Photothermal IR spectroscopy with perforated membrane micromechanical resonators

Kurek, Maksymilian

Publication date:
2017

Document Version
Publisher's PDF, also known as Version of record

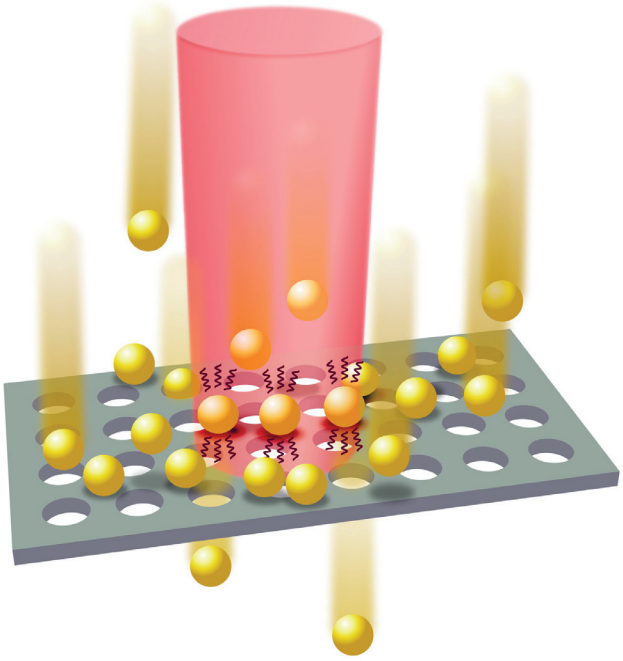

Photothermal IR spectroscopy with perforated membrane micromechanical resonators

Maksymilian Jan Kurek
PhD Thesis January 2017

DTU Nanotech
Department of Micro- and Nanotechnology

DTU Nanotech
Department of Micro- and Nanotechnology

Photothermal IR spectroscopy with perforated membrane micromechanical resonators

Maksymilian Jan Kurek

Ph.D. thesis

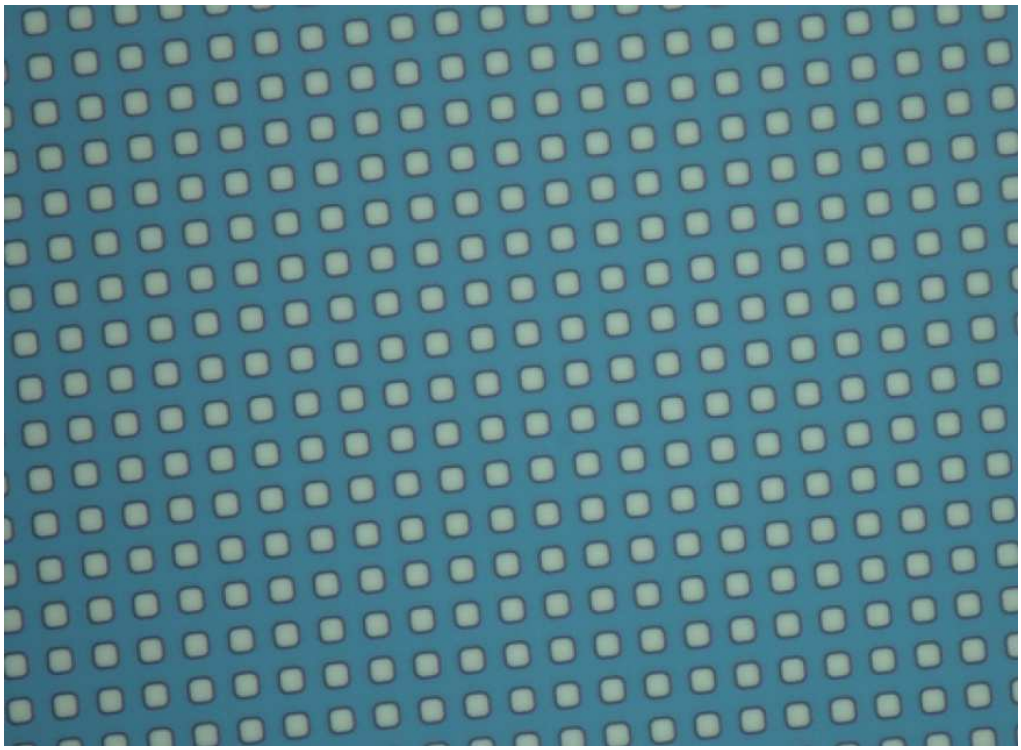

January 2017

To my lovely wife.

Preface

This thesis was written as a partial fulfillment of the requirements for obtaining the Ph.D. degree at the Technical University of Denmark (DTU). The work was carried out at the Department of Micro- and Nanotechnology (DTU Nanotech) during the period from the 1st of February 2014 to the 31st of January 2017. It has been a part of HERMES project, funded by the European Research Council.

The Ph.D. project was realized in the Nanoprobes group at DTU Nanotech with a use of DTU Danchip cleanroom facility. It was supervised by Professor Anja Boisen and Associate Professor Silvan Schmid.

Abstract

Rapid progress in nanofabrication techniques resulted in the emergence of ultrasensitive nanomechanical sensors, commonly consisting of simple vibrating structures such as cantilevers, strings or membranes that exhibit resonance behavior. The principle of operation is based on monitoring the resonance frequency shift due to various external factors, including mass, force and temperature change. The high sensitivity of nanomechanical resonators has already been exploited to create a group of photothermal spectroscopy devices capable of exceptionally fast chemical analysis of compounds on the femtogram level.

Nanomechanical infrared spectroscopy (NAM-IR) originated from photothermal bilayer cantilever deflection spectroscopy and is based on the photothermal response of a nanomechanical resonator. It has already been presented with a string resonator, which was acting as sampling element and temperature sensor. The string could be considered as a single filter-fiber and guaranteed relatively high overall sampling efficiency through impaction of airborne nanoparticles on the resonator surface. When the analyte, collected by the sensor, is exposed to IR radiation it absorbs light at a certain wavelength corresponding to its specific molecular vibrations. This thermal energy heats the resonator and leads to its thermal expansion followed by a decrease of the tensile stress in the resonator. In turn it eventually causes the resonance frequency to shift towards lower values.

However, further development of this approach was curbed by difficult and inefficient coupling of the IR light beam to a nanometer-sized resonator. In addition, readout of vibration was done by laser Doppler vibrometer, a precise but bulky and expensive instrument. These issues hindered a real-world application of the NAM-IR method. In order to overcome them, string resonators were replaced by membranes. A reliable sampling technique was maintained by adding perforation to membranes and thereby essentially getting membrane porous filters. Membranes gave also access to fully integrated magnetic transduction that allowed for significant shrinkage and simplification of the system.

An analytical model of a locally heated membrane was developed and confirmed through FEM simulations. Then, low stress silicon nitride perforated membranes were fabricated and characterized using two different experimental setups that employed optical and magnetomotive readout. Finally, spectroscopic measurements and crystallization study of about 100 pg of the model drug ‘indomethacin’ were performed. Obtained IR spectra were in good agreement both with conventional Fourier transform IR spectroscopy (FTIR) reference and literature reports. The performance of the magnetic transduction scheme was found to be comparable to the traditionally used optical detection with a minimum sample mass required for analysis of roughly 100 fg.

NAM-IR technique requires exceptionally small amount of sample and does not involve time-consuming sample preparation. Therefore, it is a promising alternative to standard IR spectroscopy with vast possible applications for example in the pharmaceutical industry.

Dansk resumé

De mange fremskridt indenfor nanofabrikationsteknikker har resulteret i udviklingen af ultra-sensitive nanomekaniske sensorer, typisk bestående af simple vibrerende strukturer såsom cantilevere, strenge eller membraner der kan virke som resonatorer. Princippet for disse sensorer er baseret på måling af skiftet i resonansfrekvensen der kan forårsages af en række forskellige faktorer såsom ændringer i masse, kraft og temperature. De nanomekaniske resonatorers høje sensitivitet udnyttes allerede indenfor fototermisk spektroskopi, hvor man ekstremt hurtigt kan foretage kemiske analyser på få femtogram prøve.

Nanomekanisk infrarød spektroskopi (NAM-IR) er udviklet på baggrund af fototermisk dobbelt lag cantilever deflection spektroskopi og er baseret på det fototermiske respons fra en nanomekanisk resonator. Konceptet er allerede vist med en streng som resonator der både opsamler prøve og virker som temperatursensor. Strengen kan ses som et filter bestående af en enkelt fiber og udviser relativt høj effektivitet ved måling af luftbårne nanopartikler på resonatorens overflade. Når partiklerne på sensoren udsættes for IR stråling absorberer de lys ved en bestemt bølgelængde der svarer til en specifik type af vibration i molekylet. Denne termiske energi opvarmer resonatoren og medfører en termisk udvidelse af materialet med efterfølgende fald i trækspændingen. Dette fald forårsager et skift i resonansfrekvensen til en lavere værdi.

Videre udvikling af denne metode blev besværliggjort af problemer med effektivt at koble IR lyset til en resonator i nanometer-størrelse. Desuden blev aflæsningen af vibrationer foretaget med et laser Doppler vibrometer. Et præcist, men dyrt instrument der er svært at håndtere. Disse problemer gjorde at NAM-IR metoden ikke var brugbar i praksis.

For at løse disse problemer blev strengen udskiftet med en membran. Den driftssikre måleteknik blev bibeholdt ved at perforere membranen og derved gøre den gennemtrængelig. Brugen af membraner i stedet for strenge gav også adgang til fuldt at integrere magnetisk transduktion der gjorde det muligt at gøre systemet væsentligt mindre og mere simpelt.

En analytisk model for en lokalt opvarmet membran blev udviklet og verificeret gennem FEM simulationer. De perforerede membraner blev fremstillet i siliciumnitrid og karakteriseret ved hjælp af to forskellige eksperimentelle set ups der gjorde brug af et optisk og meagnetomotive readout. Til sidst blev systemet brugt til at udføre spektroskopiske målinger samt foretage et studie af krystaliseringen af 100 pg indomethacin. IR spektret stemte fint overens med både den konventionelle reference 'Fourier transform IR spectroscopy' (FTIR) samt hvad der er rapporteret i litteraturen. De opnåede resultater fra det magnetiske tranduktion studie var sammenlignelige med traditionel optisk detection ved en minimum prøvestørrelse på cirka 100 fg. NAM-IR teknikken kræver kun meget små mængder prøve og involverer ikke tidskrævende prøveforberedelse. Derfor er denne teknik et lovende alternativ til standart IR spektroskopi med mange anvendelsesmuligheder indenfor f.eks. den farmaceutiske industri.

Table of contents

Chapter 1

Introduction

Since the famous visionary lecture given by Richard Feynman in 1959 [1] a tremendous technological development has gradually occurred. Such inventions as scanning tunneling microscope finally caused the emergence of nanotechnology in the 1980s which generally refers to understanding and manipulation of matter on the nanoscale. The field started continuously attracting more attention among researchers with increasing number of publications and patents [2]. It led to first applications in food [3], construction [4], textile [5], medicine [6] and automotive [7] industry. At the beginning they were limited to using nanomaterials rather than sophisticated nanostructures. However, swift progress in nanofabrication techniques resulted in emergence of micro- and nanoelectromechanical systems (NEMS/MEMS) creating vast scope of possible new applications. Numerous projects focused on these systems were accomplished in the Nanoprobes group.

1.1. Nanomechanical sensors

Among other applications, NEMS/MEMS were used as ultrasensitive sensors with sensitivity being basically function of their size. Those sensors commonly consist of simple vibrating structures like cantilevers, strings and membranes exhibiting resonance behaviour [8]. The principle of operation is based on monitoring of resonance frequency of vibration that is governed by properties of a resonator whose dimensions, mass, stiffness and stress are especially of the great importance. If any of mentioned properties is altered, the resonance frequency will shift. For instance additional mass deposited on the resonator would decrease its resonance frequency (see Figure 1.1).

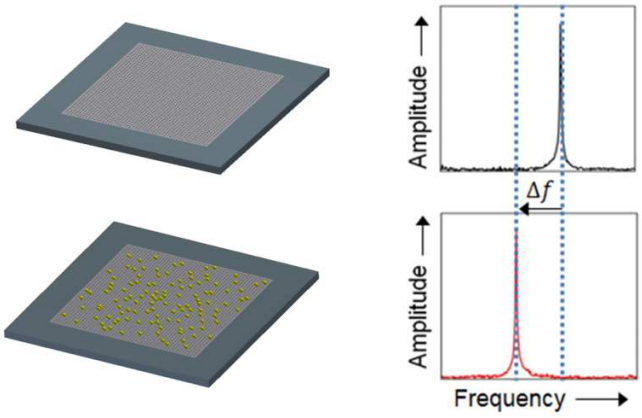

Figure 1.1 Added mass on the membrane resonator causes shift of the resonance frequency towards lower values.

This straightforward phenomenon was harnessed to build diverse sensors with extraordinary sensitivity for additional mass [9], force [10] and temperature change [11] measurements. In the last case, sensitivity in the range of μK was achieved using string resonators, which together with extremely small thermal mass of nanomechanical sensors allowed for analysis of individual nanoparticulate samples [12] and thermal characterization of nanograms of polymers [13].

1.2. Sensors for photothermal IR spectroscopy

The great performance of nanomechanical resonators as temperature sensors finally resulted in systems that were able to perform a precise identification of chemical compounds by irradiating them with IR light. Obviously the idea was inspired by conventional IR spectroscopy techniques that are well-developed and widely used but require expensive instruments, miligrams of sample and can involve time-consuming sample preparation.

In the late 1970s the photothermal IR spectroscopy was first presented [14] and was then implemented with micromechanical sensor, namely bilayer cantilever [15] (see Figure 1.2a). This approach featured high selectivity and mass sensitivity of 10 pg under ambient conditions [16]. Eventually vibrating structures were introduced to photothermal IR spectroscopy and NAM-IR technique was established. It was originally done by Shoko Yamada using silicon rich silicon nitride (SiN) string resonators (see Figure 1.2b) in Nanoprobes group at DTU Nanotech just couple of years ago and a detection limit of 44 fg was reported for measurements performed in high vacuum [17].

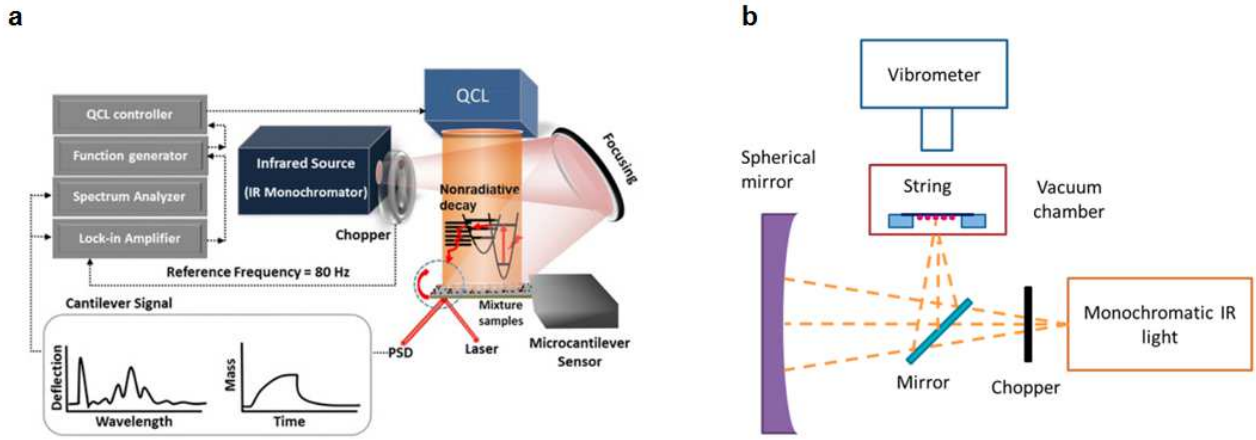

Figure 1.2 Experimental setups for a) photothermal cantilever deflection spectroscopy [16] and b) NAM-IR [17].

Using pre-stressed resonators with high quality factor (Q) values enabled increase of sensitivity and chips design fostered efficient sampling through impaction of airborne analyte nanoparticles on the surface of the sensor. Nevertheless, the remaining obstacles impeding this technique were difficult and inefficient coupling of the IR light beam with a typical diameter of several hundreds of microns to a nanometer-sized resonator and lack of integrated readout.

Replacing strings with perforated membranes helped overcoming these issues. Laser alignment on the membrane with lateral dimensions of 1×1 mm became much less troublesome. Furthermore, using membranes as porous filters improved the sampling efficiency. The mentioned initial NAM-IR setup relied on optical detection of vibration by laser Doppler vibrometer, a very accurate but bulky and expensive piece of equipment. Applying separated electrodes on the membrane surface supported introduction of magnetomotive readout and actuation scheme [18] that resulted in significant shrinkage and simplification of the sensor, facilitating its practical applications.

The quality control of the drugs during the development and production processes are of a great importance for the pharmaceutical industry [19,20]. The sample amount required for a single measurement should preferably by as small as possible, especially in the case of new and experimental drugs. Therefore the NAM-IR with extraordinarily high sensitivity and virtually no sample preparation is a promising alternative to other characterization techniques that are in use now.

The aim of this project has been to develop a new platform that would be a step towards a real-world application of the NAM-IR. The micromechanical SiN perforated membrane resonators have been chosen for this purpose due to their practical advantages over string resonators and possibility of easy implementation of magnetomotive transduction scheme. The chips were fabricated and characterized using two different experimental setups, including one designed exclusively for non-optical vibration detection. The measurements performed on the model drug indomethacin proved that this new approach to NAM-IR is capable of identifying substances without the need of laser Doppler vibrometer and sensitivity deterioration.

Chapter 2

Theory

The devices developed during this Ph.D. project are mainly different types of mechanical resonators. The general working principle of sensors based on these vibrating structures is the observation of the resonance frequency shift caused by external factors. The first part of this chapter presents an overview of the theory behind resonators including singly-clamped cantilevers, doubly-clamped beams, strings and membranes. It will help to understand which factors influence the resonating behavior of studied nanomechanical structures and how they can be exploited for sensing purposes. The aim is here to establish the theoretical framework for the thesis. The second part of the chapter is focused on the analysis of the heat transfer in a membrane that is an essential issue for NAM-IR. Most of theory explained in this chapter is not new and is primarily based on [21-26]. The model of heat transfer in the membrane was developed by Professor Ole Hansen from DTU Nanotech.

2.1. Vibrations

Vibrations are the fluctuations of a mechanical system around an equilibrium position. Most probably the early humanity interest in vibration originates from the development of musical instruments such as whistles and drums. It was the pendulum that attracted the first scientific attention in the 16th century when Galileo Galilei made his observations about the period of its vibration. Later in the 18th century beams were analyzed by Leonhard Euler and Daniel Bernoulli. Finally during the 19th centenary plates were studied by Gustav Kirchhoff and Simeon Poisson [27]. Together with the advancement in technology the awareness of the importance of the vibration phenomena arose. Vibrations occur in many common engineering systems and if uncontrolled can lead to catastrophic results. For example an earthquake can induce vibrations that may cause large stresses and building collapse. They can disturb precision measurements and provoke excessive wear of machinery parts. Therefore, often the objective is the reduction or elimination of vibrations. On the other hand they also have many beneficial uses in various applications, especially as key elements in transducers and sensors. During the last decades the group of sensors based on NEMS appeared, whose principle of operation depends on monitoring of their mechanical vibrations.

2.1.1. Driven damped one-dimensional harmonic oscillator

In order to understand the basic terms associated with vibrations (eigenfrequency, resonance, quality factor), the study of driven damped vibration of a single degree of freedom system is presented, which is modelled with harmonic oscillator attached to linear spring and linear damping element (see Figure 2.1). The spring represents the relation between the displacement and the

restoring force. In turn, the damper in the form of dashpot represents the damping force which is present in all real physical systems and is assumed to be proportional to the velocity of moving mass.

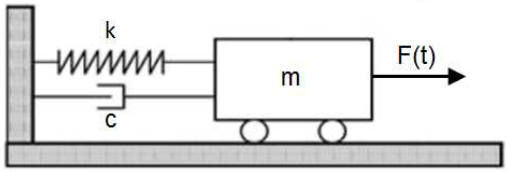

Figure 2.1 Schematic of damped one degree of freedom harmonic oscillator.

If a periodic driving force $F(t)=F_0\sin(\omega t)$ is assumed, from the equilibrium of forces acting in the system the second order differential equation of motion is:

$$m\ddot{x} + c\dot{x} + kx = F_0\sin(\omega t), \tag{2.1}$$

where m is the mass, k is the spring constant, c is the coefficient of damping force and ω is the angular frequency of driving force. Using substitutions:

$$\omega_0 = \sqrt{\frac{k}{m}}, \tag{2.2}$$

$$n_c = \frac{c}{2m}, \tag{2.3}$$

$$q = \frac{F_0}{m}, \tag{2.4}$$

the inhomogeneous second order differential equation can be written as:

$$\ddot{x} + 2n_c\dot{x} + \omega_0^2 = q\sin(\omega t), \tag{2.5}$$

where ω_0 is the angular eigenfrequency of a system without damping and n_c is the coefficient of damping. The eigenfrequency is the frequency corresponding to the natural mode of vibration and occurs when the system is undergoing the free vibration. The solution to the last equation is:

$$x = x_1 + x_2, \tag{2.6}$$

where

$$x_1 = r_0\exp^{-n_c t}\cos(ut + \varphi_0), \tag{2.7}$$

$$x_2 = B\sin(\omega t - \delta), \tag{2.8}$$

where r_0 and u are amplitude and angular frequency of damped vibration, respectively and constants B and δ are the amplitude of the forced vibration and the phase lag of the vibration against the sinusoidal force, respectively. They are chosen so the equation (2.5) is satisfied:

$$B = \frac{q}{\sqrt{\left(\omega_0^2-\omega^2\right)^2+4n_c^2\omega^2}}\,, \tag{2.9}$$

$$\tan\delta = \frac{-2n_c}{\omega_0^2-\omega}\,. \tag{2.10}$$

The general solution of the equation (2.1) is finally:

$$x(t) = \underbrace{r_0 exp^{-n_c t}\cos(ut+\varphi_0)}_{I} + \underbrace{\frac{q}{\sqrt{\left(\omega_0^2-\omega^2\right)^2+4n_c^2\omega^2}}\sin(\omega t-\delta)}_{II}. \tag{2.11}$$

The part I of the equation (2.11) reflects the fading free damped vibration of the resonator whereas part II describes the forced vibration with the frequency of the external force. The part I can be then neglected. Another important parameter of such system is the damping ratio ς defined as:

$$\zeta = \frac{n_c}{\omega_0}\,. \tag{2.12}$$

The presented above solution is valid for slight damping, when n_c<ω_0. Then the maximum amplitude of the system can be derived by calculating its derivative with respect to driving frequency and setting it equal to zero. As a result the resonance angular frequency ω_r which is the frequency of the highest amplitude can be obtained:

$$\omega_r = \omega_0\sqrt{1-2\zeta^2}\,, \tag{2.13}$$

It can be clearly seen that for slight damping the resonance angular frequency nearly overlaps with the eigenfrequency of the system. If the damping ratio is higher than approximately 0.707 the resonance frequency peak disappears. Using the equation (2.10) the phase lag at resonance is roughly $\pi/2$ (see Figure 2.2).

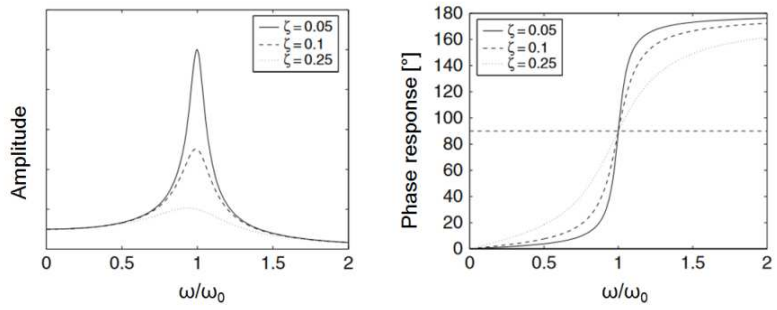

Figure 2.2 Amplitude (left) and phase (right) response as a function of the driving frequency for different damping ratios.

The next crucial value describing the vibrating system is the quality factor *Q*. It indicates the sharpness of the resonance peak and is defined as a ratio between stored *W* and lost *ΔW* energy during one cycle of vibration at resonance:

$$Q = 2\pi \frac{W}{\Delta W} . \quad (2.14)$$

The maximal kinetic energy of the system can be used to find its total energy. With a displacement at resonance of $x = a\sin(\omega t)$ the maximal kinetic energy is:

$$W = \frac{1}{2} m\dot{x}^2 = \frac{1}{2} m a^2 \omega_r^2 . \quad (2.15)$$

The energy is lost because of work of the dissipative force $F_d = -c\dot{x}$ also during one cycle of vibration:

$$\Delta W = -\int_0^{2\pi/\omega_r} F_d \dot{x} dt = -\int_0^{2\pi/\omega_r} c\dot{x}^2 dt = \pi c a^2 \omega_r . \quad (2.16)$$

The quality factor can be rewritten using equation (2.14) or with (2.3), (2.12) and (2.13) as:

$$Q = \frac{m\omega_r}{c} , \quad (2.17)$$

$$Q = \frac{\sqrt{1-2\zeta^2}}{2\zeta} . \quad (2.18)$$

Obviously, the low damping in the system is required in order to have a high quality factor. The sharper the resonance peak, the better it can be determined facilitating higher possible frequency resolution of sensors based on nanomechanical vibrating structures.

2.1.2. Euler-Bernoulli beam theory

The Euler-Bernoulli beam theory will be harnessed for analysis of one-dimensional free and conservative bending vibrations of structures that were actually used throughout this Ph.D. project. A beam is defined as an object having one of its dimensions much larger than the other two. The beam is considered thin if ratio of its length to height is at least 10, then the rotational inertia and the shear deformation can be neglected. A fundamental assumption is that the cross-section of the beam is infinitely rigid in its own plane so no deformations occur in this plane. Moreover, for the out-of-plane displacement, during the deformation of the beam the cross-section remains plane and normal to the deformed axis of the beam. On the basis of the equilibrium of forces for an infinitesimal piece of beam the equation of motion can be derived. If a linear elastic material of the beam, small deflections *U(x,t)* and no damping in the system are assumed then the equation of motion of a thin beam with length *L*, width *w* and height *h* (see Figure 2.3) is:

$$\rho A \frac{\partial^2 U(x,t)}{\partial t^2} + E I_y \frac{\partial^4 U(x,t)}{\partial x^4} = 0, \quad (2.19)$$

where ρ is the mass density, *A* is the cross sectional area, *E* is the Young's modulus and I_y is the geometric moment of inertia about the y-axis. The solution to this differential equation is a superposition of normal modes. The out-of-plane displacement function can be separated into a position dependent and a time dependent term in order to solve it:

$$U(x,t) = \sum_{n=1}^{\infty} U_n(x)\cos(\omega t), \quad (2.20)$$

where ω is the angular frequency, n is the mode number and $U_n(x)$ is the displacement function with a general solution consisting of trigonometric functions that represent standing waves in the beam center and hyperbolic functions that describe the behavior at the clamped ends of the beam:

$$U_n(x) = a_n cos\beta_n x + b_n sin\beta_n x + c_n cosh\beta_n x + d_n sinh\beta_n x, \quad (2.21)$$

where β_n is the wavenumber. By insertion of equation (2.21) into (2.19) the equation of motion can be rewritten as:

$$-\rho A\omega^2 U(x,t) + EI_y\beta_n^4 U(x,t) = 0. \quad (2.22)$$

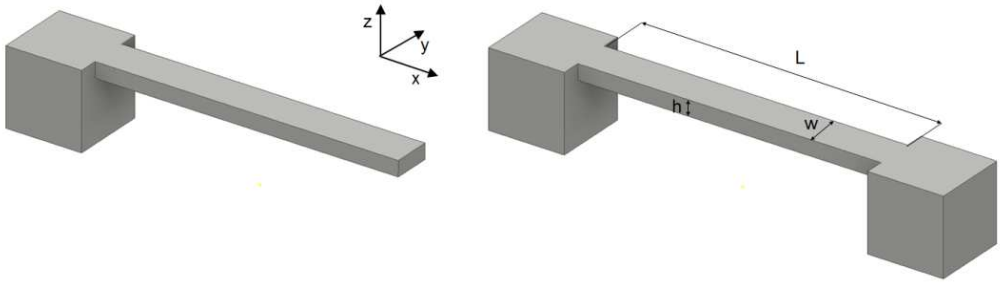

Figure 2.3 Singly-clamped cantilever (left) and doubly-clamped beam (right).

Finally the angular eigenfrequency as a function of the wavenumber is:

$$\omega = \beta_n^2\sqrt{\frac{EI_y}{\rho A}}\,. \quad (2.23)$$

The unknown coefficients a_n, b_n, c_n and d_n must be found to derive the wavenumber of specific eigenmodes of the beam. It can be achieved by determining the boundary conditions of a given case of the beam.

2.1.2.1. Singly-clamped cantilever

The singly-clamped cantilever is fixed at one end and the curvature and momentum are zero at the free end:

$$U_n(0) = \frac{\partial U_n(0)}{\partial x} = \frac{\partial^2 U_n(L)}{\partial x^2} = \frac{\partial^3 U_n(L)}{\partial x^3} = 0. \quad (2.24)$$

Applying these boundary conditions to equation (2.21) and calculating the system of four linear equations, the frequency equation can be obtained:

$$cos(\beta_n L)cosh(\beta_n L) + 1 = 0. \quad (2.25)$$

It can be solved numerically and the three first roots $\beta_n L = \lambda_n$ are 1.8751, 4.6941 and 7.8548. The angular eigenfrequency of a singly-clamped cantilever is:

$$\omega = \frac{\lambda_n^2}{L^2}\sqrt{\frac{EI_y}{\rho A}}. \tag{2.26}$$

2.1.2.2. Doubly-clamped beam

On the other hand doubly-clamped beam is fixed at both ends, hence the boundary conditions are:

$$U_n(0) = U_n(L) = \frac{\partial U_n(0)}{\partial x} = \frac{\partial U_n(L)}{\partial x} = 0. \tag{2.27}$$

As in the previous case, the boundary conditions help to define the system of linear equations that leads to the following frequency equation:

$$cos(\beta_n L)cosh(\beta_n L) - 1 = 0, \tag{2.28}$$

with the three first roots equal to $\beta_n L = \lambda_n$=4.7300, 7.8532 and 10.9956. It means that for the same dimensions and material properties doubly-clamped beam has higher eigenfrequency values than singly-clamped cantilever. In addition, boundary conditions can be used for obtaining the mode shapes of studied structures. Figure 2.4 depicts three first mode shapes of cantilevers and beams.

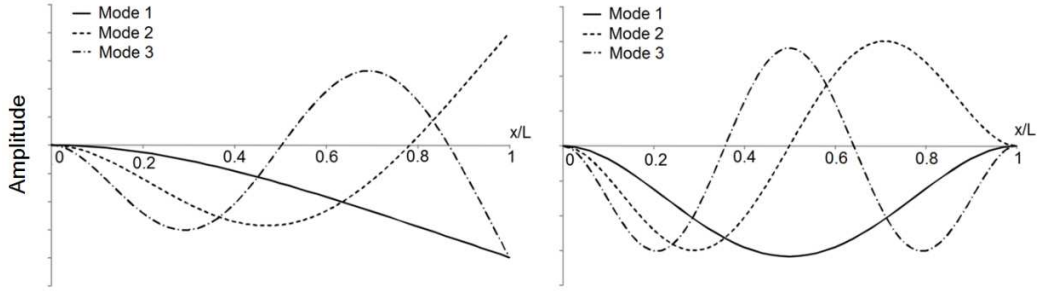

Figure 2.4 Modal shapes of singly-clamped cantilever (left) and doubly-clamped beam (right).

2.1.2.3. Doubly-clamped pre-stressed beam (string)

The equation of motion (2.19) is valid only if there is no tensile stress in the beam. However microfabrication of resonators often introduces process related tensile stress σ. Therefore the equation of motion has to be modified by adding the tensile force $N=\sigma A$:

$$\rho A\frac{\partial^2 U(x,t)}{\partial t^2} + EI_y\frac{\partial^4 U(x,t)}{\partial x^4} - N\frac{\partial^2 U(x,t)}{\partial x^2} = 0. \tag{2.29}$$

This equation is more complex than (2.19) but can be solved using the same approach as presented before yet with changed boundary conditions. The pinned supports are assumed instead of fixed ones. They cannot resist a momentum so the rotation of beam ends is allowed which would give an error in the shape functions especially at the clamping regions:

$$U_n(0) = U_n(L) = \frac{\partial^2 U_n(0)}{\partial x^2} = \frac{\partial^2 U_n(L)}{\partial x^2} = 0. \tag{2.30}$$

The displacement function of sinusoidal mode shape with the wavenumber β_n is assumed independent of the tensile tress:

$$U_n(x) = U_{0,n}\sin(\beta_n x). \tag{2.31}$$

Analogous calculation as for previous cases yields the term for angular eigenfrequency ω_n:

$$\omega_n = \frac{n^2\pi}{2L^2}\sqrt{\frac{EI_y}{\rho A}}\sqrt{1+\frac{\sigma AL^2}{n^2\pi^2 EI_y}}\,, \tag{2.32}$$

with the wavenumber that satisfies the new boundary conditions (2.30):

$$\beta_n = \frac{n\pi}{L}\,. \tag{2.33}$$

Comparison of equation (2.32) to (2.26) shows that the tensile stress increases the angular eigenfrequency of the beam. When $12\sigma L^2 \gg n^2\pi^2 Eh^2$ the flexural rigidity of the beam can be neglected and equation (2.32) reduces to:

$$\omega_n = \frac{n\pi}{L}\sqrt{\frac{\sigma}{\rho}}\,. \tag{2.34}$$

2.1.2.4. Rectangular and square membrane

The membrane is essentially a plate under tensile stress. The equation of motion of a rectangular membrane is given by the two-dimensional wave equation:

$$\sigma\nabla^2 U(x,y,t) - \rho\frac{\partial^2 U(x,y,t)}{\partial t^2} = 0. \tag{2.35}$$

In this case separation of time and spatial variables is necessary as well:

$$U(x,y,t) = U(x,y)\cos(\omega t), \tag{2.36}$$

with a sinusoidal mode shape:

$$U(x,y) = \sum_{n=0}^{\infty}\sum_{m=0}^{\infty} c_{n,m} sin\left(\frac{n\pi x}{L_x}\right) sin\left(\frac{m\pi y}{L_y}\right), \tag{2.37}$$

where n and m are mode numbers and L_x and L_y are the side lengths of the membrane in x and y direction. By using this equation in equation (2.35) the angular eigenfrequency of a simply supported membrane becomes:

$$\omega_{n,m} = \sqrt{\frac{\sigma}{\rho}}\sqrt{\frac{n^2\pi^2}{L_x^2}+\frac{m^2\pi^2}{L_y^2}}\,. \tag{2.38}$$

It can be further reduced if the membrane is a square with a side length L:

$$\omega_{n,m} = \frac{\pi}{L}\sqrt{n^2 + m^2}\sqrt{\frac{\sigma}{\rho}}\,. \tag{2.39}$$

The angular eigenfrequency of a circular membrane with radius *r* can be approximated with the Rayleigh method that is based on the complete commute of the energy between its kinetic and potential state assuming a conservative system. For fundamental mode calculation yields:

$$\omega_{1,1} \approx \frac{2.415}{r}\sqrt{\frac{\sigma}{\rho}}\,. \tag{2.40}$$

It should be noted that the general relation between frequency *f* and angular frequency *ω* is:

$$\omega = 2f\pi. \tag{2.41}$$

2.1.3. Quality factor of pre-stressed resonators

It was first experimentally observed that highly stressed resonators have much higher quality factor values than structures of the same dimensions but without significant tensile stress [28,29]. Non-stressed resonators store $W_{bending}$ and lose $\Delta W_{bending}$ energy due to bending. Apart from that, pre-stressed structures such as strings and resonators can also store $W_{elongation}$ and dissipate $\Delta W_{elongation}$ energy in lateral elongation. However, the most important contribution to the stored energy comes from the presence of the tensile stress. More exactly from the elastic energy $W_{tensile}$ which is a result of work of vibrational deflection against the lateral tensile stress. Therefore the quality factor of the pre-stressed resonator is:

$$Q = 2\pi\frac{W_{tensile}+W_{elongation}+W_{bending}}{\Delta W_{elongation}+\Delta W_{bending}}\,. \tag{2.42}$$

The elongation and bending factors can be considered the intrinsic damping $Q_{intrinsic}$ that summarizes all energy loss mechanisms that take place on the surface or in the bulk material of the resonator. Assuming that the magnitude of the tensile pre-stress is dominating the mechanical behavior and $Q_{intrinsic}$ is equal for elongation and bending, the equation (2.42) can be simplified to:

$$Q \approx \alpha_{dd} Q_{intrinsic}\,, \tag{2.43}$$

where α_{dd} is the damping dilution factor:

$$\alpha_{dd} = \left(\frac{W_{bending}}{W_{tension}} + \frac{W_{elongation}}{W_{tension}}\right)^{-1}. \tag{2.44}$$

As the $W_{tension}$ is a dominating stored energy source for pre-stressed resonators, the damping dilution factor is larger than unity. It means that quality factor is enhanced in comparison to relaxed resonator without an effect of high tensile stress.

As it has been already mentioned in 2.1.2.3., the mode shape of the string resonator should include bending near the clamping regions. The rest of the resonator follows just the sinusoidal shape.

Further reduction of the damping dilution factor to the bending energy only gives for a rectangular string with a width *w*, length *L*, height *h* and mode number *n*:

$$\alpha_{dd,string} \approx \left(\frac{(n\pi)^2}{12} \left(\frac{h}{L}\right)^2 \frac{E}{\sigma} + \frac{1}{\sqrt{3}} \frac{h}{L} \sqrt{\frac{E}{\sigma}} \right)^{-1}. \tag{2.45}$$

The right term represents the effect of edge bending and the left term represents the anti-nodal sine bending of the string. Typically $h \ll L$ so quality factor is mainly limited by the energy loss near the edges of a vibrating structure. The quality factor is expected to be higher for longer strings.

If a similar mode shape approach and assumptions are applied for a rectangular membrane with edge length *L*, the calculation of energies stored during one cycle of vibration gives:

$$\alpha_{dd,membrane} \approx \left(\frac{\pi^2 (n^2+m^2)}{12} \left(\frac{h}{L}\right)^2 \frac{E}{\sigma} + \frac{1}{\sqrt{3}} \frac{h}{L} \sqrt{\frac{E}{\sigma}} \right)^{-1} \tag{2.46}$$

2.2. Heat transfer

The local heat flux into the membrane will cause thermal expansion of the resonator material. In turn, it will lead to change of the tensile stress across the membrane and eventually to a resonance frequency shift. Analytical model of the membrane with a heat source located in the center would give a valuable insight into the process of the heat transfer in the membrane and its implications. A two-dimensional isotropic continuous circular membrane was considered for the sake of simplicity. The analysis was ultimately performed in the polar coordinate system due to the symmetry of the studied object (see Figure 2.5).

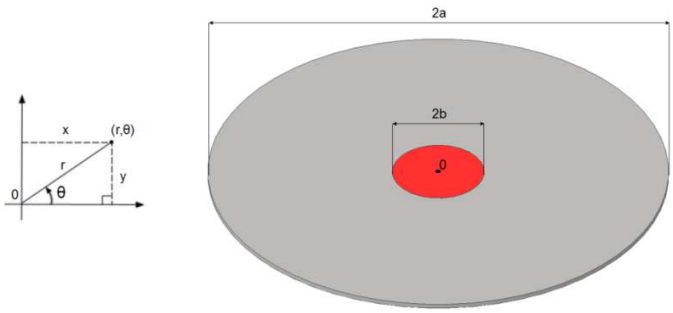

Figure 2.5 Schematic drawing of a membrane with radius size *a* and height *h*. Circular heat source with a radius size *b* is placed in the center of the membrane.

The thermal stress induced resonance frequency shift problem involves solving in fact three problems on a membrane: a static temperature distribution, an in-plane thermal stress and a deflection eigenmode problem.

The thermal problem can be approached first with the steady state heat conduction that is governed by the Fourier's law assuming unidirectional heat flow and the isothermal membrane edges [30]:

$$\boldsymbol{J}_q = -\kappa \nabla T, \tag{2.47}$$

where $\boldsymbol{J}_q$ is the heat flux, κ is the thermal conductivity and ∇T is the gradient of temperature. The negative sign indicates that the heat flow is in the direction of decreasing temperature. The conservation equation for heat can be written as:

$$C_V \frac{\partial T}{\partial t} = \kappa \nabla^2 T + q, \tag{2.48}$$

where C_v is the heat capacity per unit volume and $q=q(r)$ is the heat dissipated per unit volume. In steady state the heat diffusion equation is:

$$\kappa \nabla^2 T + q = 0. \tag{2.49}$$

The membrane is heated by power P input so:

$$q(r) = \frac{P}{\pi b^2 h} \times H(b - r), \tag{2.50}$$

where H(r) is Heaviside step function. Since this problem has ideal rotational symmetry it can be simplified such that $T=T(r)$ and $T(a)=0$. In the polar coordinate system equation (2.49) is:

$$\kappa \frac{1}{r} \frac{\partial}{\partial r}\left(r \frac{\partial T}{\partial r}\right) = -\frac{P}{\pi b^2 h} \times H(b - r). \tag{2.51}$$

The solution for $r>b$ is:

$$T(r) = -\frac{P}{2\pi\kappa h} \ln \frac{r}{a}, \tag{2.52}$$

and for $r<b$ is:

$$T(r) = \frac{P}{4\pi\kappa h} \frac{\left(b^2 - r^2\right)}{b^2} - \frac{P}{2\pi\kappa h} \ln \frac{b}{a}. \tag{2.53}$$

The in-plane thermal stress problem can be derived from the force balance condition on a volume element which requires the stress-strain-temperature relations:

$$\epsilon_x = \frac{1}{E}\left(\sigma_x - \nu \sigma_y\right) + \alpha T, \tag{2.54}$$

$$\epsilon_y = \frac{1}{E}\left(\sigma_y - \nu \sigma_x\right) + \alpha T, \tag{2.55}$$

where α is the thermal expansion coefficient and assuming that the stresses in the thickness direction of the membrane can be ignored: $\sigma_z=0$ and $\tau_{xz}=\tau_{yz}=\tau_{zx}=\tau_{zy}=0$. Then also shear strains vanish: $\gamma_{xz}=\gamma_{yz}=\gamma_{zx}=\gamma_{zy}=0$. Applying the elastic relation between shear stress and strain:

$$\gamma_{ij} = \frac{2(1+\nu)}{E}\tau_{ij}, \tag{2.56}$$

and using equations (2.54) and (2.55), the stress formulas can be obtained:

$$\sigma_x = \frac{E}{1-\nu^2}\left(\frac{\partial u_x}{\partial x} + \nu\frac{\partial u_y}{\partial y} - (1+\nu)\alpha T\right), \tag{2.57}$$

$$\tau_{xy} = \tau_{yx} = \frac{E}{2(1+\nu)}\left(\frac{\partial u_x}{\partial y} + \frac{\partial u_y}{\partial x}\right), \tag{2.58}$$

where u_x and u_y are the components of the in-plane displacement vector $\boldsymbol{u}=(u_x,u_y)$. Lateral force balance further requires:

$$h\left(\frac{\partial \sigma_x}{\partial x} + \frac{\partial \tau_{xy}}{\partial y}\right) = 0, \tag{2.59}$$

$$h\left(\frac{\partial \sigma_y}{\partial y} + \frac{\partial \tau_{xy}}{\partial x}\right) = 0. \tag{2.60}$$

After inserting stress expressions (2.57) and (2.58) to equations (2.59) and (2.60):

$$\frac{\partial^2 u_x}{\partial x^2} + \frac{1-\nu}{2}\frac{\partial^2 u_x}{\partial y^2} + \frac{1+\nu}{2}\frac{\partial^2 u_y}{\partial x \partial y} = (1+\nu)\alpha\frac{\partial T}{\partial x}, \tag{2.61}$$

$$\frac{\partial^2 u_y}{\partial y^2} + \frac{1-\nu}{2}\frac{\partial^2 u_y}{\partial x^2} + \frac{1+\nu}{2}\frac{\partial^2 u_x}{\partial x \partial y} = (1+\nu)\alpha\frac{\partial T}{\partial y}. \tag{2.62}$$

This in-plane displacement problem can be also simplified in the polar coordinate system due to the rotational symmetry. Since it is expected that $u_\theta=0$ and only u_r is non-zero, equations (2.61) and (2.62) can be reduced to:

$$\frac{\partial}{\partial r}\left(\frac{1}{r}\frac{\partial r u_r}{\partial r}\right) = (1+\nu)\alpha\frac{\partial T}{\partial r}. \tag{2.63}$$

Assuming boundary conditions $u_r(a)=0$ and $u_r(0)=0$ can be obtained:

$$u_r = (1+\nu)\frac{\alpha}{r}\int_0^r rT(r)dr + C_1 r + \frac{C_2}{r}, \tag{2.64}$$

where constants C_1 and C_2 are:

$$C_1 = -(1+\nu)\frac{\alpha}{a^2}\int_0^a rT(r)dr, \tag{2.65}$$

$$C_2 = 0. \tag{2.66}$$

The equation (2.57) can be rewritten now in the polar coordinates to:

$$\sigma_r = -\alpha E\left(\frac{1}{r^2}\int_0^r rT(r)dr + \frac{1+\nu}{1-\nu}\frac{1}{a^2}\int_0^a rT(r)dr\right). \tag{2.67}$$

In order to simplify the above equation, *b=0* can be assumed which means that the excitation is a delta function power applied at *r=0*. Then the temperature can be expressed just as (2.52) and the radial stress becomes:

$$\sigma_r = -\frac{\alpha EP}{4\pi\kappa h}\left(\frac{1}{1-\nu} - \ln\frac{r}{a}\right). \tag{2.68}$$

The equation of motion of the membrane with a tensile stress σ_0, in polar coordinates is:

$$\frac{1}{r}\frac{\partial}{\partial r}\left(\sigma_0 r\frac{\partial U(r,t)}{\partial r}\right) - \rho\frac{\partial^2 U(r,t)}{\partial t^2} = 0. \tag{2.69}$$

For a circular clamped membrane boundary condition is *U(a,t)=0*, then according to equation (2.40) the fundamental mode angular frequency is:

$$\omega_0 = \frac{2.404}{a}\sqrt{\frac{\sigma_0}{\rho}}\,. \tag{2.70}$$

When the additional heat-induced tensile stress σ_r must be taken into account:

$$\frac{1}{r}\frac{\partial}{\partial r}\left((\sigma_0 + \sigma_r) r\frac{\partial U(r,t)}{\partial r}\right) - \rho\frac{\partial^2 U(r,t)}{\partial t^2} = 0\,. \tag{2.71}$$

To find the fundamental mode angular frequency ω of the heated membrane and then angular frequency shift, equation (2.71) must be solved. As the stress in this case is dependent on the radial position on the membrane, the approximated result can be obtained using the Rayleigh's coefficient method. The final result for the relative fundamental eigenmode shift is:

$$\frac{\omega-\omega_0}{\omega_0} = -\frac{\alpha EP}{8\pi\kappa h\sigma_0}\left(\frac{2-\nu}{1-\nu} - 0.642\right), \tag{2.72}$$

which is proportional to the absorbed power *P* and does not depend on the membrane lateral dimensions.

2.3. Summary

In this chapter the simple model of damped vibrations of a forced oscillator was analyzed and very important terms of resonance frequency and quality factor were defined. Next, the undamped free vibration of singly-clamped cantilever, doubly-clamped beam and membrane were described on the basis of the Euler-Bernoulli theory. The influence of the high tensile stress on the behavior of these resonators was studied as well. Finally, the case of a membrane heated in the center was investigated in detail in order to understand the character of the resonance frequency shift caused by temperature profile change across the membrane.

Chapter 3

Pyrolytic carbon resonators

Part of my Ph.D. activities were dedicated to the investigation of pyrolytic carbon as a material for the fabrication of micromechanical resonators. In this chapter, the fabrication and thorough characterization of pyrolytic carbon singly-clamped cantilever and doubly-clamped string resonators are discussed. First, the fabrication process is explained and its outcome studied. Then the mechanical properties of resulting structures are explored in order to understand the influence of processing conditions and further perspectives of using pyrolytic carbon structures for sensing purposes.

3.1. Introduction

Micro- and nanomechanical resonators are typically fabricated from low-loss semiconductor materials and ceramics, such as silicon [31], low and high stress silicon nitride [32], silicon carbide [33] or aluminium nitride [34]. However, for the realization of micro- and nanoelectromechanical systems, the micromechanical resonators should preferentially be electrically conductive, which requires additional doping in the case of semiconductors and metallization in the case of ceramics. The conductivity is important mostly in terms of implementation of various actuation and readout schemes [35]. On the other hand, pyrolytic carbon is already conductive [36] and can be obtained directly from photoresist through pyrolysis at elevated temperatures in inert atmosphere. The advantage of this fabrication method is that the geometry of carbon micro- and nanostructures such as micropillar arrays [37], bridges [36] and suspended nanowires [38] can be defined through simple photolithographic processes followed by pyrolysis, which generally is a heating of an organic material in the absence of oxygen that leads to its irreversible thermochemical decomposition into combustible gases and carbon [39]. Up to now a few different approaches to fabricate carbon-based singly-clamped cantilevers [40] and doubly-clamped beams [41] were presented using soft lithography or multiple steps of photolithography (see Figure 3.1), but pyrolytic carbon strings resonators have not been yet reported.

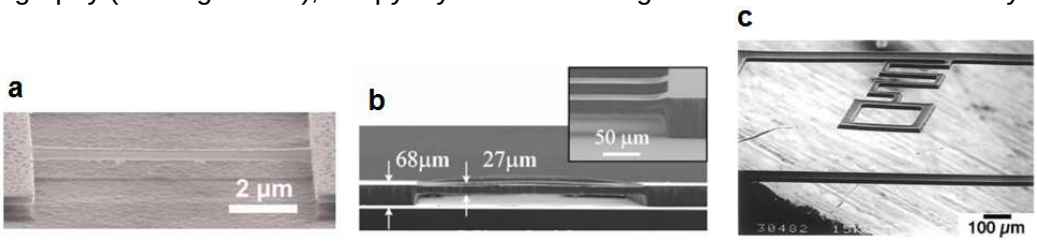

Figure 3.1: Images of pyrolytic carbon a) doubly-clamped beam [41], b) microbridge [36] and singly-clamped structure representing the sensing unit of an accelerometer [40].

Therefore the goal of this research was to develop a simple and reliable process for fabrication of both cantilevers and strings resonators. The fabrication approach for strings was planned to take an advantage of a considerable tensile stress that would be generated in doubly-clamped structures due to shrinkage and mass loss of the photoresist during pyrolysis [42]. According to the statements from the previous chapter it would significantly enhance quality factor of the final structures.

3.2. Methods

For the purpose of obtaining pyrolytic carbon string resonators, new fabrication approaches were developed and employed. The cleanroom work was mostly performed by Frederik Kjær Larsen as a part of his bachelor project supervised by Associate Professor Stephan Sylvest Keller and Associate Professor Silvan Schmid at DTU Nanotech.

3.2.1. Fabrication

Two various photoresist precursors were used, namely negative SU-8 2005 (SU-8) and positive photoresist AZ 5214e (AZ). It was expected that these two photoresist types would experience different behavior during pyrolysis, especially regarding the shrinkage level. The photolitography masks were designed using L-Edit 15 (Tanner Research, Monrovia, CA, USA) software that is a CAD drawing tool. They included singly-clamped cantilevers and doubly-clamped beams with diverse lengths *L* of 100, 200, 300, 400, 500, 625, 750, 875, 1000 and 1500 µm and widths *w* of 3, 6, 14, 30 and 50 µm combinations. The fabrication process consisted of the three main steps: photolithography, dry etching and pyrolysis. Two different fabrication strategies called “dry etch-pyrolysis” and “pyrolysis-dry etch” were investigated, where the last two process steps were carried out in inverse order (see Figure 3.2). After the photolithography either dry etching or pyrolysis was performed first followed by pyrolysis or dry etching, respectively. This approach would give relevant information about the influence of particular fabrication step on the resulting structures. The process conditions of photolithography, dry etching and pyrolysis were identical regardless of the fabrication strategy.

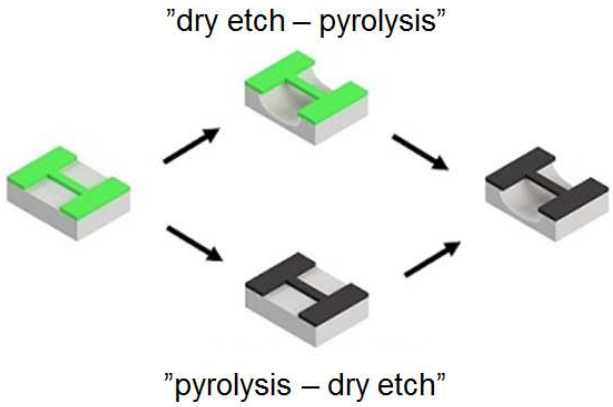

Figure 3.2: Schematic of two fabrication strategies for pyrolyzed photoresist microresonators. The grey color is the silicon substrate, green is the photoresist and black is the carbon (see Appendix A).

Each process started with the spin-coating of a single layer of photoresist on the surface of single side polished 525 µm thick 4 inch silicon wafers. The wafers for AZ resist (AZ Electronic Materials, Somerville, NJ, USA) were dipped in 5% buffered hydrofluoric acid (BHF) solution for 60 s to remove the native oxide. Spin-coating for 30 s with an acceleration of 1000 rpm/s and a spin speed of 725 rpm was performed on the automatic spin-coater (Maximus 14 from ATMsse GmbH, Singen, Germany) to obtain a resist thickness of 4.2 µm. The photoresist was soft-baked at 90°C for 60 s and patterned in mask aligner (MA6 from Süss MicroTec AG, Garching, Germany) by hard contact ultraviolet (UV) exposure with a dose of 100 mJ/cm^2. This was followed by development in AZ 351B diluted 1:5 in water for 70 s, rinse with water for 3 min and drying in the spin rinse dryer for 90 s. For the SU-8 resist (MicroChem, Westborough, MA, USA) a dehydration bake at 250 °C for 30 min was performed for the wafers prior to film deposition. Spin coating on the manual spin-coater (RCD8 from Süss MicroTec AG, Garching, Germany) for 30 s with an acceleration of 5000 rpm/s and a spin speed of 2000 rpm resulted in a 5.5 µm thick SU-8 film. After spin-coating the wafers were placed in a ventilated area for 2 h to partially evaporate the solvent [43] which was followed by hard contact UV exposure with a dose of 200 mJ/cm^2. The post exposure bake of the SU-8 was done on a hotplate with a temperature ramp of 2°C/min up to 50°C. Subsequently 60 min later the hotplate was switched off and together with wafers allowed to cool down to room temperature. The SU-8 was then developed in propylene glycol methyl ether acetate (PGMEA) for 2×2 min, rinsed with 2-propanol (IPA) and dried in air for 60 min.

Releasing the microresonators by under-etching required highly isotropic etching of silicon while avoiding damage of the structures of interest. Hence, dry etching using a deep reactive ion etcher (standard rate ASE, Surface Technology Systems, Newport, UK) was chosen. The plasma etching generates heat and radiation, which may potentially cause high intrinsic stress and large deformations in the suspended structures and eventually affect the further usability of the devices. Therefore, a dry etch recipe earlier optimized for the release of thin SU-8 cantilevers was applied [44]. The process was conducted with a coil power of 1500 W, SF_6 gas flow rate of 300 sccm to increase the chemical etching of silicon and without use of O_2 gas to minimize the etching of photoresist. The chuck temperature was kept at 0°C to minimize thermal stress in the microresonators. In addition the platen was switched off to enhance the isotropic etch. The etch time should be kept as short as possible to minimize etching of the photoresist and prevent heating. It turned out that 5 min was enough to ensure that the majority of the structures were successfully released. Only the widest resonators, with a width of 50 µm, were still connected to the Si substrate after the process.

For pyrolysis, the wafers were loaded into a PEO-601 furnace (ATV Technologie GmbH, Vaterstetten, Germany) with a N_2 gas flow rate of 24 L/min and first heated from room temperature to 200°C. Maintaining this temperature for 30 min supports elimination of solvents from the photoresist and residual O_2 from the furnace. Then the temperature was increased to 900 °C and kept constant for 60 min to complete the carbonization. Finally the oven was cooled down to room temperature. The ramp rate for all temperature changes was 2°C/min.

3.2.2. Characterization

The initial evaluation of the structures was done on the basis of their scanning electron microscope (SEM) images. Afterwards the fundamental mode resonance frequency measurements were performed.

3.2.2.1. Outcome of the fabrication processes

The fabrication approach in which structures were defined first by the means of photolithography, then released through dry etching and finally pyrolyzed, was successful only for certain photoresist and resonator types. The chips were inspected using SEM (Supra 40 VP from Zeiss, Jena, Germany) after second and last step of the process. Its outcome is summarized in the Figure 3.3.

All singly- and doubly-clamped resonators except the widest ones with a width of 50 µm were released. Although the dry etch recipe was optimized to reduce intrinsic and extrinsic stress in released polymer microstructures [44], doubly-clamped photoresist strings experienced structural changes during dry etching, which resulted in a contorted and undefined shape, in particular at increased distance from the clamping (see Figure 3.3e) for resonators with a nominal width up to 6 µm. The wider structures were simply buckled instead (see Figure 3.3a).

Figure 3.3b,c,f,g,h,i show doubly-clamped carbon based SU-8 (SU8-C) and AZ (AZ-C) strings. After pyrolysis, the deformed resist strings were transformed into straight and well-defined suspended pyrolytic carbon structures. This straightening was caused by a considerable shrinkage of the photoresist during pyrolysis. The isotropic silicon dry etching resulted in an under-etch of roughly 23 µm at the clamping of the strings. After pyrolysis, the width of the overhanging area decreased to around 11 µm, resulting in an elongation of the doubly-clamped resonators of approximately 25 µm independent of the initial length of the strings.

Furthermore, the width of the resonators was also considerably reduced due to shrinkage. For example, suspended AZ resonators with a nominal width of w = 14 µm before pyrolysis had a final width of only around 6 µm. The narrowest doubly-clamped AZ-C strings with a nominal width of w = 3 µm and L > 500 µm ruptured. For doubly-clamped pyrolytic carbon resonators obtained from SU-8 resist, buckling was generally observed as presented in Figure 3.3c.

For both photoresist types, fabrication of singly-clamped cantilevers was not successful with this processing scheme due to large initial bending of the microstructures after pyrolysis (see Figure 3.3d).

Finally, the comparison of the fabricated structures indicates a difference in behavior between SU-8 and AZ photoresist during pyrolysis (see Figure 3.3b,h). The doubly-clamped resonators obtained with AZ as a precursor had a relatively well-defined clamping area with a sharp corner. In contrast, the structures based on SU8-C showed a smooth transition between string and clamping edge. This dissimilarity can be associated with different levels of lateral shrinkage and resist reflow of positive and negative photoresists during pyrolysis [36].

In conclusion, the “dry etch-pyrolysis” process based on the AZ resist precursor yielded doubly-clamped pyrolytic carbon string resonators with tensile stress while no structures suitable for further experiments were obtained on the basis of SU-8 resist precursor because they remained buckled even after the pyrolysis and due to low level of induced tensile stress.

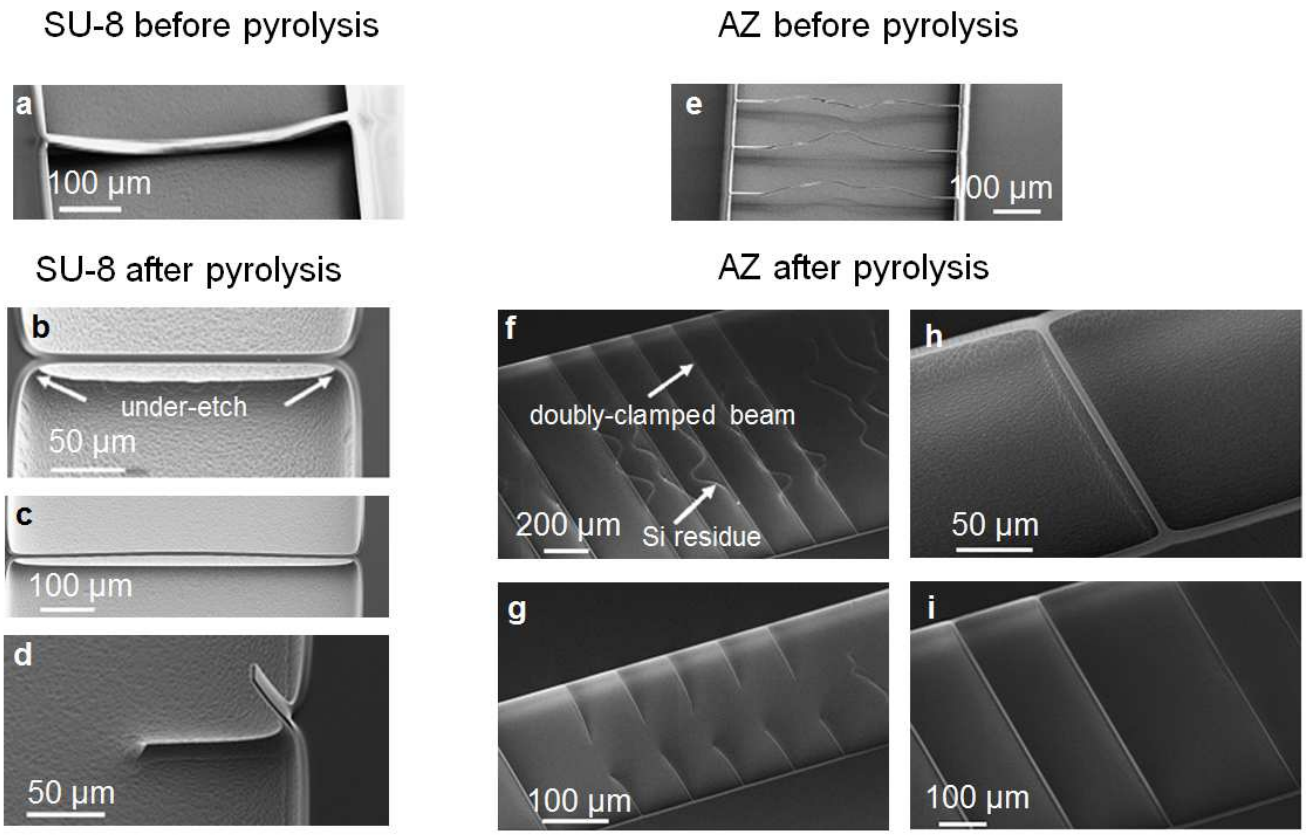

Figure 3.3: SEM pictures of the fabrication output of the “dry etch-pyrolysis” strategy. a) SU-8 photoresist resonators (*L*=500 µm, *w*=14 µm) collapsed after dry etch; b) Suspended SU8-C (*L*=200 µm, *w*=30 µm); and c) (*L*=500 µm, *w*=14 µm) resonators; d) SU8-C cantilever (*L*=100 µm, *w*=30 µm) with high initial bending; e) AZ photoresist resonators (*L*=200 µm, *w*=6 µm) with severely distorted structure due to high local temperature during dry etch; f) The remained curled paths in the silicon correspond to the shape of the AZ resonators during the dry etching process. After pyrolysis step the AZ-C (*L*=1500 µm, *w*=6 µm) resonators were straight again; g) The shrinkage of the photoresist due to the pyrolysis induced tensile stress that could not be withstood by all doubly-clamped structures (*L*=500 µm, *w*=6 µm); h) Short AZ-C (*L*=200 µm, *w*=14 µm); and i) long (*L*=500 µm, *w*=14 µm (left) and *w*=6 µm (right)) resonators. All dimensions are nominal mask dimensions.

The alternative fabrication strategy in which pyrolysis was performed before the release of the resonators also gave positive results only in specific cases. The overall results are recapitulated in Figure 3.4.

Figure 3.4a shows a doubly-clamped SU-8 resist beam after pyrolysis but before dry etching. The carbon structures were well defined and no significant dimensional change was observed. Apparently,

lateral shrinkage occurs mostly for features that are not in direct contact with the substrate such as the ones obtained with the “dry etch-pyrolysis” process described above.

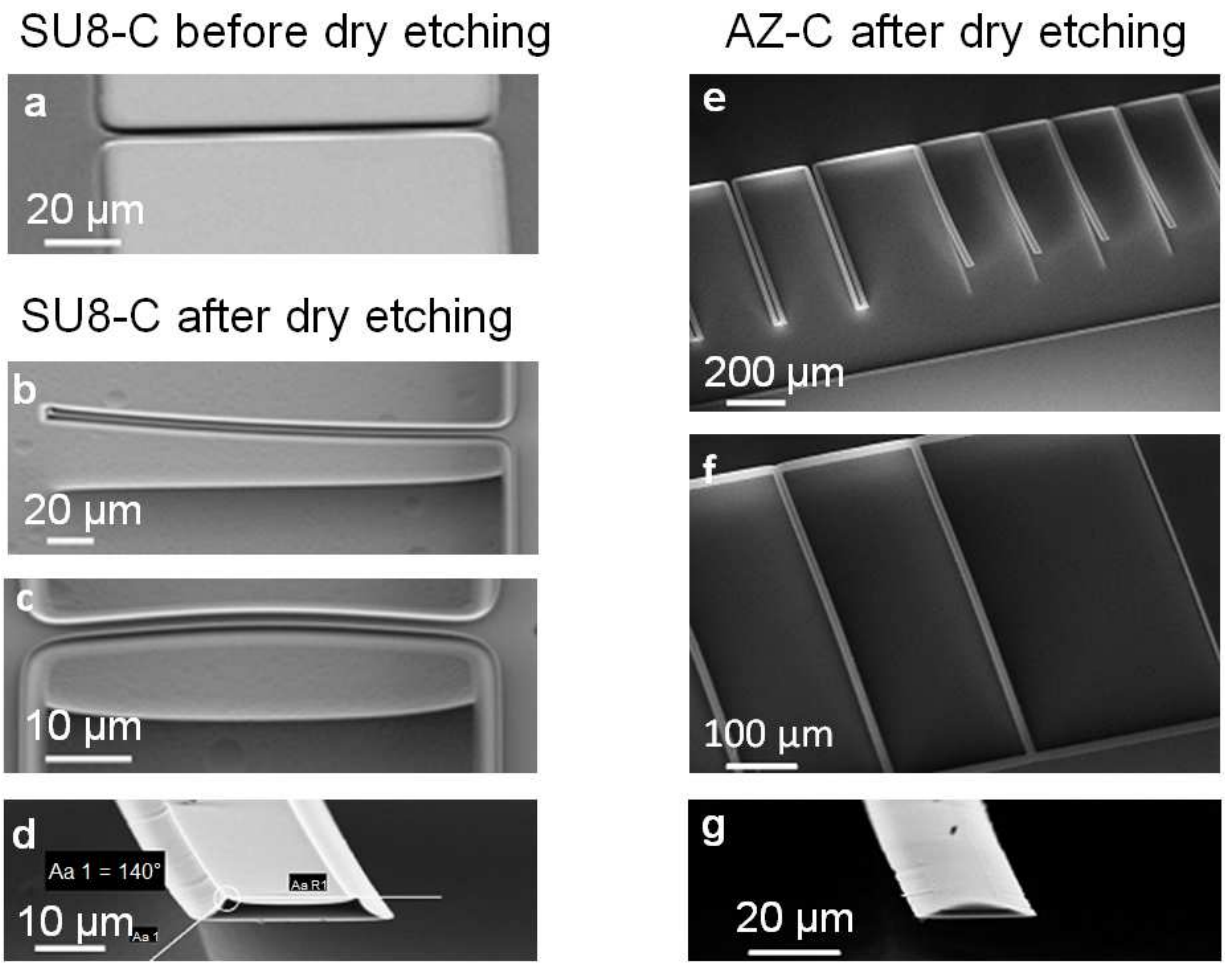

Figure 3.4: SEM pictures of the structures obtained with the “pyrolysis-dry etch” strategy. a) Unreleased SU8-C resonator (*L* = 100 µm, *w* = 14 µm) after pyrolysis; b) Released SU8-C cantilever (*L* = 200 µm, *w* = 14 µm); c) Doubly-clamped SU8-C beam (*L* = 100 µm, *w* = 14 µm); d) Curved sidewalls of the cross-sectional profile of SU8-C cantilever (*w* = 14 µm); e) The widest pyrolyzed AZ cantilevers (left**)**, *L* = 500 µm, *w* = 50 µm) were not released compared to the more narrow ones (right**)**, (*L* = 500 µm, *w* = 30 µm); f) AZ-C doubly-clamped beams (*L* = 500 µm, *w* = 14 µm (left) and *w* = 6 µm (right)); g) AZ-C cantilever (100 µm long, 14 µm wide) with a rounded profile due to the reflow of the photoresist. All dimensions are nominal mask dimensions.

Figure 3.4b-g show pyrolytic carbon microstructures after dry etching. Again here all microstructures except resonators with a width of 50 µm (Figure 3.4e-left) were completely released during dry etching. The singly-clamped cantilever beams obtained with this process showed no deformation at the clamping and only slight curvature for both SU-8 and AZ resist precursors (Figure

3.4b,e) even for devices with a length of 600 µm. However, doubly-clamped beams were clearly buckling after dry etching for both SU8-C and AZ-C (Figure 3.4c,f).

Figure 3.4d,g illustrate the beam profiles at the free-standing tip of cantilever beams of SU8-C and AZ-C, respectively. The curved sidewalls of the obtained resonators are a consequence of non-uniform lateral shrinkage of the photoresist during pyrolysis. Shrinkage at the bottom was smaller than at the top surface of the structures of interest because it was restrained by interaction with the substrate [45]. This was most evident for SU-8 structures (Figure 3.4d) [46], whereas for AZ, apparently, the reflow of the photoresist was possible and the cross-sectional profiles of the beams were more rounded (Figure 3.4g) [36].

In conclusion, the “pyrolysis – dry etch” process both for SU-8 and AZ resist precursors yielded singly-clamped pyrolytic carbon cantilevers.

3.2.2.2. Determination of pyrolyzed photoresist density and thickness

The basic unknown parameters after the fabrication process were density and thickness of obtained resonators. These values were necessary for calculating the Young’s modulus and tensile stress on the basis of the resonance frequency measurements. The thickness could not be determined precisely enough simply from the SEM pictures because of the complex relative position of the structures and the detector. The rounded edges and not exactly vertical side walls of resonators hampered such attempts as well. Therefore unpatterned photoresist films were processed on the 4 inch silicon wafers with identical fabrication parameters as described earlier for photolitography and pyrolysis. The wafer with AZ photoresist was not exposed to the UV light while the wafer with SU-8 underwent the flood exposure. The samples were weighed on a microbalance before spin-coating and after pyrolysis of the polymer films to determine the mass of the pyrolyzed photoresist. The carbon layer was mechanically removed by a metal blade, to avoid scratching the silicon, at ten points across the wafer and the film thickness was determined using a contact profilometer (DektakXT from Bruker, Billerica, MA, USA). The data was used to obtain the average thickness of the pyrolytic carbon. The uncertainties were evaluated based on the standard deviation of the mean assuming a t-distribution for a confidence interval of 95%. The film thickness for SU8-C was $h_{SU8\text{-}C}$=1.00±0.02 µm and forAZ-C was $h_{AZ\text{-}C}$=550±16 nm which is in good agreement with reported values of photoresist vertical shrinkage during pyrolysis [42,47]. The thickness together with the surface area of the silicon wafer was then used to calculate the volume of the carbon layer. Finally, the density was derived to be $\rho_{SU\text{-}C}$=1.52±0.06 g/cm^3 for pyrolyzed SU-8 and $\rho_{AZ\text{-}C}$=1.42±0.06 g/cm^3 for pyrolyzed AZ which is similar to values reporter previously by other research groups [40,41].

3.2.2.3. Resonance frequency measurements

The optical motion detection technique was chosen as the resonance frequency of the out-of-plane vibration was readout in the non-contact mode by laser Doppler vibrometer (MSA-500 from Polytec GmbH, Waldbronn, Germany) operating a laser wavelength of 633 nm. It is a very convenient tool for a nondestructive tests of nano- and micromechanical resonators. It works on the basis of Doppler effect and optical interference. If a wave is reflected by a moving object and detected by the

measurements system, the Doppler frequency shift can be recorded. To be able to determine the velocity of an object and amplitude of vibration, it has to be measured at a known wavelength which is done by using a laser interferometer [48,49]. The schematic technical realization of laser Doppler vibrometer is depicted in the Figure 3.5.

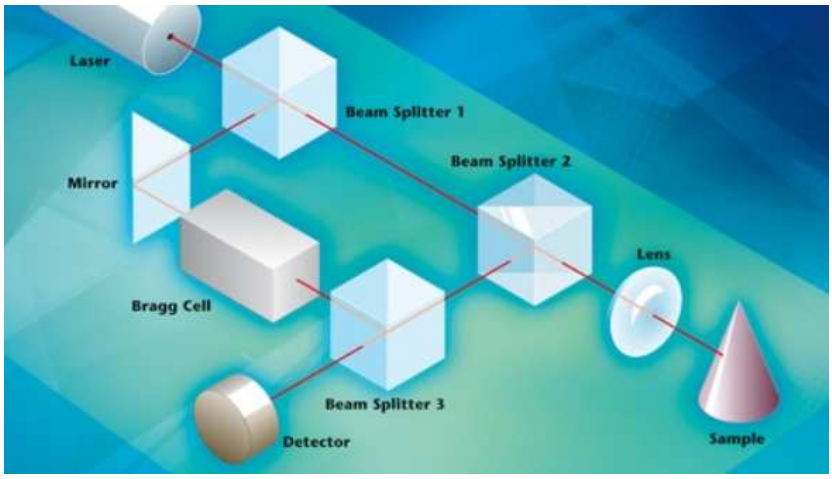

Figure 3.5: Working principle of laser Doppler vibrometer [48].

The beam of a helium neon laser is split by a beam splitter 1 into a reference beam and a measurement beam. After passing through a beam splitter 2, the measurement beam is focused onto the resonator surface, which reflects it. This reflected beam has now its frequency and phase changed depending on the velocity and displacement of the object under investigation. It is now deflected further by beam splitter 2, and then it is merged with the reference beam by the beam splitter 3 and finally is directed onto the detector. Meanwhile the reference beam is reflected by a mirror towards an acousto-optic modulator (Bragg cell) and ultimately reaches the beam splitter 3. As the path length of the reference beam is constant over time, a movement of the resonator generates a fringe pattern on the detector. This superposition of the reference and reflected measurement beams is used to extract the Doppler shift in the frequency. One complete dark and bright cycle on the detector corresponds to an object displacement of exactly half of the wavelength of the light used. Lastly, through the signal processing and analysis the vibrational velocity and displacement of the sample are provided.

The wafers with carbon resonators were manually diced using diamond scribing tool. Any silicon debris that remained after wafer breaking was removed by N_2 gas flow. Single chips were then glued through a carbon conductive tab on the piezo actuator (Noliac, Kvistgaard, Denmark) in the vacuum chamber with a transparent glass lid. The actuation signal was controlled by laser Doppler vibrometer software. The experiments were conducted at room temperature in high vacuum under a pressure of 1×10^{-5} mbar generated by membrane pump (PJ 15347-813.4 from Leybold GmbH, Cologne, Germany) and turbo pump (HiPace 80 from Pfeiffer Vacuum, Aßlar, Germany). The picture of the experimental setup is showed in Figure 3.6.

Figure 3.6: Experimental setup for studies of resonator vibrations.

3.3. Results and Discussion

Mechanical properties of pyrolytic carbon resonators are crucial for evaluation of their assessment of suitability in nano- and micromechanical systems. The performance of fabricated structures should be put into perspective and compared to the abilities of standard materials listed at the beginning of the chapter. The resonance frequency values of studied resonators enabled determination of pyrolyzed carbons Young's modulus in the case of cantilevers and tensile stress for strings. The theory described in the chapter 2 was used to achieve it.

3.3.1. Resonant behavior of cantilevers

The cantilevers fabricated with the "pyrolysis-dry etch" processing strategy with a nominal width of 30 µm, thickness of 1 µm and 550 nm for the SU-8 and AZ photoresists, respectively, and different lengths from 100 to 625 µm were used in the experiments. Figure 3.7 presents the measured resonance frequency and Q values as a function of the cantilever length. The moment of inertia about the y-axis of a beam with rectangular cross-section, with width *w* and height *h* is:

$$I_y = \frac{wh^3}{12}. \tag{3.1}$$

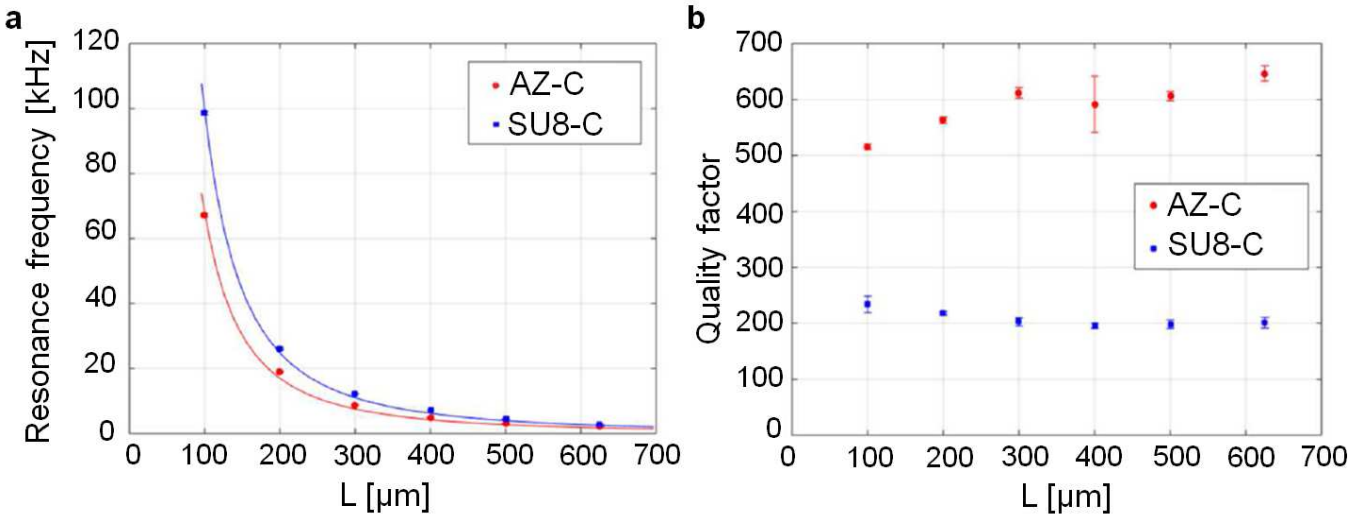

Figure 3.7: Relation between length and a) resonance frequency of the fundamental mode and b) Q of the carbon cantilevers fabricated with the "pyrolysis-dry etch" scheme using SU-8 and AZ photoresist precursors. Error bars represent a 95% confidence interval. Measurements were done on five cantilevers of each length and then averaged.

Applying it to the equation (2.26) and bearing in mind the relationship (2.41), the fundamental mode resonance frequency of singly-clamped cantilever is:

$$f_{1,c} \approx \frac{1}{2\pi}\frac{h}{L^2}\sqrt{\frac{E}{\rho}}\,. \tag{3.2}$$

Employing the above formula and experimental results of fundamental mode resonance frequency measurements the Young's modulus values were calculated (see Table 3.1).

Table 3.1: Values of Young's modulus of pyrolytic carbon cantilevers with different length. Errors represent a 95% confidence interval.

	SU8-C	AZ-C
L [µm]	**E [GPa]**	
100	58±12	82±11
200	65±12	105±15
300	72±15	114±16
400	77±16	110±15
500	74±15	113±16
625	74±15	124±17

The Young's modulus values are higher than values reported for pyrolyzed photoresist in the literature [41] that were obtained through nanoindentation method on a thin carbon film. These results demonstrate that the properties of the pyrolytic carbon strongly depend on the type of precursor and

pyrolysis conditions. It should be noted that the non-rectangular cross-section along with the unknown residual stress distribution may influence to some extent the applicability of the simple singly-clamped cantilever model described in the subsection 2.1.2.1 and eventually the calculation results. The calculated Young's modulus values are more or less identical for cantilevers with a length $L \geq 300$ µm. The values obtained for 100 and 200 µm long structures are lower due to the influence of the under-etched clamping, which is more important for shorter beams [50]. Therefore, the data for the two shortest cantilevers were excluded from the calculation of the averaged values, which are 74±8 GPa for SU8-C and 115±8 GPa for AZ-C.

The fact that AZ-C shows a higher Young's modulus than the SU8-C indicates that the AZ photoresist precursor results in pyrolytic carbon of higher quality. It is reflected in comparison of measured Q values for both photoresists. Generally, in nano- and micromechanical resonators energy can be lost to the surrounding medium, through the clamping to the substrate via elastic waves or through intrinsic dissipation energy mechanisms [22,51,52].

All experiments were done at a pressure of 1×10^{-5} mbar which was in the ballistic region where losses due to the interaction of the resonator with gas medium can be already neglected [51,53,54].

The clamping losses are an effect of resonator coupling to the support structure. An elastic wave excited by the shear stress of the beam is propagated and lost through the anchor of the resonator [55-57]. The clamping geometry plays a key role in the energy loss. Assuming that the supporting structure thickness h_b is thinner than the propagating elastic waves and that the material properties of the base and cantilever are the same, clamping losses for the fundamental resonance frequency mode can be estimated by [55]:

$$Q_{clamping}^{-1} \approx 0.95 \frac{w}{L} \frac{h^2}{h_b^2} . \tag{3.3}$$

In this case the silicon wafer thickness was h_b =525 µm which for the shortest cantilevers gives the $Q_{clamping}$ value of around 4×10^6. This is four orders of magnitude higher than the values measured during experiment, hence clamping loss does not limit the Q of pyrolytic carbon singly-clamped cantilevers.

Also, the fact that experimentally obtained Q values show no significant dependence on the cantilever length suggests that intrinsic losses dominate over the clamping loss. The intrinsic damping mechanisms cause that the ordered mechanical energy is transformed into the disordered internal energy of the system. They can be divided into fundamental or friction losses.

Fundamental losses are present even in the ideal frictionless materials and are associated mostly with Akhiezer damping [58,59] and thermoelastic dissipation (TED) [60-62]. The Akhiezer damping, also called phonon-phonon scattering, takes place as a result of heat flow between different phonon modes. The applied strain field in the vibrating solid material modulates the frequency of the thermal phonons. It leads to a temperature difference between different phonon modes and then each of them tends to relax towards the mean temperature value. It finally results in intramode heat flow and entropy generation leading to energy dissipation. The thermoelastic dissipation is based on the

irreversible heat flow in the resonator as well. Different portions of the resonator are forced periodically into compression and tension. As a consequence of thermoelastic coupling, an oscillating temperature field across the structure thickness is generated. This temperature gradient causes the heat flow and energy loss. The relevance of the Akhiezer damping is expected to be lower in comparison to TED at a size scale of investigated here cantilevers [63] therefore it can be ignored. The quality factor that should be observed for unstressed beam if the TED would be the dominant dissipation mechanism can be obtained from [60]:

$$Q_{TED}^{-1} = \frac{E\alpha^2 T}{\rho c_p}\left(\frac{6}{\xi^2} - \frac{6}{\xi^3}\frac{sinh\xi + sin\xi}{cosh\xi + cos\xi}\right), \tag{3.4}$$

$$\xi = h\sqrt{\frac{2\pi f_{1,c}\rho c_p}{2\kappa}}, \tag{3.5}$$

where α is the coefficient of thermal expansion, T is the temperature and c_p is the heat capacity. The pyrolytic carbon values of E and ρ were obtained before, the c_p is 710 J(kg K), the κ is 1.7 W/(m K), α is 78.5 ppm/K and T is 296.15 K [64]. For 1 µm thick SU8-C cantilevers Q_{TED} would be around 250 for the shortest resonators and more than 5000 for longest ones. Bearing in mind the lack of dependence between measured Q values and resonators length, the TED cannot be the main energy dissipation mechanism.

It means that friction losses are critical in this case. They originate from the material imperfections in the bulk or on the surface of the resonator. More precisely the energy is lost by the irreversible motion of atoms during vibration caused for example by defect dislocations in crystalline materials or molecular chain movement in amorphous materials [65,66]. Indeed pyrolytic carbon is a highly amorphous material with a distorted lattice structure with graphite-like areas [47]. Therefore, the dominant energy loss that limits Q is believed to be a result of internal material damping, such as friction between carbon layers.

3.3.2. Resonant behavior of strings

The strings fabricated with the “dry etch-pyrolysis” approach on the basis of AZ photoresist precursor with a nominal width of 14 µm, thickness of 550 nm and different lengths from 125 to 525 µm were used in the experiments. Combining equations of (2.34) and (2.41), the eigenmode resonance frequency of a string resonator is:

$$f_{n,s} = \frac{n}{2L}\sqrt{\frac{\sigma}{\rho}}. \tag{3.6}$$

A ratio between the fundamental resonance frequency mode (n=1) and higher resonance modes of 2.02±0.03 for the second harmonic (n=2) and 3.1±0.1 for the third harmonic (n=3) measured for 425 µm long AZ-C string resonators was very close to integer, clearly confirming string-like behavior (see Figure 3.8). Figure 3.9 shows the resonance and quality factor values as a function of string length. The fundamental mode resonance frequency values were to a good approximation proportional to the inverse of the length, as predicted by equation (3.6). The experimental data was used to calculate the

tensile stress in the strings utilizing equation (3.6) (see Table 3.2). Higher tensile stress was observed in shorter strings. This variation in stress could be the consequence of a different shrinkage of short strings during pyrolysis compared to longer ones. The resonance frequency values of 325, 425 and 525 µm long strings were fitted to equation (3.6) and the tensile stress calculated that way was 33±7 MPa.

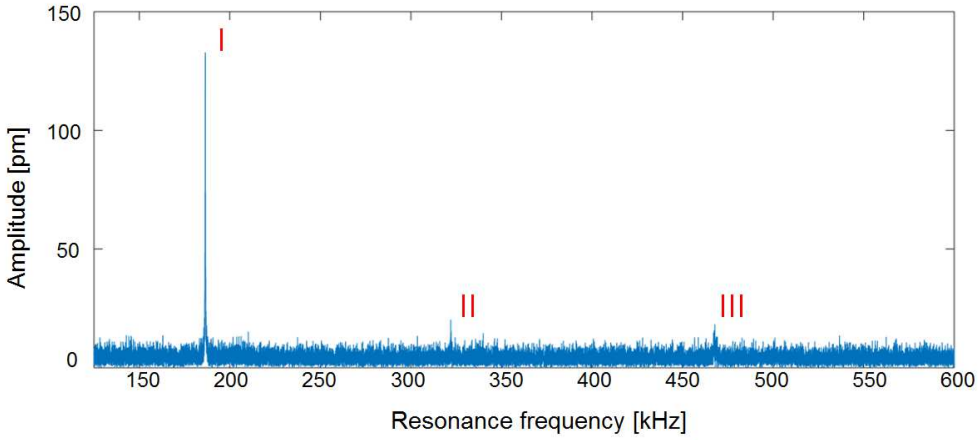

Figure 3.8: Frequency spectrum of 425 µm long AZ-C string resonator. First three resonance frequency modes are marked in red.

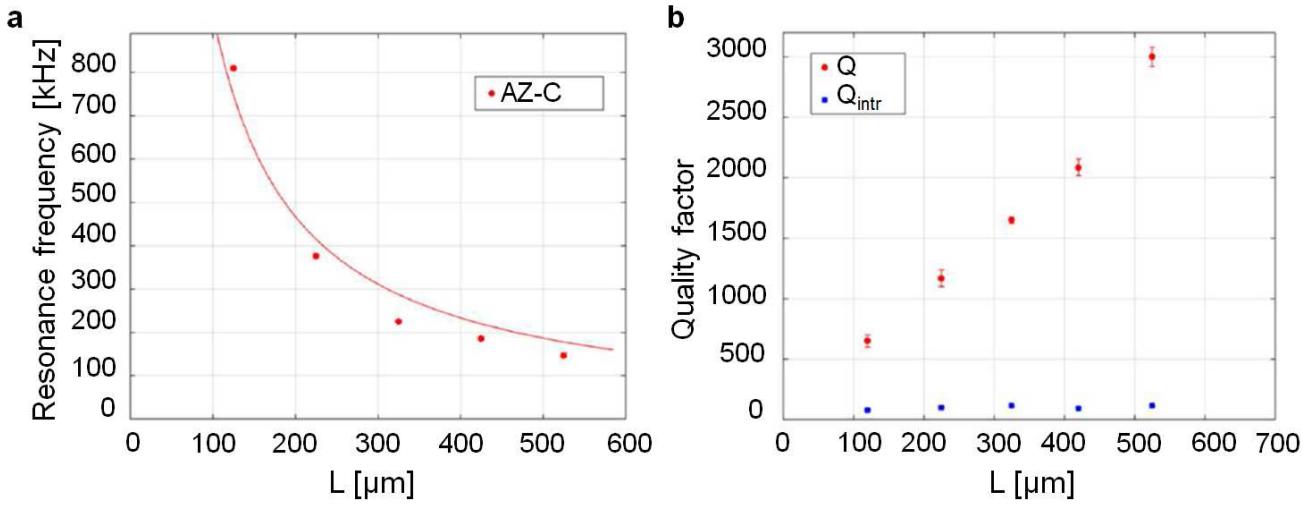

Figure 3.9: Relation between length and a) resonance frequency of the fundamental mode and b) Q of the carbon strings fabricated with the "dry etch-pyrolysis" scheme using AZ photoresist precursors. Error bars represent a 95% confidence interval. Measurements were done on five cantilevers of each length and then averaged.

In Figure 3.9b, the Q increases linearly with the string length, which is an effect of damping dilution. This phenomena explained in chapter 2 was shown also for string resonators made of silicon nitride [28,67] and SU-8 photoresist [66]. From equations (2.43) and (2.45) the quality factor of a prestressed doubly-clamped bean can be expressed as:

$$Q \approx \sqrt{3}\sqrt{\frac{\sigma}{E}}\frac{L}{h}Q_{intrinsic} \cdot \quad (3.7)$$

The $Q_{intrinsic}$ of pyrolytic carbon strings was obtained by inserting the values of the Young's modulus and tensile stress derived from experimental data to the above equation. It is assumed that it is a reasonable approximation to use the Young's modulus values calculated using experimental data of structures fabricated with the "pyrolysis-dry etch" strategy. This resulted in an average value of $Q_{intrinsic}$ for AZ-C resonators of 100±7. The intrinsic Q was relatively low and it was not significantly influenced by string length. This suggests that $Q_{intrinsic}$ is dominated by internal material friction, similarly as for singly-clamped cantilevers. The $Q_{intrinsic}$ value can directly be compared to the $Q_{intrinsic} \approx 600$ obtained for cantilevers (see Figure 3.7b). The material damping in the AZ-C cantilevers fabricated with the "pyrolysis-dry etch" process seems to be considerably lower than that of AZ-C strings fabricated with the "dry etch-pyrolysis" process. This could imply that the unpyrolysed photoresist is affected more by the dry etch step compared to the pyrolytic carbon, finally resulting in carbon of lower quality.

Table 3.2: Values of tensile stress of pyrolytic carbon strings with different length. Errors represent a 95% confidence interval.

AZ-C	
L [µm]	**σ [MPa]**
125	54±5
225	41±4
325	31±3
425	35±3
525	34±5

3.4. Conclusion

The different fabrication approaches of pyrolytic carbon resonators were demonstrated and acquired structures characterized. It can be concluded that it is possible to obtain nanomechanical cantilevers and strings through pyrolysis of photoresist. The developed fabrication process consists of only three main steps: photolitography, dry etching and pyrolysis, which allows for shorter fabrication time in comparison with common methods based on silicon or silicon nitride resonators. The order of the last two process steps had a decisive influence on the fabrication output, as summarized in Table 3.3.

For the "dry etch-pyrolysis" process strategy, dry etching resulted in structural deformation of the photoresist and buckling of the doubly-clamped beams. However, during pyrolysis the lateral shrinkage of the released photoresist effectively induced tensile stress in the suspended doubly-clamped beams. Nevertheless, only pyrolyzed AZ 5214e strings could be used in further experiments and displayed a string-like behavior. Singly-clamped cantilever beams could not be used due to excessive bending in the clamping area.

For the “pyrolysis-dry etch” fabrication strategy, structures were first pyrolyzed and then released by dry etching. No change of the lateral dimensions was observed except for an alteration of the beam cross-section. The doubly-clamped structures were not stretched during pyrolysis and buckling was observed. As a consequence, these devices could not be used as string resonators. However, the singly-clamped cantilevers showed minimal bending and could be used for characterization of the Young’s modulus of pyrolytic carbon.

Table 3.3: Summary of the overall fabrication output for the two different process strategies with the two precursor materials.

	Cantilevers		Strings	
Photoresist precursor	SU-8 2005	AZ 5214e	SU-8 2005	AZ 5214e
“dry etch-pyrolysis”	✗	✗	✗	✓
“pyrolysis-dry etch”	✓	✓	✗	✗

It is important to compare derived mechanical properties of fabricated structures to other materials commonly used for fabrication of resonators. The Young’s modulus values for pyrolytic carbon were calculated to be 74±8 GPa for the SU-8 and 115±8 GPa for AZ 5214e precursor. These values are much higher than for polymers with 4 GPa for SU-8 [66] but significantly lower than for silicon nitride resonators with 240 GPa [67]. Due to the amorphous structure of pyrolytic carbon with a high internal friction the fabricated cantilevers had moderate Q values of several hundred, which is better than 60 for SU-8 [66] and obviously less than for silicon nitride [67]. The tensile stress in pyrolytic carbon string resonators was determined to be 33±7 MPa. It is slightly higher than for strings made of SU-8 with 20 MPa [66] but lower than for silicon nitride, where tensile stress can reach 200 MPa for low stress and 900 MPa for high stress structures [67]. The Q values of strings have increased approximately linearly with length as predicted by the damping dilution model with maximal values of up to 3000 for 525 µm strings which is one order of magnitude higher compared to the Q values measured for cantilevers. Again this value is higher than SU-8 stringlike doubly-clamped microbeams that showed Q of 720 for around 300 µm long structures [66] and orders of magnitude lower than performance of silicon nitride ones [67].

Generally, with the presented Q values and Young’s modulus of more than 100 GPa, pyrolytic carbon is a promising alternative material for the fabrication of micro- and nanomechanical resonators, allowing for a direct photoresist-based fabrication. Pyrolytic carbon has a density more than two times lower than SiN, which is an advantage in terms of, for instance, mass sensitivity. Even though SiN has substantially higher tensile stress [67], SiN string resonators with a tensile stress of 900 MPa and the same dimensions as pyrolytic carbon structures, would be just 70% more sensitive to attached mass distributed evenly over the entire resonator surface [8,22].

There is also plenty of room for improvement, especially by the optimization of pyrolysis conditions and structure design. Additionally, the intrinsic electrical conductivity [41] allows for electrical integration for the development of novel carbon-MEMS/NEMS. The more detailed study of

electrical conductivity of carbon resonators could be the next step in research of this promising alternative to standard resonator materials.

Chapter 4

Photothermal nanomechanical infrared spectroscopy

The advancement in the photothermal IR spectroscopy with perforated nanomechanical membrane resonators was a principal goal of this work. Here the basic concepts of IR spectroscopy are reviewed. Afterwards, the attempts made so far of using nano- and micromechanical resonators as tools for photothermal IR spectroscopy are mentioned. Finally, the novel approach is presented in detail where SiN perforated membranes act as thermal sensors and porous filters for analyte sampling. Here the magnetomotive actuation and readout scheme is applied and makes a great step towards real-life applications of nanomechanical photothermal IR spectroscopy.

4.1. Introduction

Sir Isaac Newton's studies in the 17th century on the corpuscular theory of light laid the ground for the emergence of a crucial brunch of physical and analytical chemistry experimental methods [68] today known as spectroscopy.

4.1.1. IR spectroscopy

Spectroscopic methods rely on the observation of interaction of electromagnetic radiation with matter. They can be divided into emission and absorption methods in which information is obtained about the radiation emitted by the sample and information comes from the part of the radiation that has been absorbed by the sample, respectively [69,70]. The radiation scattered by the sample can also provide important information and is an object of interest of Raman spectroscopy that will not be talked over here. Generally IR spectroscopy examines the absorption of radiation associated with the excitation of vibrational levels of the molecules and can be particularly useful in sample identification.

The IR radiation covers the range of wavelengths from 780 nm to 1 mm. In practice, the most relevant region for spectroscopy measurements, the so-called fingerprint region, is in the mid-IR range from 2.5 µm to 25 µm, which corresponds to the wavenumber values from 4000 cm^{-1} to 400 cm^{-1}.

The internal energy of molecules can be expressed in various forms: as translational energy associated with disordered movement of molecules, the rotational energy resulting from the rotation of the molecules around their own axis, vibrational energy associated with the oscillations around the equilibrium positions of the atoms of the molecules and the energy of the electron, which includes the kinetic energy of the motion of electrons in the molecule and the potential energy of the interaction of

electrons with nuclei and neighboring electrons. The absorption of IR radiation causes a change in rotational and vibrational energy of the molecule. The shape of the spectra in the IR wavelength range for solids and liquids depends mainly on the vibrational excitation, because the rotation of the molecules is in this case partially or completely inhibited by intermolecular interactions. Spectra of solids and liquids are therefore called vibrational spectra, while the spectra of the molecules in the gas phase are called rotary-oscillation spectra due to the great freedom of both rotation and oscillation of the particles. Vibrations of polyatomic molecules are more complex, but they can be represented as a superposition of a number of basic vibrations that are in phase and of the same frequency, called normal vibrations. Among them two basic types can be distinguished: stretching vibrational modes associated with the change of bond lengths and bending vibrational modes resulting from the change of angles between bonds during the movement in the plane or out of the plane of the bonds. Each of the vibration modes may also be symmetrical or asymmetrical. The number of degrees of freedom of the molecule is equal to the sum of degrees of freedom of constituent atoms. Each atom has three degrees of freedom of movement. Thus, a molecule consisting of *n* atoms has *3n* degrees of freedom. In the case of nonlinear molecule, three of these degrees of freedom are translational and three are rotation. The remaining *3n-6* degrees of freedom describe the normal vibrational modes. Linear molecules have only two rotational degrees of freedom, so the vibration corresponds to *3n-5* normal modes (see Figure 4.1).

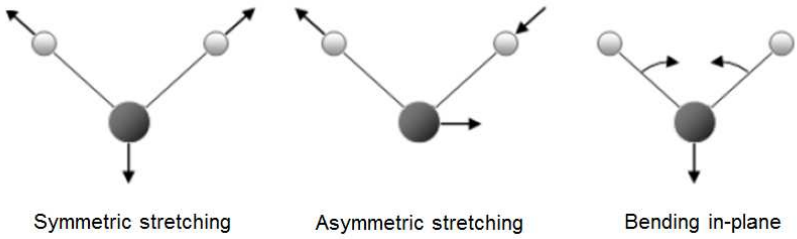

Figure 4.1 Normal **v**ibrational modes of a nonlinear water molecule.

The interaction between diatomic molecule and electromagnetic radiation can be understood by using the model of harmonic oscillator, which can be a system of two masses that represent atoms joined by a spring. According to a Hooke's law the vibration frequency *v* of such oscillator is:

$$\nu = \frac{1}{2\pi}\sqrt{\frac{k}{m_r}}\,, \tag{4.1}$$

$$m_r = \frac{m_1 m_2}{m_1 + m_2}\,, \tag{4.2}$$

where *k* is the spring constant and m_1 and m_2 are the masses of atoms. The energy of harmonic oscillator *E* is quantized:

$$E = h\nu\left(n + \frac{1}{2}\right)\,, \tag{4.3}$$

where *h* is the Planck constant and *n* is the quantum number equal (0,1,2,…). The interaction between the IR radiation and harmonic oscillator is possible only if selection rules are met. The energy of a photon of electromagnetic radiation that can be absorbed by a molecule must correspond to its difference in energy levels which is $\Delta E = \pm h\nu$. In the case of harmonic oscillator only absorption or emission transitions with a single change of quantum number $\Delta n = \pm 1$ are allowed. It accounts for fundamental absorption bands that appear in the IR spectra of molecules. The wavelength at which a molecule absorbs radiation fits the position of the absorption peak and provides information about the specific functional groups it consists of. The model of anharmonic oscillator can be used to explain transitions when a molecule absorbs at once a multiply of *hv*, which results in overtones in the IR spectrum.

The intensity of the bands can be expressed by the transmittance *T* or the absorbance *A*. The transmittance is the ratio of the intensity of light transmitted through the sample to the light intensity incident on the sample. The absorbance is the inverse of the decimal logarithm of transmittance:

$$A = log_{10}\left(\frac{1}{T}\right). \tag{4.4}$$

Nowadays, the two main IR spectrometer types are dispersive and Fourier transform (FT). The dispersive spectrometer consists of three basis parts: a radiation source (usually a silicon carbide bar called Globar heated up to 1100°C), a monochromator and a detector (thermal or photonic). The monochromator is an optical system in which the radiation is dispersed by a prism or diffraction grating and then the light of a specific wavelength can be extracted. It is done by using slits with adjustable width and mirrors. The light beam passes through the sample and finally reaches the detector. The main drawback is the fact that sample is irradiated with monochromatic light so the measurement over a broad spectrum is very slow. This issue was overcome in the FTIR spectrometer in which monochromator is replaced typically by a Michelson interferometer (see Figure 4.2). The crucial element here is the movable mirror. When it moves at a constant speed, the intensity of incident radiation on the sample varies, as two light beams have different distance to the sample and interfere with each other. On the basis of the signal from the detector, an interferogram is created. It is a record of interference intensity signal as a function of a scanning time when the mirror was moving. A Fourier transformation converts later the received spectrum from a function of time to a function of wavenumber. The measurement is much faster and more sensitive using this approach.

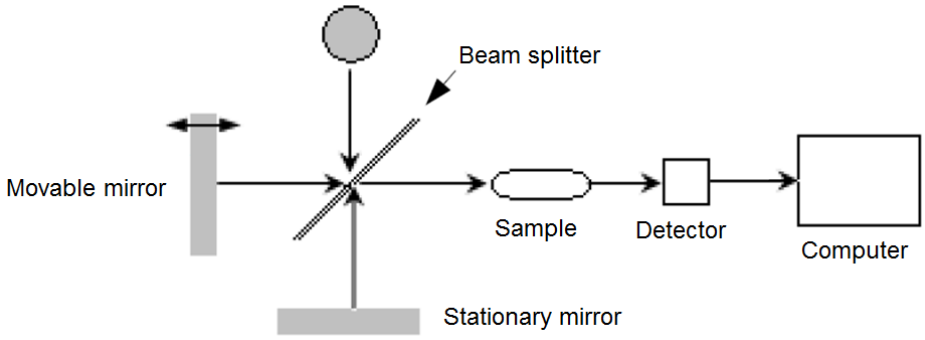

Figure 4.2 Schematic of FTIR spectrometer.

There are also two elementary experimental techniques, namely transmission and reflectance. Transmission methods rely on the measurement of the radiation intensity after passing through the sample. The decrease in the intensity for specific wavelength shows the absorption of radiation and can reveal the bonds present in the sample. This method however requires sample preparation as not all materials are transparent in the IR region. Gases and liquids can be placed in the cuvette made of potassium bromide (KBr) or sodium chloride (NaCl) that have a good transparency for IR light. Spectra of solids can be measured in the KBr pellets. Only if the sample is sufficiently thin the transmission spectrum can be obtained directly.

Reflectance methods are focused on measurement of the radiation reflected from the sample. Different approaches can be used, depending on the sample surface and type of light reflection. For example, a very common technique is the attenuated total reflectance (ATR) IR spectroscopy that uses the phenomenon of total internal reflection. The IR beam has a limited path length in the sample and experience only low attenuation even in highly absorbing media. This IR spectroscopy method was used as a reference for NAM-IR experiments.

The IR spectroscopy is used in research as well as in industry and has a vast variety of applications. First of all, it can be used in identification of functional group and structure elucidation of organic and inorganic molecules. Moreover, the identification of the substances is possible as the probability that any two compounds will produce identical spectra is almost zero. It is a valuable technique in studies of various types of materials. In the case of polymers IR spectroscopy can be used for their identification and characterization [71,72], for monitoring of polymerization reactions [73], for investigation of surface [74,75] and structural [72,73] properties including branching and crystallinity and for studies on polymer degradation [76]. For biological samples lipids and their conformation [77,78], proteins and peptides [79-81], nucleic acids [82,83] or even clinical samples [84,85] can be inspected. Apart from that, it is gaining popularity in food [86], pharmaceutical [87] and agricultural [88] industries.

IR spectroscopy is a well-established technique and numerous types of instruments are commercially available. However, the main limitations of this analytical method are still the need for relatively large sample amounts and troublesome sample preparation. Usually, up to few mg of sample is needed for a single FTIR measurement [89]. This can be a major challenge, particularly in the process of new drug development where the sample availability can be strongly limited because of very high costs [90]. In addition, sample preconcentration and such procedures as drying and KBr pellet formation are not only time-consuming [91] but may contribute to analysis errors [92] as well.

4.1.2. Photothermal IR spectroscopy

Another approach to determine the energy absorbed by the sample is to measure the temperature change of the sample induced by the irradiation with IR light [93]. In the first historically conducted experiments the temperature change was measured by a thermistor while monochromatic light was focused on the sample surface [14]. This method can be useful especially for opaque and highly scattering samples that present difficulties both in transmission and reflection based techniques [94]. Furthermore, it can improve the spatial resolution of measurement on the sample, as the conventional

IR spectroscopy methods are diffraction limited whereas for modern photothermal IR spectroscopy the limit is defined by the size of the contact between a probe and a sample [95]. The next step in development of this technique was a photothermal deflection spectroscopy, which is based on the photothermal deflection of a laser beam due to the change of the refractive index caused by heating of the sample by light [96]. Eventually the idea of photothermal deflection spectroscopy was realized using the micromechanical sensor in the form of bilayer cantilever that commonly is a SiN cantilever with a thin metal layer on top [15]. The analyte molecules in the vapor phase were first adsorbed on the surface of the sensor and then illuminated with a monochromatic IR light, similarly like in the dispersive spectrometer. The sample absorbs light of a certain wavelength corresponding to its specific molecular vibrations. As a result there is a heat flux into the cantilever and its temperature increases locally. The mismatch between thermal expansion coefficient values of the two mentioned materials causes the deflection of the whole structure that is later detected by the optical lever [97]. By using cantilevers with and without adsorbed molecules it is possible to obtain the IR absorption spectrum of the sample by plotting the differential cantilever deflection as a function of illumination wavelength [16]. The photothermal cantilever deflection spectroscopy was a crucial step in overcoming problem of poor selectivity of standard micromechanical cantilever sensors that rely on the fact that the deflection of the cantilever is directly proportional to the adsorption-induced surface stress [98]. The chemical selectivity was obtained by selective interfaces on the surface of the sensor but efficiency of this solution was limited [99,100]. Attempts done using arrays of cantilevers where each element was modified with partially selective interfaces [101] did not improve selectivity [100]. The chemical sensitivity was imparted to bilayer cantilever sensors by exploiting their exceptional sensitivity to temperature change [102,103]. This approach was used over the years in chemical process and environmental monitoring [104,105], detection of explosives [106,107] and biological analytes [108], polymer characterization [109] and identification of reagents in liquid using hollow cantilevers [110]. The main factors limiting the sensitivity and deteriorating performance of such devices are long-term drifts associated with temperature fluctuations and nonspecific physisorption of molecules on the surface [111] as well as vibrational and thermomechanical noise [112-114].

The vibrational resonance frequency of cantilever depends on its dimensions, mass and Young's modulus (see Equation 3.2). Therefore, molecular adsorption on the surface of the structure causes resonance frequency shift. It can be used for relative humidity measurements or adsorption rate studies [98]. However, this frequency approach for cantilevers lacks of selectivity and exposure to IR radiation cannot change it. In contrary, the resonance frequency of vibration of such nano- and micromechanical resonators as strings and membranes depends directly on their tensile stress that can be readily tuned by heating of the structures. The NAM-IR was first accomplished using string resonators and already better detection limit in comparison to bilayer cantilever deflection sensors was achieved [16,17,115]. The simple fabrication and robust detection scheme based on the resonance frequency measurements were featured. The vital advantage was also the simple and efficient analyte sampling method. Resonators were actuated by a piezo ring and actuation was done using laser Doppler vibrometer. The main disadvantage of NAM-IR technique was the alignment of IR laser beam on the string resonators with a width below 1 µm that required a great effort. Such difficulty could be avoided if membranes with larger surface area were used instead. Apart from that the experimental setup for NAM-IR with strings was fully dependent on the optical readout. The expensive and bulky

laser Doppler vibrometer impeded the expansion of this method outside the specialized laboratory. Membranes allow for a straightforward implementation of purely electrical actuation and readout schemes where laser Doppler vibrometer is not necessary anymore. All of these aspects will be elaborated throughout the rest of this chapter.

4.2. Methods

The project demanded fabrication of perforated membranes with electrodes. The existing process flow for plain membranes developed by Associate Professor Silvan Schmid and Ph.D. student Andrea Casci Ceccacci was used as a base and additional steps were introduced to obtain perforation and electrodes. Most of the cleanroom work was performed by Matthias Carnoy as part of his master project supervised by Associate Professor Silvan Schmid and me. Again all the fabrication was done in DTU Danchip cleanroom facility. Once the chips were ready, the sampling of analytes was done on the system used previously by former Ph.D. student in the Nanoprobes group Shoko Yamada. Finally, measurements were conducted in two different experimental setups that would be discussed in detail later in this subchapter.

4.2.1. Fabrication

First the optimum material must be chosen for this specific membrane resonators application. A high photothermal frequency response as well as quality factor were required. From Equation 2.72 it is clear that the relative resonance frequency shift of a membrane increases with thermal expansion coefficient α, Young's modulus E, absorbed power P and Poisson's ratio v. It decreases with thermal conductivity κ, tensile stress σ, and structure thickness h. The quality factor is governed by Equations 2.43 and 2.46 and can be enhanced by damping dilution effect caused by high tensile stress. First of all, polymers have high thermal expansion coefficient [116], nevertheless they can be excluded as they have relatively low tensile stress [66] and Young's modulus [117]. In turn, although metals such as aluminium have considerable thermal conductivity [64] and substantial heat dissipation can be expected, they were successfully used as temperature sensors. Unfortunately, low tensile stress limited the quality factor and frequency resolution [11]. The remaining materials possible for fabrication in DTU Danchip cleanroom facility were stoichiometric (high stress) and silicon rich (low stress) SiN. These two materials have very similar values of thermal expansion coefficient, Young's modulus and thermal conductivity [118-123] but have different tensile stress levels. The stoichiometric SiN may have five times higher tensile stress than silicon rich SiN, with approximated values of 1100 and 230 MPa, respectively [67,124,125]. The stoichiometric SiN should have the best quality factor values but very high tensile stress would deteriorate the thermal sensitivity of the sensor. The silicon rich SiN was expected to take advantage of both high thermal sensitivity and resonance frequency resolution. The suitability of this material for NAM-IR has already been confirmed [125] and finally it was chosen for membrane resonators fabrication in this work.

The masks for three photolitography processes were designed using L-Edit 15 program, similarly as for the pyrolytic carbon resonators project. Precisely one hundred 7×7 mm chips were fitted on one wafer. Membranes had lateral dimensions of 500×500 µm and 1×1 mm and were perforated on the whole surface with 1 and 2 µm square holes organized in 1 and 2 µm grid. The four possible

combinations of perforation, grid and membrane sizes were applied. Part of the chips had three 10 µm wide gold (Au) electrodes that were used for magnetomotive actuation and readout scheme (see Figure 4.3). The double side polished 350 µm thick 4 inch silicon wafers were used as a substrate.

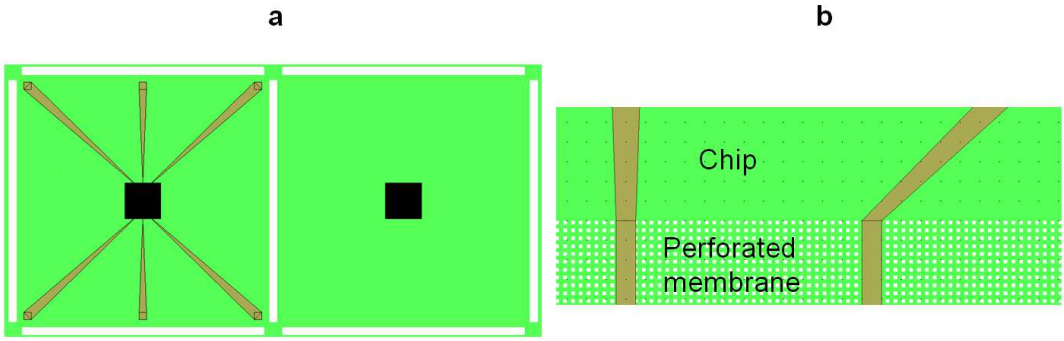

Figure 4.3 a) Illustration of chips with (left) and without (right) electrodes. The perforation appears as a black color. b) The zoom-in view of the central and one of the side electrodes.

The full fabrication scheme is presented in Figure 4.4.

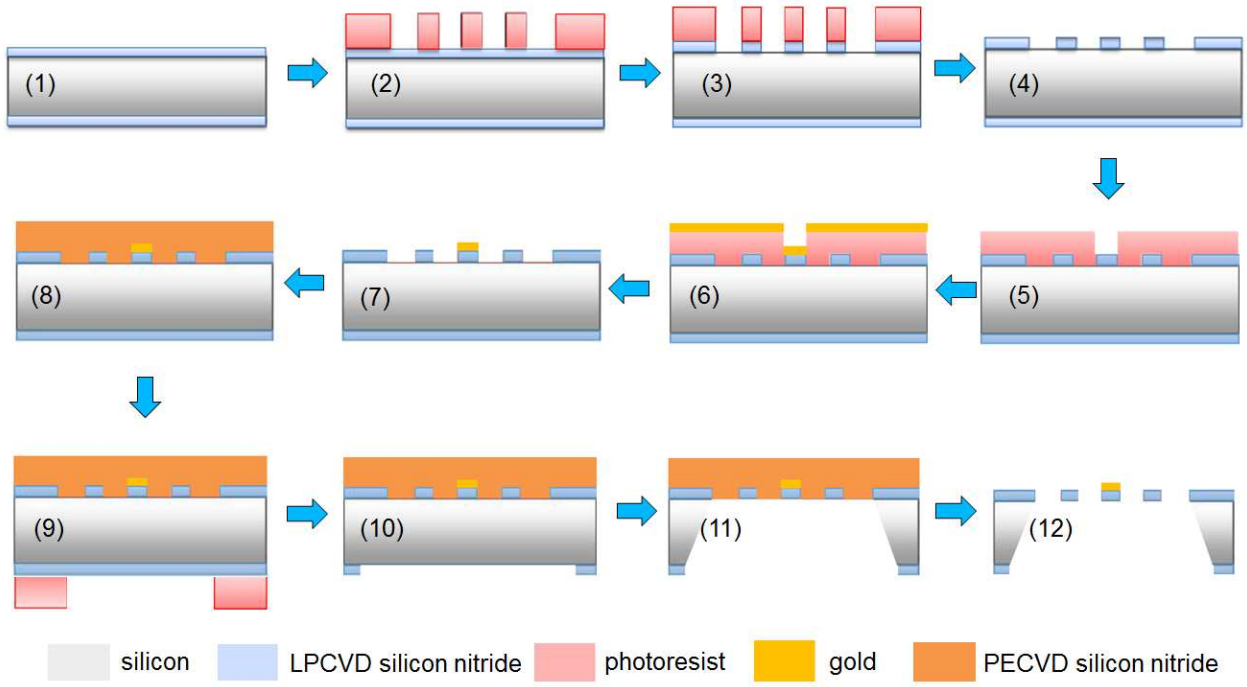

Figure 4.4 Fabrication scheme for perforated low stress SiN membrane resonators (see Appendix A).

It starts (1) with a deposition of 100 nm thick layer of silicon rich SiN on both sides of the wafers in the low-pressure chemical vapor deposition (LPCVD) furnace (Tempress Systems, Vaassen, The Netherlands). Under a pressure of 0.27 mbar and temperature of 845°C activated ammonia (NH_3) and dichlorosilane (H_2SiCl_2) gases diffuse to the wafer surface and react there to deposit a film. The

reaction byproducts in the form of hydrochloric acid (HCl) and hydrogen gas (H_2) are desorbed [126]. The stress in thin films is mainly generated due to the different thermal expansion coefficients of film and substrate and because of film grain growth when it is constrained by the substrate [127]. The ellipsometer (ESM-300 from J.A. Woollam Co., Lincoln, NE, USA) was used to measure the thickness of the obtained SiN layer. According to Danchip staff the silicon nitride should have tensile stress of the value around 215 MPa. Next (2) the wafers were dipped in BHF for 60 s to remove the native oxide and chemically pretreated with hexamethyldisilazane (HMDS) to promote the adhesion of AZ 5214e photoresist that was then spin-coated and 1.5 µm thick layer was formed. The photoresist was then soft-baked at 90°C for 60 s and patterned in mask aligner by hard contact UV exposure with a dose of 49 mJ/cm^2. After a development in AZ 351B diluted 1:5 in water for 60 s, rinsing with water for 3 min and 90 s drying in spin dryer, the perforation pattern was defined in the solidified photoresist. It served as a mask for a dry etching step (3) where silicon nitride was removed and perforation holes were opened. The silicon nitride was etched with a chuck temperature of 0°C for 45 s in the advanced oxide etcher (AOE) instrument (Multiplex ICP from STS, Newport, UK). It is a reactive ion etching (RIE) technique where reactive gases are excited and ionized by radio frequency field in a vacuum chamber. Ionic species are accelerated by the radio frequency field and collide with the sample reacting with the SiN and etching it. Such dry etching method has been chosen because of vertical motion of the ions that results in the anisotropic profiles and high selectivity against silicon which is an effect of using H_2 and octafluorocyclobutane (C_4F_8) gases in the process. Afterwards (4) the photoresist was removed in the plasma asher in which oxygen plasma combines with photoresist and ash formed that way is pumped away from the chamber. The goal of second photolitography step (5) was a definition of electrodes pattern for lift-off process and it was performed similarly as the first one but here the negative photoresist AZ nLOF 2020 was used instead. The proper alignment of the mask to the wafer with perforation was critical. The UV exposure dose was 70 mJ/cm^2 and wafers underwent post exposure bake in 110°C for 60 s and development in 351B developer for 60 s in automated developer machine (Gamma 2M from Süss MicroTec AG, Garching, Germany). Then the metal layer was deposited on the front side of the wafer (6) using a thin film deposition machine (QCL 800 from Wordentec, Shebbear, UK). It allows for electron beam evaporation of desired metal whose atoms are then transported in high vacuum to the wafer surface. The 50 nm thick layer of Au was deposited with a rate of 1 nm/s on top of the 5 nm thick adhesion layer of titanium (Ti). The wafers were then immersed in acetone bath for 3 h (7) which dissolved the photoresist and excess metal was removed. The front side of the wafer with defined electrodes needs to be protected from potassium hydroxide (KOH) wet etch that would be used to release the membranes from the back side of the wafer. It has been achieved (8) by deposition of SiN that has a low etch rate in the KOH (around 1 nm/min) in the plasma-enhanced chemical vapor deposition (PECVD) machine (Multiplex CVD 06541 from SPTS, Newport, UK). In contrary to LPCVD, here the pressure is elevated to 1.13 mbar and plasma is added in the chamber that together with reactant gases of silane (SiH_4), NH_3 and nitrogen (N_2) create the desired solid surface on the substrate. The films deposited by LPCVD show better uniformity and homogeneity [128] but this method could not be used as wafers with metal are forbidden for processing in the LPCVD furnace in order to avoid contamination. The last photolitography step (9) was performed with the same parameters as the first photolitography step, only the mask was aligned from the back side to the already existing structures on the wafer. Again

due to the metal contamination issues AOE could not be used for removing the silicon nitride on the back side of the wafer. The same principle of dry etching was applied (10) in the similar machine (part of Cluster System C010 from SPTS, Newport, UK) with reactive CHF_3 and N_2 gases. Next, the wet etching of silicon from the back side of a wafer (11) in KOH at a temperature of 80°C and concentration of 28% was performed for approximately 6 h. Eventually the protective silicon nitride layer was removed (12) in the 5% BHF solution during 10 min bath. Wafers were then left to dry in the fume hood and were diced with a diamond scribing tool.

The membrane fabrication yield was estimated to be around 90%. However, inspection of the wafers revealed that the definition of perforation holes should be optimized (see Figure 4.5) in terms of exposure dose and development time. The mask aligner uses mercury lamp as a UV light source so the exposure radiation has a wavelength of 365 nm. The resolution limit for this machine in hard contact exposure mode is around 1 µm. Therefore, the smallest perforation square holes with a nominal lateral size of 1 µm were not always correctly developed and part of such membranes remained unpatterned (see Figure 4.5a,b). On the other hand, the nominal 2 µm perforation holes experienced distorted shape (see Figure 4.5c,d). In the center of the wafer holes still had more quadratic shape, whereas on the chips located at the edge of the wafer the holes were completely circular. It can be explained by the proximity effects and not uniform UV light intensity across the wafer [129]. The resulting perforation holes on average had a diameter of roughly 2 µm for circular holes and edge length of about 2 µm for more quadratic holes.

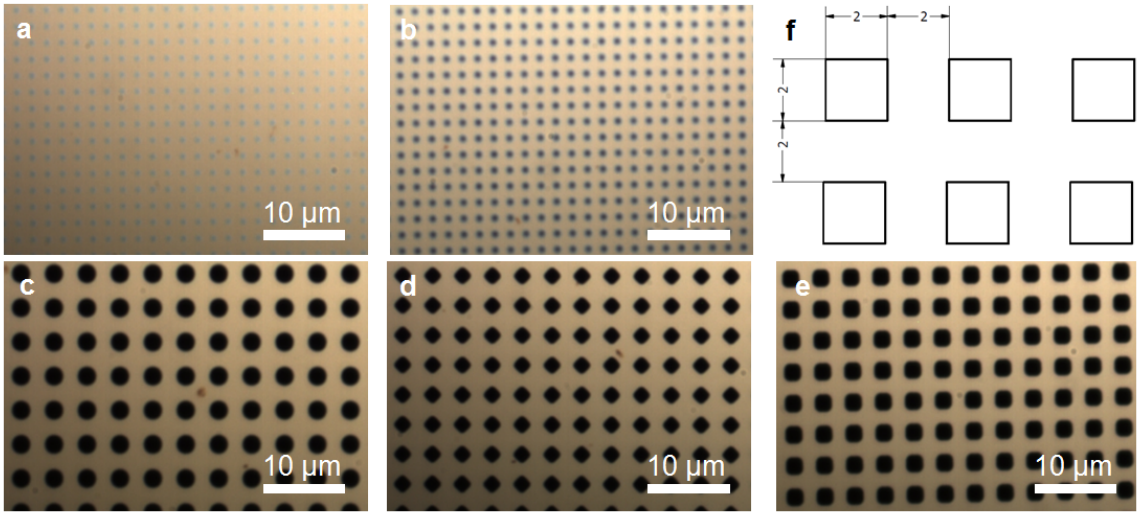

Figure 4.5 Pictures taken using optical microscope with 100 times magnification. a) and b) Membranes with nominal lateral size perforation holes of 1 µm in 1 µm grid. Part of the membranes remained unpatterned, the rest had circular holes with 1 µm in diameter. c), d) and e) Perforation holes shape in different parts of a wafer, the nominal size of 2 µm in 2 µm grid. Circular shapes c) observed on the edge of the wafer and quadratic shapes e) in the center. f) Drawing showing perforation holes organized in a grid.

4.2.2. Sampling

Definitely, the advantage of the NAM-IR over the photothermal cantilever deflection spectroscopy is the analyte sampling approach. In the latter method it was done by physically dipping cantilevers in

the solution, depositing a drop of the solution on the sensor surface or by using vapor deposition [104,106]. The NAM-IR with perforated membranes offers an efficient and fast sampling of analyte in the form of airborne nanoparticles by an air filtration-based technique [17,115,130].

The perforated membrane functions as a thin porous membrane filter and can collect sample nanoparticles that are streaming through it by three basic mechanisms that are assumed to act independently [131] (see Figure 4.6). Their theoretical analysis is complex but simplified equations can be derived and are accurate enough to show the trend of collection efficiency with sampling parameters.

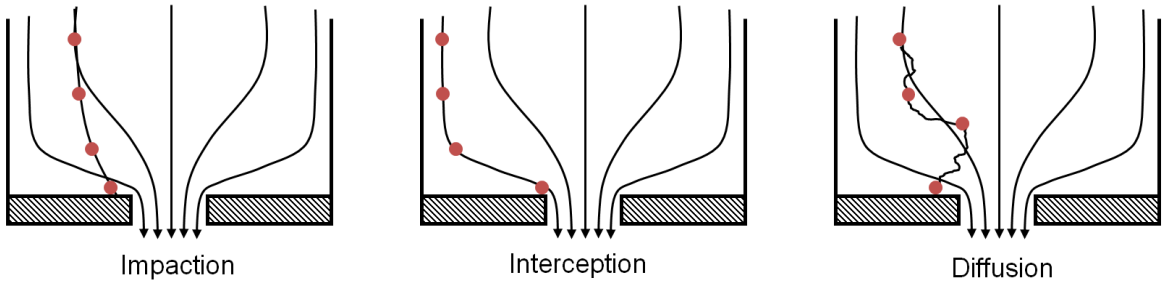

Figure 4.6 Three main mechanical collection mechanisms on the membrane porous filter that is exposed to an aerosol stream.

Impaction on the membrane surface occurs when a particle is unable to adjust quickly enough to the abruptly changing streamlines near the pore opening and eventually hits the filter. It happens for particles with large momentum which is an effect of large mass or high velocity. Interception takes place when the center of a particle following a streamline passes within a distance of the particle radius from the opening of a single hole. It is the only mechanism that is not a result of a particle departing from its original gas streamline. Finally, the Brownian diffusion of a particle may cause deviation from its nonintercepting trajectory and landing on the membrane surface.

The overall sampling efficiency E_S is a figure of merit of a porous membrane filter. It is defined as the ratio of number of particles deposited on the surface to the total number of particles that approach the filter and can be expressed as:

$$E_S = 1 - (1 - E_I)(1 - E_R)(1 - E_D), \tag{4.1}$$

where E_I, E_R and E_D are collection efficiencies due to impaction, interception and diffusion to the front surface of the filter, respectively.

Collection efficiency that is attributable to impaction assuming the steady and axisymmetric flow can be calculated as [132-134]:

$$E_I = \frac{2\varepsilon_i}{1+\xi} - \left(\frac{\varepsilon_i}{1+\xi}\right)^2, \tag{4.2}$$

$$\varepsilon_i = 2Stk\sqrt{\xi} + 2Stk^2\xi\exp\left[-\frac{1}{Stk\sqrt{\xi}}\right] - 2Stk^2\xi, \quad (4.3)$$

$$\xi = \frac{\sqrt{P}}{1-\sqrt{P}}, \quad (4.4)$$

$$Stk = \frac{2\rho_p r_p^2 U_0}{9\eta r_0}, \quad (4.5)$$

where P is the porosity of a filter defined as a ratio of open space in a filter matrix to the amount of volume taken by a filter media itself, Stk is the Stokes number, ρ_p is the particle density, r_p is the particle radius, U_0 is the face velocity, η is the dynamic viscosity of the flow and r_0 is the pore radius.

Collection efficiency due to interception assuming Poiseuille flow and neglecting the slip-flow phenomena is [133,135,136]:

$$E_R = (2N_R)^2, \quad (4.6)$$

$$N_R = N_r\left(1 - \frac{N_r}{2}\right), \quad (4.7)$$

$$N_r = \frac{r_p}{r_0}. \quad (4.8)$$

Diffusion to the inner pore wall of a filter can be disregarded because of the very small thickness of a membrane. Collection efficiency due to diffusion to the front surface of the filter is [134,137]:

$$E_D = 1 - \exp\left[\frac{-\alpha_1 \mathcal{D}^{2/3}}{1+(\alpha_1/\alpha_2)\mathcal{D}^{7/15}}\right], \quad (4.9)$$

$$\alpha_1 = 4.57 - 6.46P + 4.58P^2, \quad (4.10)$$

$$\mathcal{D} = \frac{D_p}{D_0 U_0}, \quad (4.11)$$

$$D_0 = \frac{r_0}{\sqrt{P}}, \quad (4.12)$$

$$D_p = \frac{k_B T}{6\pi\eta r_p}, \quad (4.13)$$

where α_1=4.5, $\mathcal{D}$ is the normalized particle diffusion coefficient, D_0 is the radius of the cylindrical flow approaching a pore, D_p is the particle diffusion coefficient, k_B is the Boltzmann constant and T is the temperature.

These models are valid only if the flow approaching a pore is laminar, which occurs at a low Reynolds number Re which can be derived from [132]:

$$Re = \frac{U_0 D_0}{\upsilon}, \quad (4.14)$$

where v is the kinematic viscosity of a flow.

Dedicated system for sampling of analytes on perforated membranes had been designed by Associate Professor Silvan Schmid and used during previous projects focused on NAM-IR (see Figure 4.7b) [17,125]. Compressed air was provided from DTU Danchip facility grid. The filtered air supply (3074B from TSI, Shoreview, MN, USA) removed oil, liquid droplets and fine particles from the incoming air. It had a built-in gas regulator valve allowed for precise pressure adjustments. Airborne nanoparticles were generated using a jet nebulizer (3076 from TSI, Shoreview, MN, USA). The cross-section of device is presented in the Figure 4.7a [138].

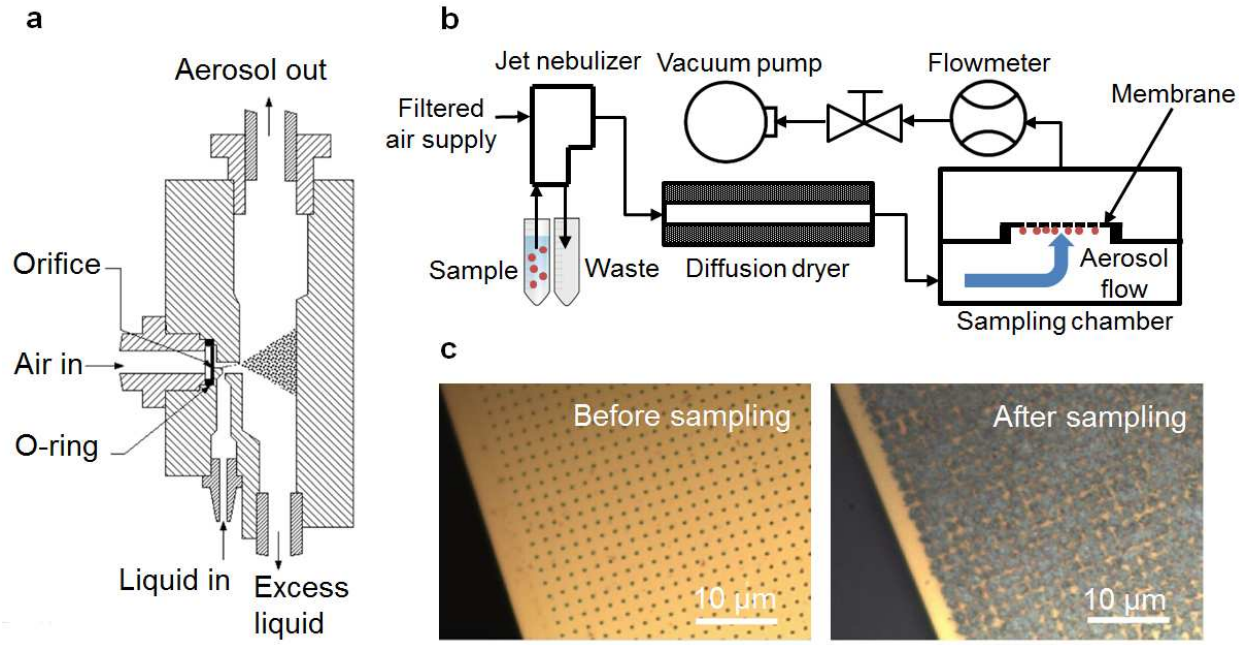

Figure 4.7 a) Cross-section of a jet nebulizer. b) Schematic of a sampling setup. c) Taken with 50 times magnification optical microscope pictures of a membrane with nominal 1 µm perforation in 1 µm grid before and sampling of indomethacin that was first dispersed in methanol.

Air under pressure expands through an orifice that is 0.34 mm in diameter to form a high velocity jet. Liquid with dispersed sample is drawn into the nebulizing section through a vertical passage and is then nebulized by the jet. Large droplets are removed by impaction on the wall opposite to the jet and excess liquid is drained at the bottom of the nebulizer assembly block. Aerosol left the instrument through the fitting at the top and went through the diffusion dryer with silica beads. It was then directed into the custom-made aluminium chamber where perforated membrane was spanned over the orifice covering it perpendicularly to the airborne nanoparticles flow, efficiently filtering them. From the other side of the chamber suction was applied by vacuum obtained from DTU Danchip grid as well. It increased the nanoparticles velocity and that way enhanced sampling efficiency on the membrane filter. The air flow was controlled by a valve (VFA-22-SSV from Dwyer, Michigan City, IN, USA) and measured by flowmeter (4100 from TSI, Shoreview, MN, USA). The size of nebulized particles was determined by a portable diffusion size classifier (DiSCmini from Matter Aerosol, Wohlen, Switzerland) which is based on the particle diffusion charging and sequential electrical measurements. Positive ions

are mixed with the aerosol and charged particles are then detected in two stages by electrometers. The first stage is a pile of steel grids on which small particles are deposited by diffusion. The second stage is a filter which intercepts all the other particles. The mean particle diameter size is obtained by analysis of the two currents measured on detection stages [139]. The average particle diameter can be measured with an accuracy of ±30% [140]. Inspection of membranes under microscope after sampling showed that nanoparticles were captured exclusively on the perforated area and could not be found close to the edge of the membrane (see Figure 4.7c).

Assuming the circular perforation holes with a diameter of 1 µm and 2 µm, the porosity values of both membrane types were calculated to be 0.24±0.02. The average particle radius was measured to be 25 nm. The sampling was performed with a flow rate of 1 l/min. The total perforation holes area for 1×1 mm membrane was around 0.2 mm^2 which together with mentioned flow rate gives face velocity of 84.4±8.3 m/s. The density of the analyte was 1.32 g/cm^3 [141], the dynamic viscosity of flow for air was 1.8×10^{-5} Pa·s [134], the kinematic viscosity was 1.5×10^{-5} m^2/s [132] and the temperature was 295.15 K. Taking into account Equations from (4.1) to (4.13) the overall sampling efficiency of a membrane with nominal 1 µm and 2 µm perforation holes was 67±23% and 59±21%, respectively with overwhelming dominance of impaction-driven sampling. The membranes with lateral dimensions of 500×500 µm and equivalent perforation would have increased overall sampling efficiency for 12% and 6% due to higher face velocity. It is a major improvement in comparison to estimated total sampling efficiency on the order of 10% reported for string resonators that act as single filter-fiber [115]. According to Equation (4.14) Reynolds number for bigger membrane was 12 and 46 for smaller one which means that flow around the pore was laminar. It should be noted that it is virtually impossible that 67% or 59%, depending on the perforation size, of the sample that was first in dispersion would be collected on the membrane. Part of the nebulized airborne particles would be lost in the sampling system, mainly in the nebulizer block itself and rubber tubing used for sample transport towards the membrane filter. Therefore, the amount of sample compound dispersed in liquid and nebulized is significantly higher than the quantity actually needed for a reliable experiment.

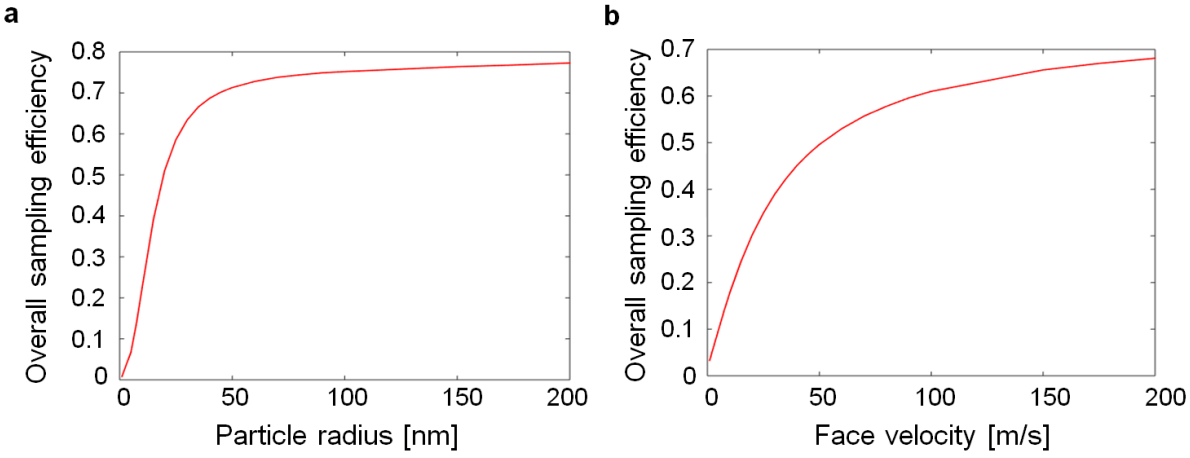

Figure 4.8 Overall sampling efficiency of a 1×1 mm membrane with 2 µm perforation holes in 2 µm grid in the case of constant a) face velocity and b) particle radius. Data obtained with face velocity of 84.4 m/s and particle radius of 25 nm.

Perforated membrane resonators have a great potential to be used as sensors for detecting contaminations in research laboratories or pharmaceutical plants as they are capable of capturing nanoparticles directly from air and can be placed for example in air purification and ventilation systems. Nanoparticles size and their momentum have a decisive influence on the overall sampling efficiency of a specific membrane (see Figure 4.8). Simulation shows that it could be raised simply by increasing the air flow in the system when other conditions are constant. The 100% collection efficiency can however only be obtained for particles bigger than the perforation holes.

Experiments confirmed that perforated membrane saturates over prolonged filtering and when it is completely clogged no more sample nanoparticles can be captured. Figure 4.9 presents resonance frequency change of a 1×1 mm membrane with 2 µm holes in 2 µm grid due to sample adsorbed on its surface. In this case the membrane saturated after approximately 20 min of sampling with 90 µM indomethacin dispersion in methanol with nebulizing pressure of 4 bar and flow rate of 1 l/min. It is assumed that this additional mass does not alter the structure stiffness. It can rather be interpreted as an increase of mass density of the membrane material.

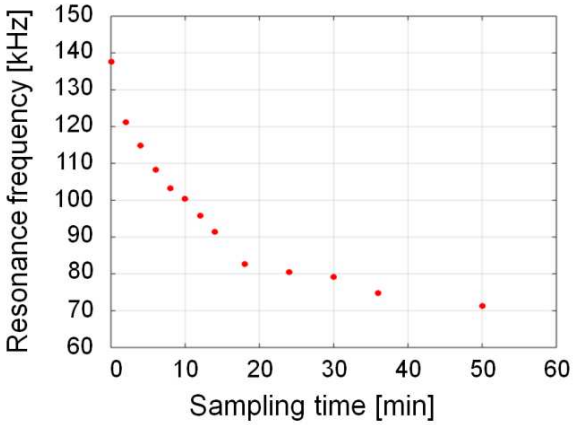

Figure 4.9 Resonance frequency of a 1×1 mm membrane with nominal 2 µm perforation holes in 2 µm grid changes during sampling if indomethacin.

4.2.3. Experimental setups

Two completely separated experimental setups were used to conduct the measurements. As it has been already mentioned they rely on different actuation and readout techniques. The comparison of their performance is essential in terms of choosing the most promising path of NAM-IR development.

4.2.3.1. Optical readout setup

First setup, similarly to the one used for studying pyrolytic carbon resonators, was based on optical readout and piezo actuation. However, modifications in the general setup design and introduction of new instruments were necessary (see Figure 4.10). The sensor chip was glued on the piezo ring actuator (Noliac, Kvistgaard, Denmark) by double-sticky carbon tape inside an aluminium vacuum chamber designed by Shoko Yamada [125]. Piezo actuator was connected to actuation

control by electrical feedthrough. The chamber had glass window on the top and zinc selenide (ZnSe) window that is transparent for IR radiation on the bottom. The readout laser was directly focused on the top side of the membrane and the IR laser was focused on the back side of the membrane where the analyte was collected using an Au coated parabolic mirror with 2 inch reflected focal length (MPD254254-90-M01 from Thorlabs, Newton, NJ, USA). The IR light was emitted by a tunable quantum cascade laser (QCL) (LaserTune from Block Engineering, Marlborough, MA, USA) in a mid-IR range of wavenumber from 768 cm^{-1} to 1953 cm^{-1}, which covers the so-called fingerprint region of most of chemical compounds.

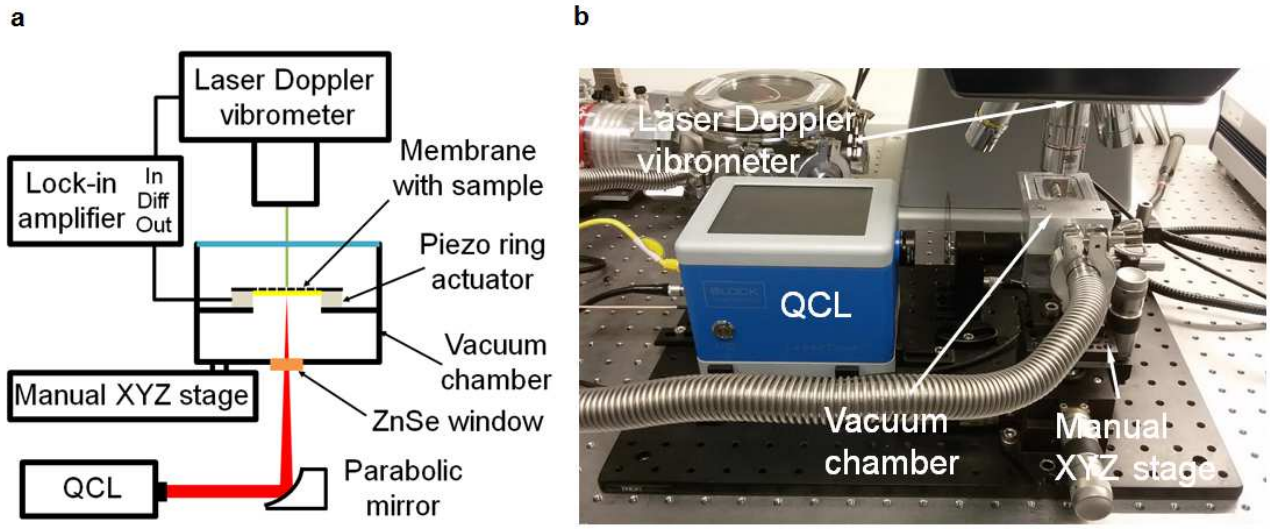

Figure 4.10 Schematic a) and picture b) of the experimental setup with optical detection of out-of-plane membrane vibration.

The QCL used in the setup is a semiconductor laser that has a very wide gap-free tuning range, can reach a peak power of approximately 20 mW depending of the operating parameters and is equipped with laser pointer which makes it a suitable IR radiation source for the purpose of these experiments. It consists of a quantum cascade chip that in turn is comprised of numerous of alternating layers of semiconductor material grown by molecular beam epitaxy that form quantum energy wells and confine the electrons to particular energy states. So a quantum well is essentially a semiconductor with relatively low band gap energy sandwiched between semiconductor layers with high band gap energies. The thickness is typically a few nanometers and electrons are confined primarily to the center part of the sandwich. Each electron traverses the lasing medium in transitions from one quantum well to the next, driven by the voltage applied across the device. At precisely engineered locations called the ‘active regions’ the electron transitions from one valence band energy state to a lower one and in the process emits a photon. The electron continues through the structure and when it encounters the next active region it transitions again and emits another photon. The output wavelength is determined by the structure and thickness of the layer rather than the lasing

material which means that the device fabrication can tailor the wavelength more freely than in for example diode lasers [142]. The quantum cascade chip serves as the laser gain medium in the external cavity Littrow configuration with back extraction and with a grating as the tuning element. The angle of the grating selects the wavelength of the diffracted light, which couples back into the QCL chip and creates a laser radiation at a single wavelength [143] (see Figure 4.11a,b).

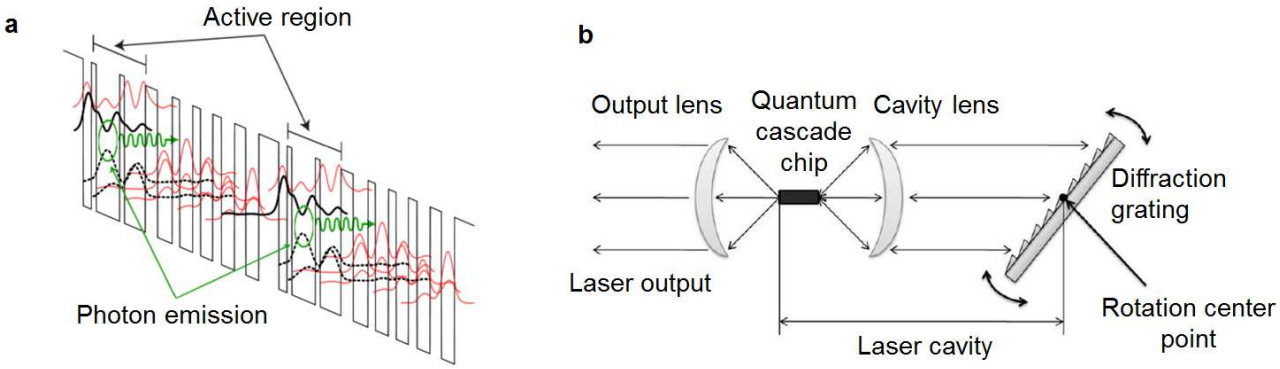

Figure 4.11 a) Quantum cascade conduction band diagram showing electron transitions. b) Principle of operation of tunable QCL [144].

The experiments could be carried out in medium vacuum at a pressure of 1 mbar or in high vacuum at a pressure of 1×10^{-5} mbar. The vibration of a membrane was readout by a laser Doppler vibrometer and detuning of the resonance frequency was recorded by a lock-in amplifier (HF2LI from Zurich Instruments, Zurich, Switzerland) with a bandwidth of 100 Hz and sampling rate of 255 S/s.

It is an instrument capable of detection and measurement of very small alternating current (AC) signals at a presence of an overwhelming noise background. The direct current (DC) output proportional to AC signal under investigation is provided through a conversion performed by a special rectifier called phase-sensitive detector (PSD). Only the signal of interest is rectified while the noise or interfering components which may accompany it are suppressed. The PSD can recognize the signal because it is supplied with a reference voltage of the same frequency and with a fixed phase relationship to that of the signal. This reference signal ensures that the instrument will keep track of any changes in the frequency of the signal of interest, since the reference circuit is locked to it [145,146].

The piezo ring actuator was fed from the lock-in amplifier with a voltage of 100 mV. The vacuum chamber was mounted on the manual translation stage to facilitate alignment of the IR laser spot on the centre of the membrane. Exactly the same approach has already been utilized for photothermal IR spectroscopy with nanomechanical string resonators [17,115,125] with a width of around 1 µm, what made alignment of the IR laser very troublesome and laborious. Of course this issue was overcome by replacing strings with membranes. Apart from that, it turned out that fixing chips on the piezo actuator with a double-sticky carbon tape can make it difficult to reproduce results. Finally, a laser Doppler

vibrometer is expensive and bulky equipment that is hindering the application of this technique outside a specialized laboratory.

4.2.3.2. Magnetomotive readout setup

The solution to all noticed disadvantages of the primary experimental setup may be a magnetomotive transduction scheme. It is a well-known actuation and readout approach that facilitated the development of the first nanomechanical resonators offering low complexity and good performance [18]. In this method resonator with length *L* and electrode on top is placed perpendicularly to a uniform magnetic field with induction *B*. Alternating current $I_L(t)$ is passed through an electrode and thereby the actuating Lorentz force $F_L(t)$ is generated:

$$F_L(t) = BLI_L(t) \, . \tag{4.15}$$

The motion of a conductor through the magnetic field induces the electromotive force $\varepsilon_{EF}(t)$ along the structure:

$$\varepsilon_{EF}(t) = \zeta BL\frac{du(t)}{dt} \, , \tag{4.16}$$

where ζ is the constant of order unity equals 0.83086 for a double-clamped beam fundamental mode and $u(t)$ is a displacement of the electrode. The force $F_L(t)$ depends linearly on the magnetic induction *B* which means that beam velocity is proportional to *B* as well. Therefore, voltage signal $\varepsilon_{EF}(t)$ scales as B^2. It was reported that external electrical circuit may affect the resonator performance [147]. In the case of low external circuitry impedance load on the resonator, in the high magnetic field the electrical damping mechanisms would shift the resonance frequency and change the resonance width [148,149]. Hence using high impedance circuits and moderate magnetic fields is recommended [148,150]. Typically, the actuation and the readout is done via a single transducing electrode [151-153]. But this requires a rather complex differential design to extract the small induced electromotive readout current from the strong driving signal background. Reference electrode is usually needed in such configuration. Separation of two signal paths could avoid this problem and lead to simplification of experimental system. This idea was explored using two different chip designs with string resonators fabricated by Peter Larsen during his Ph.D. studies. The low stress SiN strings were 3 µm wide, 500 µm, 320 nm thick with 200 nm thick aluminium (Al) electrodes. The first design called “single electrode” featured one transducing electrode sitting on the string and one reference electrode of the same dimensions. Here the reference electrode signal must be subtracted from the transduction electrode signal. The measurement can be hampered by the resistance mismatch between the two electrodes. In the alternative design called “double electrode” both electrodes were mechanically coupled, transducing electrodes sitting on the string (see Figure 4.12a). One electrode was actuated and generated electromotive force was measured directly from the second electrode. Differences in their resistivity values should be irrelevant. It was first qualitatively confirmed using a damped harmonic oscillator model built in Simulink (see Appendix B). Three resonance responses were obtained of transducing electrode with resistance of 100 Ω for varying second electrode resistances (see Figure 4.12b). The resistance of reference electrode in the “one electrode” chip had evident influence on the resulting output signal. In order to make the two resistances as close to identical as

possible a finely-tunable circuit containing adjustable phase shifter, variable amplifier and directional coupler should be applied [153]. In contrary, the resistance disparity had no consequence for “double electrode” design. The experiments were conducted in high vacuum at a pressure of 1×10^{-5} mbar, magnetic field of 0.4 T and drive voltage of 10 µV resulting in a drive power of 1 pW. Even though the electrodes in both chip types had very similar resistances of 100 Ω themselves, mismatch originated from the other parts of electrical circuits and connections. For example silver conducting paste was used to connect electrodes to wires and was measured to be already about 10 Ω. The resonance frequency response was detected with a lock-in amplifier and proved that resistance matching is crucial to get a good signal to noise ratio (SNR) as values of 37±3 and 207±8 were obtained for “single electrode” and “double electrode” designs, respectively. In addition no capacitive crosstalk has been observed despite the close distance of 6 µm between the two electrodes.

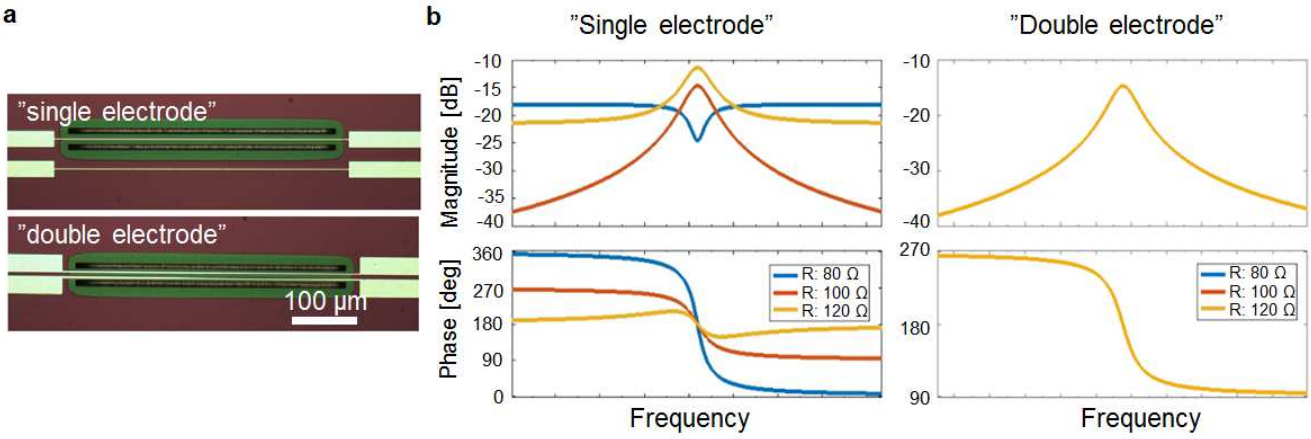

Figure 4.12 a) Microscopic images of the two types of SiN strings with Al electrodes. b) Simulink qualitative simulation results of the two experimental designs. The plots show each three resonance responses of a transducing electrode with resistance of 100 Ω for varying second electrode resistances of 80 Ω, 100 Ω and 120 Ω.

The idea of separated signal paths was harnessed in NAM-IR with perforated membrane resonators. Three Au electrodes were deposited on the membrane, each of them had w width of 10 µm (see Figure 4.13a). A central electrode was used for readout and two electrodes on the sides were used for actuation. The spacing between electrodes and edge of the membrane was 250 µm. The electrodes outside the membrane widened to form 200×200 µm pads in the proximity of the chip edge. A new aluminium vacuum chamber was designed for the purpose of these experiments. It had very compact dimensions of 60×60×50 mm and consisted essentially of two parts held together by screws (see Appendix C). Channels drilled in the aluminium enabled sampling directly in the chamber. The same parabolic mirror as in the previously described setup was used. Also here, the vacuum chamber was attached to a manual linear three axis stage (see Figure 4.13b,c). The chip was glued using epoxy to a custom-made printed circuit board (PCB) with copper contact pads. The electrodes were then either wire-bonded to the contacts on the thermosonic wire bonder (HB05 from TPT, Munich, Germany) or silver paste (Acheson Silver DAG 1415 M from Agar Scientific, Stansted, UK) was used to obtain electrical connection. The PCB with a chip on top was placed between two

Halbach arrays of 3 neodymium magnets that intensify the magnetic field over the membrane chip [154] reaching the value of 0.4 T. Beryllium copper (BeCu) spring loaded contacts (Feinmetall, Herrenberg, Germany) with a preload of 80 cN and nominal force of 130 cN pressed the pads on the PCB providing electrical connection between electrodes on the membrane and lock-in amplifier. They were fixed by cyanoacrylate glue to intermediate part made of poly(methyl methacrylate) (PMMA) that had been milled using computer numeric control (CNC) machine available at DTU Nanotech mechanical workshop. This PMMA part kept the PCB together with sensor chip in the right position using two M3 nylon screws. This approach guaranteed that all units were constrained and spring loaded contacts could always press the contact pads on the PCB allowing for easy replacement of chips and reproducible measurements. The resistance of the Au electrode was calculated to be around 50 Ω but actual values measured through spring contact varied from approximately 450 Ω for wire-bonded chips to 700 Ω for chips connected to PCB by silver paste. In fact, wire bonding required much more expertise and time. Furthermore, contacts created that way were relatively brittle and susceptible to damage. Silver paste turned out to be a good alternative and made experiment preparations easier.

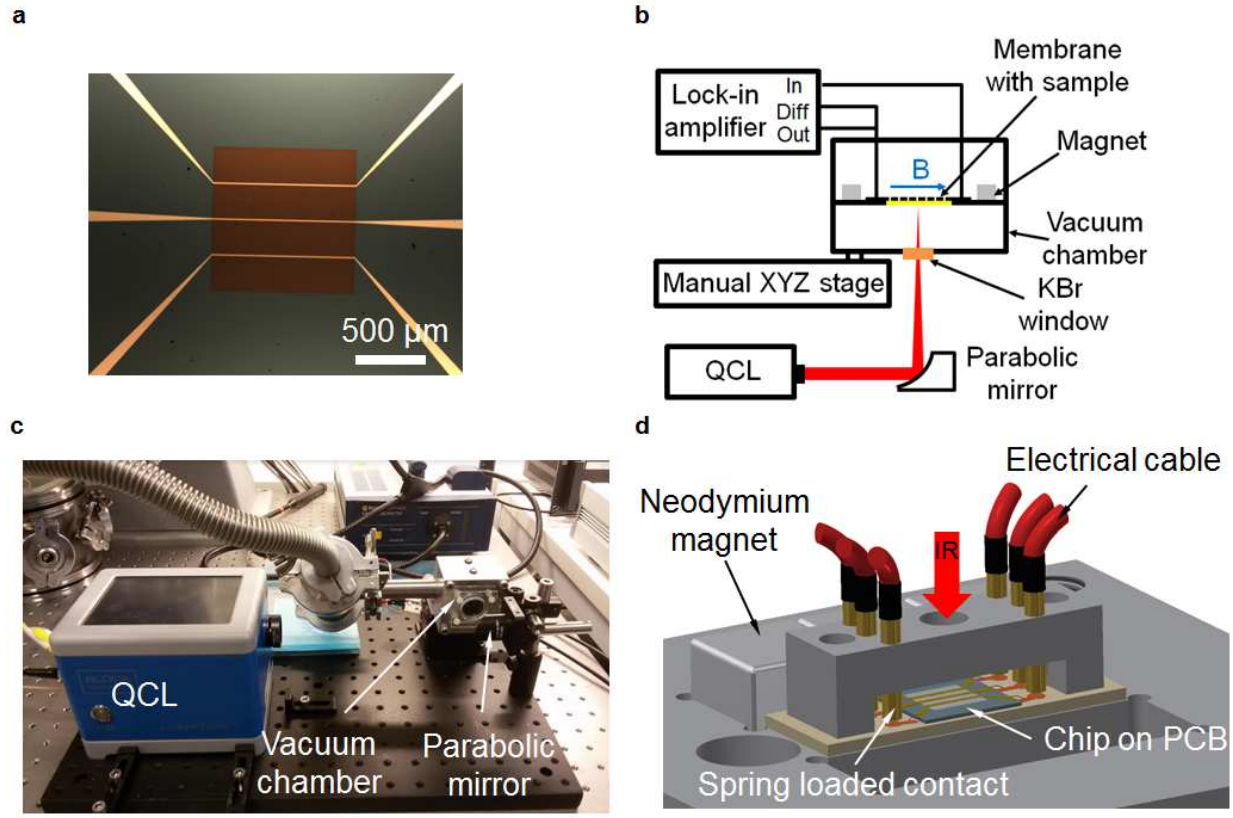

Figure 4.13 a) Microscopic image of the membrane with Au electrodes. b) Schematic and c) picture of experimental setup based on magnetomotive actuation and readout. d) View of the mounting of the chip in the chamber.

The power spectrum of the QCL device was measured with thermal power sensor (S302C from Thorlabs, Newton, NJ, USA) for 0.3% duty cycle with wavenumber step resolution of 10 cm^{-1} and dwell time of 10s. It was found to be strongly wavenumber dependent (see Figure 4.14a). The duty cycle describes the percentage of time a laser is on over a time interval. Measurements showed that QCL irradiation power exhibited polynomial rather than linear growth with increasing duty cycle value.

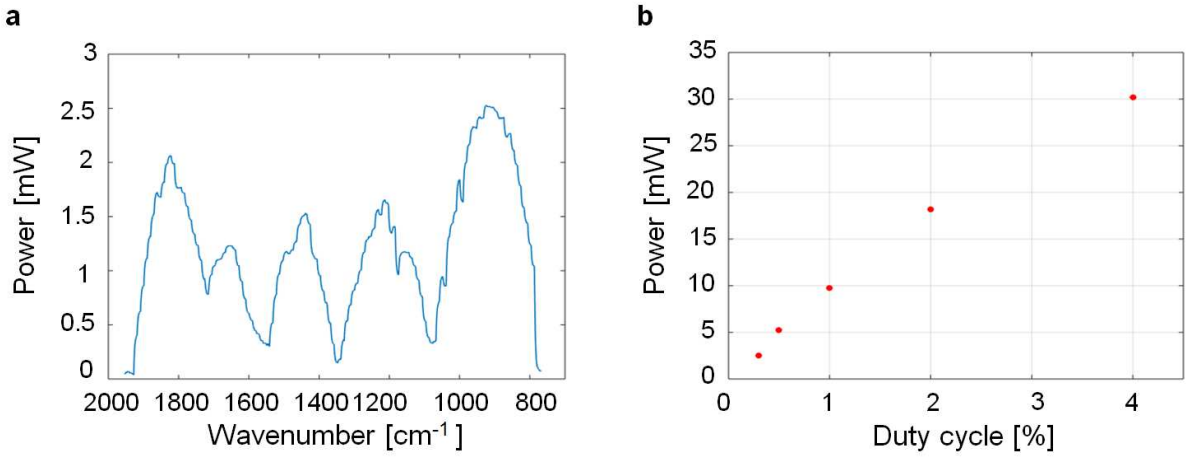

Figure 4.14 a) Power spectrum with 0.3% duty cycle of QCL used in experiments. b) Relation between duty cycle and peak power at wavenumber of 924 cm^{-1}.

4.2.4. Characterization

The knowledge about the properties of fabricated membrane resonators is crucial for further understanding of their behavior as temperature sensors. Simulations were first harnessed to confirm the correctness of the analytical model. Then the experiments were performed to fully characterize structures of interest in terms of mechanical and thermal properties and to reveal the influence of the two different experimental setups.

4.2.4.1. Simulations

Prior to experimental work, finite element method (FEM) simulations were used to validate the analytical model of resonance frequency detuning of a heated membrane. The model was created together with Matthias Carnoy in COMSOL Multiphysics (COMSOL AB, Stockholm, Sweden) software using two modules, namely membranes and heat transfer in thin shells. These modules allow using 2D geometry in 3D environment which makes meshing more effective. Still due to limited computing power, perforation could not be included in the model. The simulation had three study steps. First two stationary steps took into account only heat transfer in the thin shells physics and membrane physics. The last study step was used for eigenfrequency calculations. Simulations were performed for material properties of low stress SiN assuming following values of mass density of 3100 kg/m^3, thermal expansion coefficient of $2.3 \cdot 10^{-6}$ 1/K, Young's modulus of 250 GPa, thermal conductivity of 2.5 W/(m·K), Poisson's ratio of 0.23, heat capacity of 700 J/(kg·K) and tensile stress of 230 MPa [118]. Both square membranes with edge length of 1 mm and circular membranes with radius of 500 μm

were modelled in order to compare their relative resonance frequency changes and determine if analytical model is credible also for square membranes that were actually used in experiments. The fundamental mode resonance frequency values obtained from simulations were 192.62 kHz and 208.51 kHz for square and circular membrane, respectively. It was in very good agreement with values of 192.61 kHz and 209.49 kHz calculated from Equations (2.39) and (2.40). The power input with a step function characteristic and in a form of 200 µm radius circle was placed in the center of both membranes. Initial temperature of a membrane was set at 20°C and edges of the structure were kept at constant temperature of 20°C meaning they were perfectly insulated and there was no heat flux across them. However, these simulation results should be considered more qualitative rather than quantitative as the heat transfer outside the membrane to chip was neglected and actual IR power absorption of SiN was unknown. In addition, perforation could disturb to some extent heat transfer in material increasing its effective surface. Both analytical and FEM models assume that the membrane is in perfect vacuum and convection is fully disregarded. The FEM model confirmed that relative resonance frequency change of square and circular membrane for given conditions were very similar (difference less than 1%) and analytical model can be applied for both membrane shape cases (see Figure 4.15a). As predicted by analytical model the absolute value of relative resonance frequency change was proportional to applied power. The importance of accurate IR laser alignment in the center of the membrane was evaluated as well (see Figure 4.15b). When the IR laser spot is positioned closer to the anchor region more heat would be dissipated into the silicon substrate that acts as a heat sink. For instance misalignment of just 200 µm would result in normalized relative resonance frequency shift drop of around 20%.

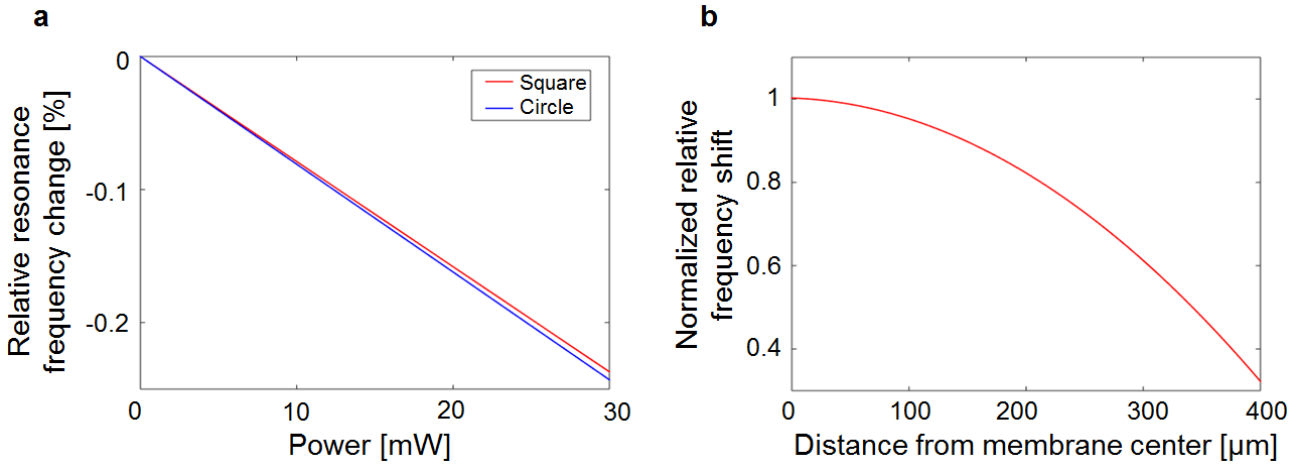

Figure 4.15 a) Simulated relative resonance frequency detuning of square and circular membrane heated in the center of the structure. b) The heat source position on the square membrane has a strong influence on the resonance frequency detuning.

Finally, the membranes lateral dimensions were cut in half but keeping the same heat source to check if that would influence the relative resonance frequency shift. The results showed that a square membrane with edge size of 1 mm had a relative resonance frequency shift roughly 7% higher than a membrane with the edge size of 500 µm. It contradicts the analytical model, which suggests that the

lateral dimensions of the structure should be irrelevant. Surprisingly, experiments later conducted on the unpatterned membranes showed that the smaller membrane had relative resonance frequency shift up to 27% higher than bigger membrane for QCL duty cycle of 0.3% and IR light wavenumber of 870 cm^{-1}. The exact reason for these findings remains unknown but it can be suggested that the influence of the heat transfer from a membrane to a body chip was underestimated as in the analytical model and simulation edge of the membrane was kept at constant temperature. Apparently this further heat transfer should not be neglected and plays bigger role for smaller structures.

4.2.4.2. Membrane properties study

Fabricated membranes were first examined in terms of fundamental mode resonance frequency values. It can be expected that due to temperature, pressure and gas flow fluctuations during deposition in LPCVD furnace, the tensile stress in the SiN layer would vary for different wafers and even for chips across one wafer. Measurements were conducted using experimental setup with laser Doppler vibrometer in high vacuum at a pressure of 1×10^{-5} mbar. Two wafers with membranes of the same dimensions but without perforation were fabricated for comparison purposes. Averaged values of fundamental mode resonance frequency for membranes with edge length of 1×1 mm were measured to be 184.03±1.62 kHz for first and 188.81±0.88 kHz for second wafer. The perforation does not disturb the resonance behavior of a structure and its influence is represented by reduction of tensile stress. Assuming the square perforation holes, the built-in stress σ_p of a perforated plate is in a following relation to tensile stress σ_s of a solid plate of the same dimensions [155]:

$$\sigma_p = \sigma_s \sqrt{1 - 4\frac{a^2}{b^2}}\,, \tag{4.17}$$

where *a* is half of perforation hole length and *b* is a distance between centres of two perforation holes (see Figure 4.16a).

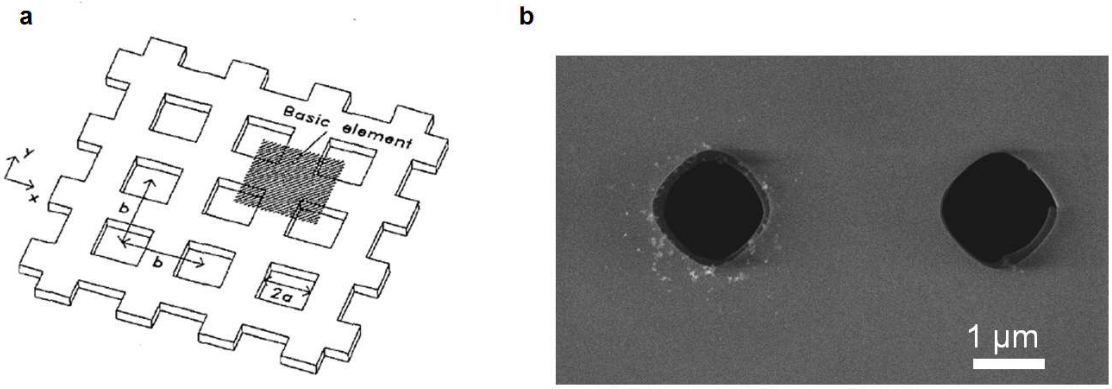

Figure 4.16 a) Schematic of perforated plate with square holes [155]. b) SEM image of a membrane with nominal 2×2 µm holes in 2 µm grid.

This tensile stress reduction should lead to lower resonance frequency values. At the same time perforation causes mass decrease of a structure that can be interpreted as a drop of mass density of a resonator. As it has been already discussed, the actual perforation holes sizes differ from chip to chip

(see Figure 4.16b), hence the resonance frequency of a perforated membrane is difficult to estimate precisely. The measurements of 10 perforated membranes from one wafer with lateral dimensions of 1×1 mm, nominal hole sizes of 2×2 µm in 2 µm grid gave average fundamental mode resonance frequency value of 162.70±4.72 kHz whereas according to Equation (4.17) a value of 171.15 kHz should be expected. Finally, again 10 perforated membranes of the same dimensions as before but with deposited Au electrodes were investigated and an average fundamental mode resonance frequency value of 180.16±5.96 kHz was obtained. Electrodes increased mass of a resonator but resonance frequency went up anyway which suggests that the stiffness of the membranes was altered by metal strips sitting on top of the structure.

The quality factor of membrane resonators is determined by intrinsic and clamping (also called acoustic radiation) losses [67,156-158]. The acoustic mismatch is a coefficient that depends on resonator tensile stress and ratio between mass densities of substrate and resonator material. If its value is high, the tunnelling of phonons from resonator into the substrate is limited. It is also minimal for symmetric modes, when $n=m$. Therefore the maximal Q values of low stress SiN are considered to be restricted by intrinsic losses. For membranes as thin as 100 nm the surface loss dominates the volume loss and is the ultimate ubiquitous limiting damping mechanism in such structures. The origins of the surface loss can be surface impurities or roughness [158]. It could be expected that perforation may contribute to it as well. Membranes with lateral dimensions of 1×1 mm and thickness of 100 nm were used for measurements in the experimental setup with optical detection where Q values were obtained for fundamental symmetric mode with $n=m=1$ from laser Doppler vibrometer software. Membranes without perforation had Q equal to 661±22 and 8168±156 in medium and high vacuum, respectively. Introduction of perforation with nominal hole size of 2 µm in 2 µm grid arose the fall in Q values to 344±25 and 7410±272 for the respective air pressure levels. This decrease has been foreseen as a consequence of higher surface loss but could be related to lower tensile stress and hence smaller damping dilution factor (see Equation 2.43 and 2.46) of perforated membranes as well. At last the membranes with perforation and Au electrodes were studied, yielding Q values of 359±24 and 7772±263 so slightly higher than for perforated membranes without electrodes. Supposedly again the influence of the metal stripes on the structure stiffness became perceptible. On the other hand, experiments conducted in the setup with electromotive actuation and readout showed surprisingly low Q values of 74±7 at 10 mV actuation voltage. The unknown, higher than nominal air pressure level in the chamber can be responsible for it, along with less effective actuation approach than piezo actuator. The lower mode Q values are sensitive to the chip mounting conditions yielding best results when the physical contact between chip and support is minimalized which reduces the radiation losses [67,158]. During experiments the relevance of the tape type clearly appeared as lower values were obtained for simple double-sticky tape than for carbon tape which provided more reliable fixation of the chip (see Figure 4.17). In addition, sampling of an analyte on the membrane surface increased the quality factor of the resonator but the exact reason of this phenomenon is still not fully understood. It can be however assumed that the adsorbed sample did not add to the energy loss and increased the overall energy stored in the system, mainly through potential energy.

The frequency stability of resonator in combination with employed actuation and readout schemes is a crucial property for its performance. Stability in general describes the variation of measurement

samples over time and can be calculated from a set of measurement values. Allan deviation (AD) is a common method of analyzing a sequence of data in the time domain, to measure frequency stability in various types of oscillators. It can be also used to determine the intrinsic noise in a system as a function of the averaging time. AD $\sigma_y(\tau)$ is a square root of Allan variance (AV) which is the variance of

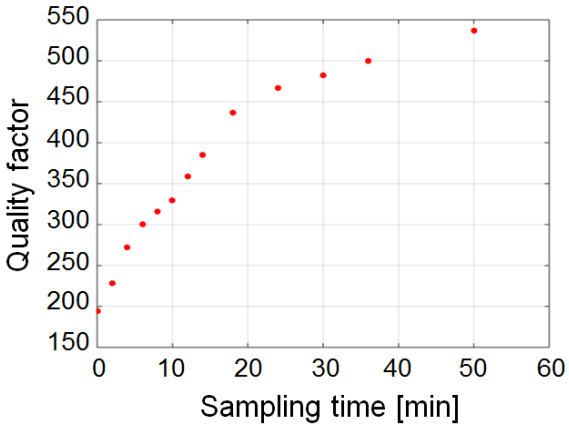

Figure 4.17 Quality factor of a 1×1 mm membrane with nominal 2 µm perforation holes in 2 µm grid changes during sampling of indomethacin. Measurements were done at a pressure of 1 mbar and chip was fixed to the piezo actuator by double-sticky tape.

the difference of two fractional frequency values *y(i+1)* and *y(i)*. The fractional frequency *y(i)* is measured at time $t_0+i\cdot\tau$ and *y(i+1)* at time $t_0+(i+1)\cdot\tau$, respectively. The Allan variance depends on the observation time τ and expresses the mean square of all frequency samples separated in time by τ over the entire measurement interval *T* [159-161]:

$$\sigma_y(\tau) = \sqrt{\frac{1}{2M}\sum_{i=0}^{M-1}\big(y(i+1)-y(i)\big)^2}\ , \tag{4.18}$$

$$M = \frac{T}{\tau} - 1\ , \tag{4.19}$$

$$y(i) = \frac{\langle \nu_1(t_0+i\cdot\tau)\rangle_\tau - \nu_0}{\nu_0}\ , \tag{4.20}$$

where $\langle \nu_1(t)\rangle_\tau$ is the current frequency vibration of the system averaged over a time interval τ and υ_0 is the reference frequency. Simply AV is a variance of M pairs of frequency measurements that were taken at times *t* and $t+\tau$, respectively. It leads to a conclusion that an AD of a value σ_y at observation time τ should be interpreted as there being an instability in frequency between two measurements that are apart of time period τ with a relative root mean square (RMS) value of σ_y. Moreover, a log-log plot of AD over observation time can indicate the two main noise components in the system. For lower observation time values white noise that is proportional to $\tau^{-1/2}$ dominates while for longer averaging times the frequency drift proportional to τ^1 is the limiting factor. The fundamental mode resonance frequency of perforated membrane resonators with side length dimensions of 1×1 mm and nominal perforation hole sizes of 2 µm distributed in 2 µm grid were measured for about 10 minutes in high vacuum using both experimental setups and recorded by lock-in amplifier. Next the AD values were

calculated using MATLAB script written by Luis Guillermo Villanueva (see Appendix D). Exemplary plots obtained by setup with optical readout of continuous resonance frequency measurements and AD over observation time are presented in Figure 4.18.

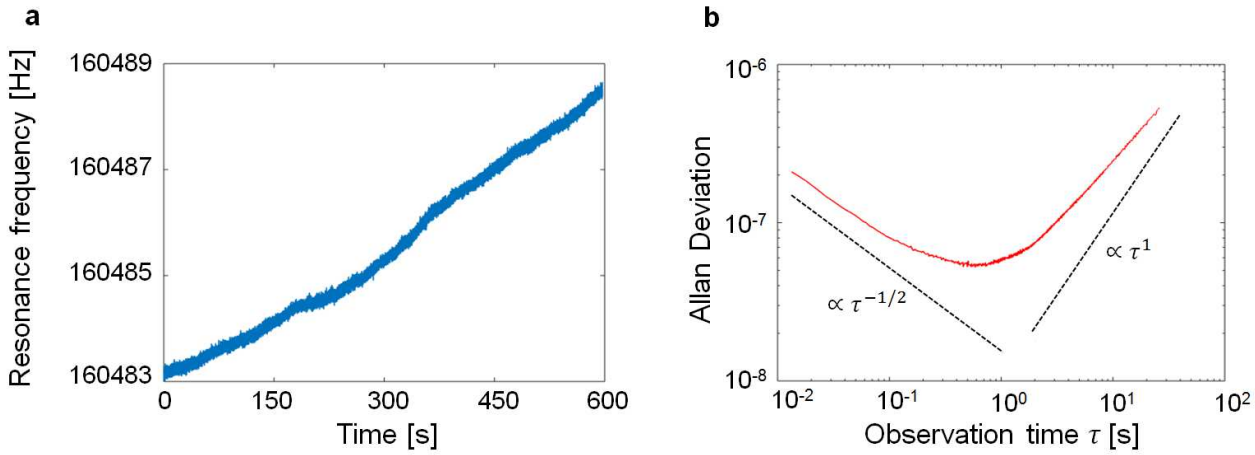

Figure 4.18 a) Continuous measurement of fundamental mode resonance frequency. b) Calculated AD values from data presented in plot a).

The measured resonance frequency was drifting upwards during the entire experiment. It was most likely caused by temperature drift of the resonator [50]. When the vacuum chamber was pumped down the temperature inside dropped due to the Joule-Thompson effect. Then it started to drift towards room temperature as pressure stabilized. In addition, a turbomolecular pump that was situated nearby generated heat that was empowering the temperature change of the membrane. In order to minimalize the effect of readout laser and its varying power, the relatively low power of approximately 4 µW was applied during all measurements [125,162]. Indeed it can be clearly seen that AD is limited by white noise for lower averaging time values and by thermal drift for lower averaging time values reaching a minimum for τ in the range of 1 second. Implementing a temperature control unit could be the first step in improving frequency stability in such system. The thorough characterization of both experimental systems and sensor types demanded a study of influence of IR radiation on the AD value. For this purpose similar measurements were done with IR laser wavenumber set at 870 cm^{-1} where IR light absorption in SiN is the highest and 1176 cm^{-1} where the absorption is low [125,163] (see Figure 4.19). QCL duty cycle was set at the lowest possible level of 0.3% and actuation voltage for membranes with electrodes was set at 2 mV. Measurement results suggested that IR radiation with a wavelength of 1176 cm^{-1} generally did not have a relevant impact on frequency stability. In contrast, for a wavenumber of 870 cm^{-1} the AD value measured by optical readout setup rose approximately 2 orders of magnitude which can be associated with intense heating of a membrane in vacuum conditions. Such phenomenon has not been observed for magnetomotive readout setup. It could be explained by an assumption that the actual air pressure in both chambers was not the same. The chamber of magnetomotive readout setup was connected by long flexible tubing to another chamber, showed in previous chapter, where a pressure sensor was located. Due to possible leakages in the custom-made chamber the pressure inside it can be considerably higher allowing for more effective

heat transfer by convection. The chamber used in optical readout setup had simpler design and much lower volume so even though tubing was needed for connection here as well, the high vacuum pressure could have been reached. Factually, alike measurements performed in optical detection setup at elevated pressure of 1 mbar yielded AD value for 870 cm^{-1} wavenumber IR laser only 23% higher than AD value without IR radiation.

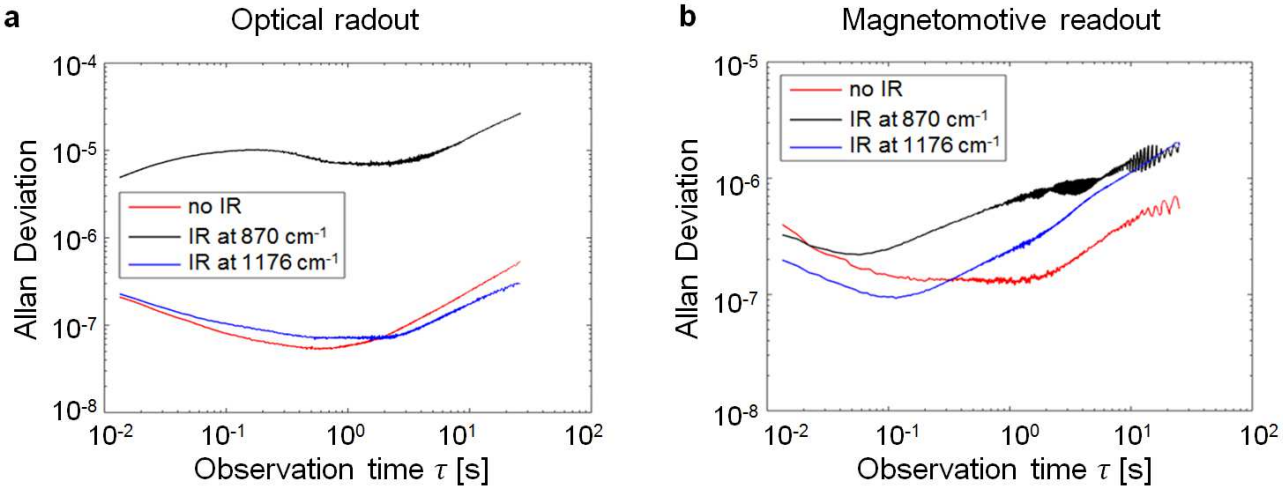

Figure 4.19 AD values obtained for experimental setups with a) optical and b) magnetomotive readout for various IR laser wavenumbers at QCL duty cycle of 0.3%.

In the absence of IR light AD values at observation time of 1 second $\sigma_{opt}(1s)\approx 6.0\cdot 10^{-8}$ and $\sigma_{magn}(1s)\approx 1.3\cdot 10^{-7}$ were obtained for experimental setups with optical and magnetomotive readout, respectively. Higher frequency stability measured for the first setup could be explained by higher vacuum quality achieved in the chamber and less energy loss due to air damping. Apart from that, different readout and actuation approaches might contribute to it, as well as slight design modification of chips needed for magnetomotive actuation and readout. However, the AD value of resonator heated by IR light would be the most important in the context of its applications in NAM-IR technique. The relation between AD and chamber pressure was studied for membrane irradiated with 870 cm^{-1} wavenumber IR light (see Figure 4.20a). The worst AD value at observation time of 1 second $\sigma_{opt}(1s)\approx 5.6\cdot 10^{-6}$ was measured at atmospheric pressure of 1 bar. Decreasing the pressure using only a pre-pump to a level of 1 mbar resulted in AD value $\sigma_{opt}(1s)\approx 6.2\cdot 10^{-7}$. Further pumping with a turbo molecular pump to 1×10^{-5} mbar confirmed previous finding as AD increased to $\sigma_{opt}(1s)\approx 3.9\cdot 10^{-6}$ meaning the frequency stability deteriorated. At the same time SNR of recorded resonance frequency peak improved for lower pressure values from 49 at atmospheric pressure, through 176 at 1 mbar to 551 at 1×10^{-5} mbar. It means that working in high vacuum conditions had an advantage of 3.13 times higher SNR value but also 6.29 times higher AD in comparison to medium vacuum. The benefit of operating in high vacuum is not that unequivocal and the system proved to be capable of working reliably at mbar pressure range. It could allow in future for setup simplification, costs reduction and increased mobility. Similar study has not been conducted for magnetomotive readout setup as resonance frequency peaks could only be recorded for the lowest nominal pressure in the chamber which suggests that magnetomotive actuation and readout schemes were less effective. The actuation

voltage was the only parameter that could be altered here and potentially might change the system performance (see Figure 4.20b).

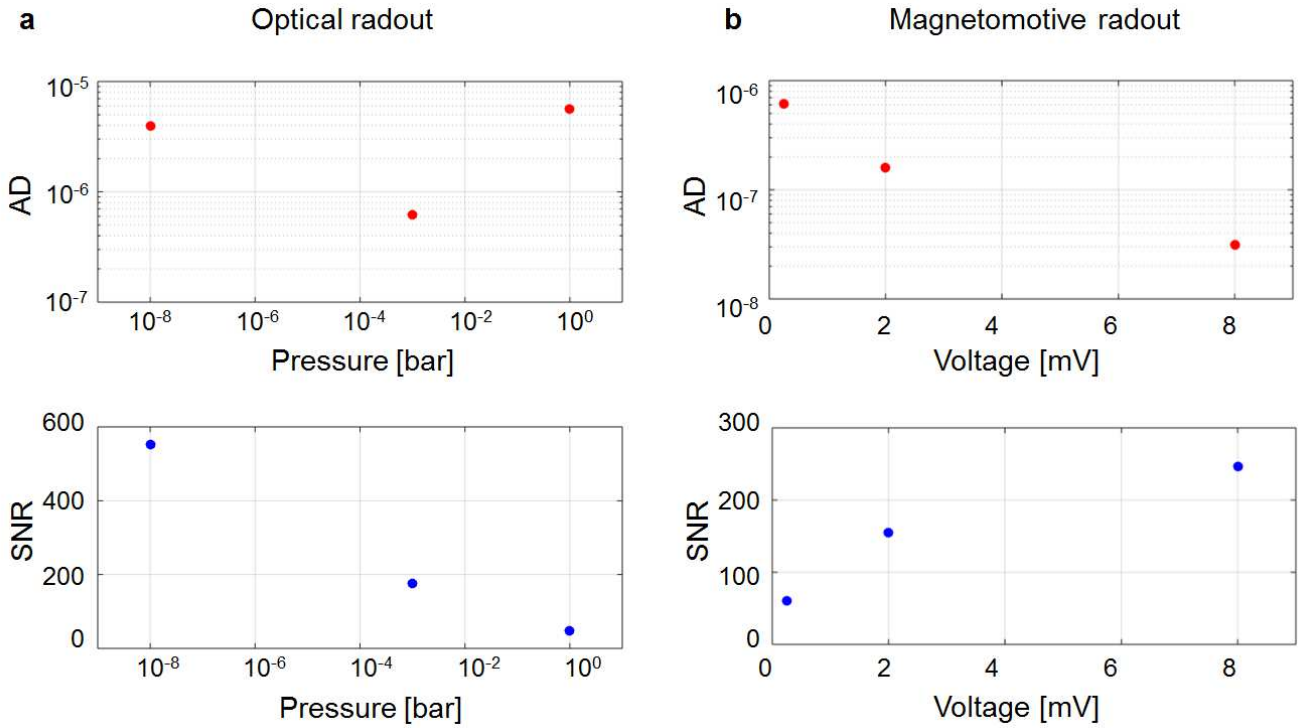

Figure 4.20 AD and SNR of membrane irradiated with IR light with wavenumber of 870 cm^{-1} obtained with a) experimental setup with optical readout for chamber pressure values of 1 bar (atmospheric pressure), 1 mbar (pre-pump only) and 1×10^{-5} mbar (pre-pump and turbomolecular pump) and b) with experimental setup with magnetomotive actuation and readout for actuation voltage values of 0.25, 2 and 8 mV.

According to Equation (4.15) Lorentz force that makes resonator to vibrate is proportional to actuation voltage and inversely proportional to electrodes resistance. Moreover, the electrical equivalent of magnetically-coupled resonator is the parallel combination of a resistor with resistance R_m, an inductor with inductance L_m and a capacitor with capacitance C_m. For an infinite source impedance, the voltage $U(\omega)$ across such circuit as a function of the applied current $I(\omega)$ in frequency domain is [147]:

$$U(\omega) = \frac{j\omega/C_m}{\omega_{LC}^2 - \omega^2 + j\omega/R_m C_m} I(\omega) \,, \tag{4.21}$$

$$\omega_{LC} = \frac{1}{\sqrt{L_m C_m}} \,. \tag{4.22}$$

With the increasing actuation force, AD dropped from $\sigma_{magn}(1s)\approx6.2\cdot10^{-7}$ for actuation voltage of 0.25 mV to $\sigma_{opt}(1s)\approx3.1\cdot10^{-8}$ for actuation voltage of 8 mV. Higher actuation voltage generated more Joule heating on the electrodes which should result in additional temperature drift but apparently this effect was dominated by strengthened actuation. Together with AD enhancement considerable rise of SNR from 61 to 247 was obtained. The relation between SNR and actuation voltage did not show linear

characteristic because of heating of electrodes during measurement that in turn resulted in growth of their resistance value. Polynomial relation was observed instead, as expected from Equation 4.21. At actuation voltage values higher than 8 mV membrane resonators were already in nonlinear regime and hardening behavior could be noticed [164].

The response time is another important feature of a resonator used in fact as a thermal sensor. The ideal thermal detector should have both thermal heat capacity and its coupling to the surroundings as small as possible. In this case, due to nanometer-scale thickness, perforated membranes had an extremely small thermal mass. The supporting silicon chip can be considered as a heat sink. Then the thermal time constant τ_T, which is a measure of how quickly such system responds, can be given by [165]:

$$\tau_T = \frac{H}{G}\,, \tag{4.23}$$

where *H* is the thermal mass and *G* is the thermal conductance. Thermal mass is the ability of a structure to store heat and can be calculated as [166]:

$$H = mc\,, \tag{4.24}$$

where *m* is the mass of a structure and *c* is the heat capacity. Successively, thermal conductance is the ability of a structure to transfer heat, given a temperature gradient through it. It can be divided into three independent parts, namely G_{sup} which is the heat conductance through surface that mechanically supports the membrane, G_{gas} due to surrounding gas and G_{rad} due to radiation. G_{rad} constitutes the low limit of *G* and together with G_{gas} at high vacuum has a negligible value compared with G_{sup}. It can be approximated that a square membrane with a thickness *h*, when heated at the centre, has an overall thermal conductance two times higher than doubly-clamped beam of the same thickness and length as a membrane:

$$G = 8kh\,, \tag{4.25}$$

where *k* is the thermal conductivity. Assuming previously stated values of heat capacity, thermal conductivity and density of SiN, thermal time constant of a 100 nm thick square membrane with 1 mm edge length was estimated from Equation 4.23 to be approximately 109 ms. It is of the same order of magnitude as for other beam, string and membrane thermal sensors reported in literature [125,162,166-168]. The above calculation did not take into account perforation of the membranes which would decrease the thermal mass of a structure and reduce its in-plane thermal conductivity and hence thermal conductance [169-171]. It should be noted that this thermal conductivity reduction is expected to be highly dependent on the perforation geometry. In addition the thermal conductivity of silicon rich SiN varies largely depending on the ratio between silicon and nitride and on the deposition process parameters [125]. The thermal time constant can be also defined as a time required for an increasing system to reach 63.2% of the final value and for a decreasing system a time needed to decay to 36.8% of the initial value. It was experimentally measured for both setups using additionally optical chopper system with 2 slots chopper blade (MC2000B and MC1F2 from Thorlabs, Newton, NJ, USA) placed close to the QCL output. The chopper frequency was set at minimum possible value of 1

Hz with expected resolution of 0.01 Hz so the membrane was irradiated for 500 ms and for the next 500 ms IR light was blocked. Measurements were performed with sampling rate of 1800 S/s which means that time interval between consecutive points was 556 µs. The IR light wavenumber was 870 cm^{-1} and duty cycle was 0.3%. However the frequency of chopper blade rotation was still too high for a chip to reach thermal equilibrium, therefore the IR light was blocked in a longer time spans by manual blade rotation (see Figure 4.21).

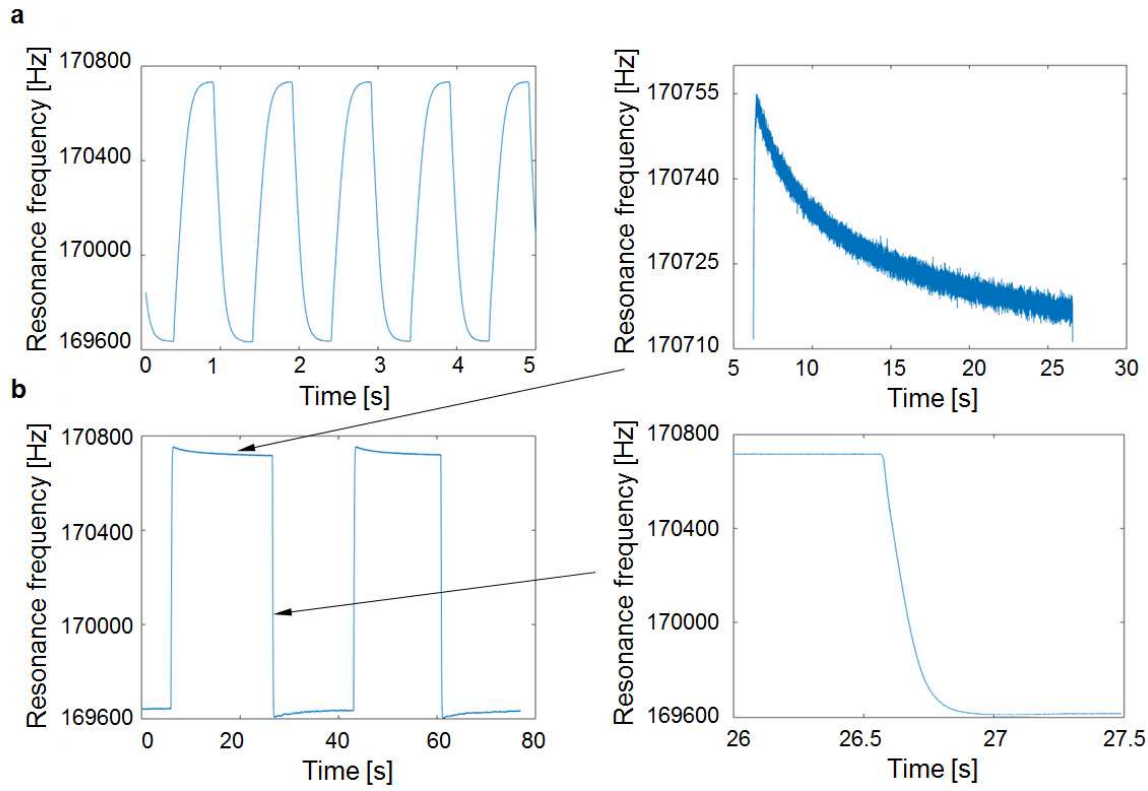

Figure 4.21 Measurements of thermal time constant of 1×1 mm SiN membrane without perforation performed at a pressure of 1 mbar in the experimental setup with optical detection. IR light with wavenumber of 870 cm^{-1} was blocked by a) chopper blade with 2 slots rotating at a frequency of 1 Hz and b) manual rotation of a blade.

Thermal time constant values obtained in the optical readout setup were dependent on pressure in the chamber and chip type. Membrane without perforation and with 1×1 mm lateral dimensions at a pressure of 1×10^{-5} mbar had τ_T equal to 47 ms which was fairly close to theoretical predictions. Experimental data revealed the effect of heating of the silicon chip too. During the resonator exposure to IR radiation heat is gradually transferred from membrane to silicon chip which expands and increases tensile stress of released vibrating structure. When the IR light was blocked the chip cooled down with a τ_{Tchip} of 3.51 s. After the pressure was increased to 1 mbar the more efficient heat convection and conduction through the surrounding air molecules was enabled. The thermal time constant then rose to 93 ms and 5.76 s for membrane and silicon chip, respectively. The perforation indeed affected the thermal conductivity of a membrane as τ_T grew to 126 ms in high vacuum and 243

ms in medium vacuum. Further deposition of indomethacin on the entire membrane surface led to the shortening of thermal time constant to 63 ms in high vacuum and 170 ms in medium vacuum. The drug must have boosted the thermal mass of a system comprised of membrane and sample but simultaneously the thermal conductance was improved as well which was supposed to be a dominating effect. The presence of chemical compounds, especially in the space of perforation holes could have counteracted the thermal conductivity reduction caused by perforation. Finally similar perforated membrane with Au electrodes was investigated, yielding τ_T values of 64 ms in high vacuum and 123 ms in medium vacuum. Au has relatively low heat capacity of 129 J/(kg·K) and thermal conductivity of 310 W/(m·K) [64] which is roughly 100 times more than SiN and presumably contributed to higher thermal conductance value of such structure and eventually to lower thermal time constant. The differences in τ_{Tchip} values for all cases were less than 5%. Regarding the experimental setup with magnetomotive actuation and detection, analogous perforated membrane with indomethacin sample showed significantly higher τ_T value of 495 ms. It can be explained again by higher air pressure in the chamber in comparison to conditions in setup with optical detection. Apart from that, the fact that chip with membrane was attached to the PCB with epoxy could interfere in the heat transfer in the system together with the additional constant heating by electrodes fed with alternating current.

4.3. Results and Discussion

Indomethacin (purity >98% from TCI, Tokyo, Japan), molecular formula $C_{19}H_{16}ClNO_4$, that is a common oral nonsteroidal anti-inflammatory medicine often used as a model drug [172-174] has been chosen for proof of concept experiments. The IR spectra of this drug were recorded and compared with reference FTIR measurements. The smallest amount of sample that can be measured in this method was derived on the basis of obtained data. Indomethacin was studied in both amorphous and crystalline forms and clear differences between respective IR spectra were observed.

4.3.1. IR spectra of indomethacin

Prior to the sampling, the fundamental mode resonance frequency values of blank perforated membranes with lateral dimensions of 1×1 mm and nominal hole sizes of 2 µm in 2 µm grid were measured in two available experimental setups. The membranes with lateral dimensions of 500×500 µm were not used in the experiments due to cumbersome alignment of IR laser spot in their centre, especially for magnetomotive detection setup. The membrane used in optical detection setup had the resonance frequency of 127332 Hz and value obtained for the membrane used in magnetomotive scheme setup was 181525 Hz. Relatively big difference between these numbers may be associated with a fact that the membranes were fabricated in two different batches. On the basis of Equation 2.39 it was calculated that tensile stress values were 101 MPa and 228 MPa for membranes used in optical detection and magnetomotive scheme, respectively. The crystalline indomethacin was dispersed in methanol in concentration of 0.5 mg/ml. The air pressure from filtered air supply was kept at 0.5 bar and air flow in the system was 1 l/min. The sample was nebulized for 3 min and the average particle radius was 25 nm. The resonance frequency was measured again after deposition and due to additional structure mass values felt to 104186 Hz in optical detection setup and 152307 Hz in

magnetomotive scheme setup. The knowledge about the resonance frequency values could be first used to derive the aggregate mass of a resonator with sample and finally the mass of the sample only. The mass of perforated membrane used in the experiment was 252±5 pg and mass of similar membrane with electrodes was 281±6 pg. From resonance frequency data the mass of membrane with sample was computed to be 376±8 pg and 400±8 pg for respective setups. Hence, 124±9 pg of indomethacin was sampled on the membrane in the optical detection setup and 119±10 pg in the magnetomotive detection setup.

Laser pointer embedded in the QCL allowed for convenient IR laser spot alignment in the center of the membrane (see Figure 4.22a).

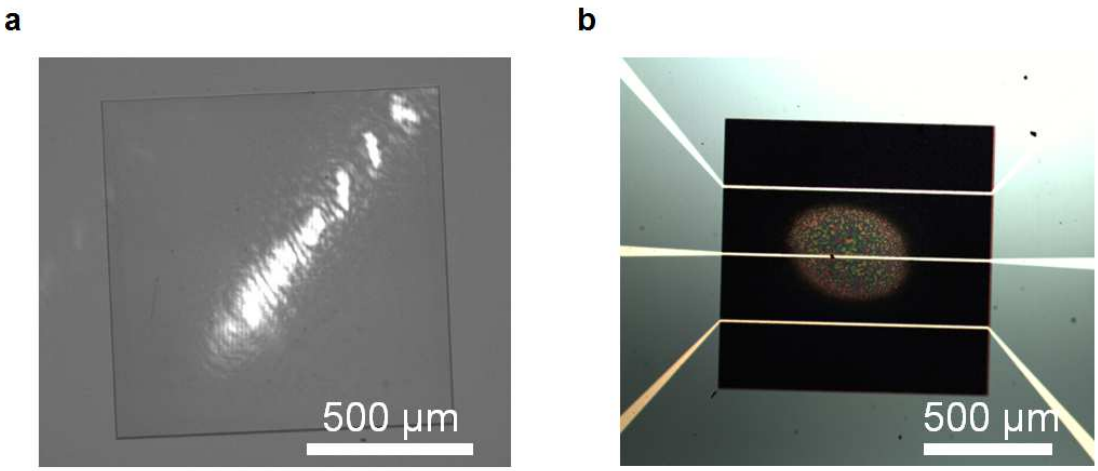

Figure 4.22 Microscopic images of a) IR beam position being aligned with the help of laser pointer and b) melted indomethacin in the spot where IR laser was focused.

The laser duty cycle was set at 0.3% with pulse duration of 30 ns and repetition rate of 100 kHz. The highest radiation power peak achieved for these settings was 0.25 mW. The lowest possible duty cycle level has been chosen because for higher duty cycle values melting of the sample was observed suggesting that the melting point of indomethacin which is around 162°C for stable crystalline form [175,176] could be reached locally in both setups (see Figure 4.22b). From the picture above the IR laser spot size can be estimated to be approximately 400 µm in diameter. The QCL was operated in a sweep mode in the full wavenumber range from 768 cm^{-1} to 1953 cm^{-1} with a spectral linewidth of 2 cm^{-1} [144]. The sweep took 100 s which means that the sweeping speed was 0.012 cm^{-1}/ms. The maximum resonance frequency shift could be obtained when the membrane with sample would be irradiated for time duration equal to or higher than its thermal time constant [177]. The average irradiation time for a single cm^{-1} was calculated to be approximately 80 ms which was more than thermal time constant of a perforated membrane with indomethacin measured in the optical detection setup ensuring the steady state thermomechanical response but much less than value derived for magnetomotive detection setup.

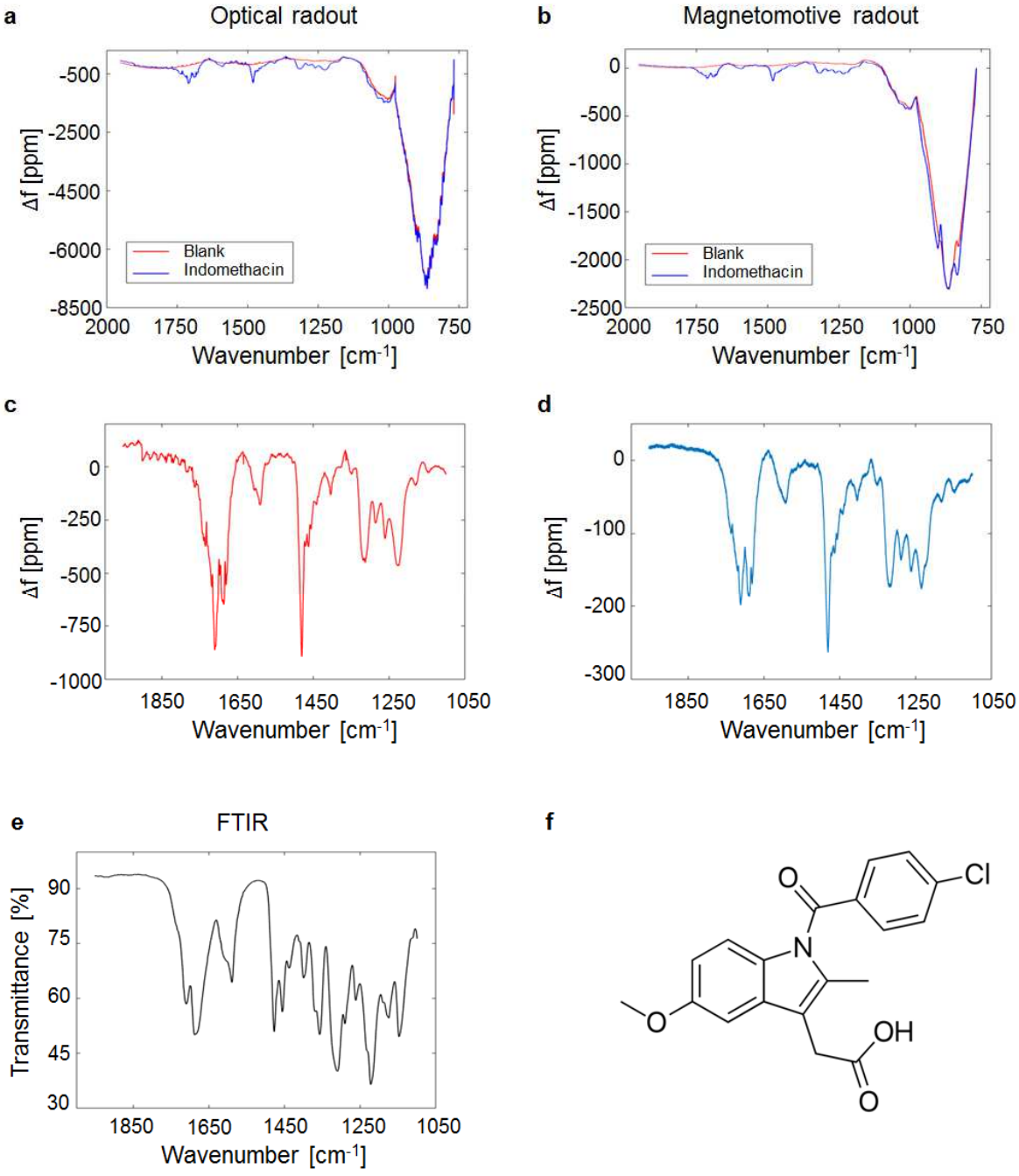

Figure 4.23 IR spectra of blank SiN membrane and membrane with crystalline indomethacin recorded in setup with a) optical and b) magnetomotive detection scheme. The peaks at 870 cm^{-1} and 1016 cm^{-1} are related to SiN. Plots c) and d) show IR spectra of indomethacin for respective setups and were obtained through subtraction of data gathered for membrane with indomethacin and blank membrane. e) The reference transmission IR spectrum of amorphous indomethacin measured by FTIR method. f) Skeletal formula of indomethacin.

Initially, the spectrum of a blank membrane was measured in high vacuum, then the same resonator with indomethacin was analyzed (see Figure 4.23a,b). The spectra of sensor with indomethacin were normalized to the spectra of blank resonator, particularly because of the inability to focus the IR laser exactly on the same spot of the membrane for each experiment. The resonance frequency temperature drift was corrected as well. Subtraction of these two data sets was necessary to remove the background signal from the final indomethacin IR spectrum that arose mainly from the stretching vibrations of Si-N bonds at 870 cm^{-1} and 1016 cm^{-1} [178,179] and fluctuations caused by the wavenumber dependent power spectrum of the QCL (see Figure 4.23c,d). The wavenumbers dominated by SiN peaks were not included in the last two mentioned plots that had a wavenumber range from 1100 cm^{-1} to 1953 cm^{-1}. The reference IR spectrum was obtained using conventional FTIR spectrum analyzer (Spectrum 100T from PerkinElmer, Waltham, MA, USA) based on ATR technique. Both NAM-IR spectra were in good agreement with the FTIR reference. The major peaks measured at 1316, 1481, 1591, 1688 and 1709 cm^{-1} using the setup with optical readout and at 1318, 1481, 1594, 1690 and 1712 cm^{-1} using the setup with magnetic transduction corresponded closely to the reference that showed peaks at 1311, 1478, 1590, 1686 and 1711 cm^{-1} and to literature data [180-182].

For instance, the last two peaks located in the ketone C═O stretching region can be attributed to benzoyl and acid group vibrations [183]. The absolute resonance frequency shift values measured for the last of mentioned absorption peak were 91 Hz and 31 Hz which equals to relative frequency shifts of 864 ppm and 197 ppm for optical and magnetic readout setups, respectively. This response of nanomechanical resonators to temperature change can be analyzed in terms of responsivity and sensitivity.

Responsivity can be defined as a change of a resonance frequency as a function of a specific parameter [22] which in this case was power absorbed by the sample and transferred to the membrane. The sample mass irradiated with IR light was almost the same for two different experimental setups and could not be the reason for the lower responsivity to temperature of the sensor operating in the magnetic scheme. The explanation could take into account factors that had been discussed before. First of all, the supposedly higher pressure in the chamber might have made enabled the heat transfer by convection in the system. It was also assumed to increase thermal time constant of a resonator in such system. Secondly, the influence of Au electrodes could not be neglected. As it has already been mentioned, Au has roughly 100 times higher thermal conductivity than SiN, increasing the heat flow from the membrane to the substrate. According to Equation 2.72 it should result in lowered responsivity of the sensor. However, Au also has about 6 times higher thermal expansion coefficient [64] which partly counteracts the negative effect of its large thermal conductivity. Apart from that tensile stress values of the two membranes used in experiments were different as the membrane from magnetomotive detection setup had more than 2 times higher stress than the one from optical detection setup. Finally, the possible not perfect alignment of the IR laser beam in the center of each membrane could also contribute to obtained unlike responsivity levels. On the basis of Equation 2.72 it was calculated that the measured frequency shifts were the results of 572±6 nW and 296±2 nW of absorbed power in the membranes used in optical and magnetomotive detection setups, respectively. It means that relative responsivity values of 1.51 ppm/nW and 0.67 ppm/nW were obtained for the two investigated cases.

Next, sensitivity is the smallest detectable change of the input signal with a specified value of SNR [22]. In terms of possible application of NAM-IR for example in pharmaceutical industry, the figure of merit would be the smallest amount of sample that can be reliably analyzed. SNR was extracted for a peak at a wavelength of 1709 cm^{-1} for optical and 1712 cm^{-1} for magnetomotive detection setup. The standard deviation of the fundamental mode resonance frequency was derived from the data collected when the QCL was off. The SNR was then 421 for the optical and 408 for the magnetic setup. The 3-sigma sensitivity was obtained by dividing the total collected sample mass by SNR and multiplying by a factor of 3, which gave values of 0.91 pg and 0.87 pg for the consecutive experimental approaches. However, the IR spot had a radius of about 200 µm and covered just 12.5% of the overall membrane area. Considering only the actually probed sample it means that as little as 111±15 fg and 109±15 fg was sufficient to give a significant signal for a respective experimental setup.

4.3.2. Crystallization study

The study of crystallization of indomethacin was used as an example of high utility of developed perforated membrane sensors for NAM-IR in pharmaceutical industry where a proper identification of drug crystallinity is crucial because the degree of crystallinity can severely impact the chemical properties and pharmaceutical performance of a compound [184]. Drugs in the amorphous state have a higher aqueous solubility and dissolution rate compared to their crystalline counterparts [185]. This can result in a higher oral bioavailability of the amorphous drug. The disadvantage of the amorphous form of a drug is that it tends to be less stable, more susceptible to air oxidation, adsorption of excipients and blending effects as well as less reproducible in production in comparison to the crystalline form [186]. Therefore, whilst there is a great interest in using drugs, for instance for oral administration, in their amorphous form, the solid amorphous form of the drug needs to be evaluated during storage, production and dissolution as it is prone to convert to a metastable or stable crystalline form. Characterization of the drug form can be done by various techniques, including usually differential scanning calorimetry (DSC), X-ray powder diffraction (XRPD), polarized light microscopy (PLM) or Raman and IR spectroscopy but these methods can be labor and time intensive [185,187-189]. As NAM-IR with perforated membrane resonators is capable of sampling and analyzing compounds in powder and in dispersion without any tedious pretreatment it could be a promising alternative to techniques mentioned before. To prove it, indomethacin was studied in two different forms: amorphous and crystalline (see Figure 4.24). The compound has been purchased in the crystalline form and dispersing it in the methanol ensured obtaining after nebulizing dry sample in the amorphous form. In order to perform reference FTIR measurements amorphous indomethacin powder was prepared by melting the initial crystalline powder in an aluminium pan on a heating plate at 180°C for 2 min. The melt was then immediately cooled by the use of liquid nitrogen followed by lightly grounding the amorphous drug with a mortar and pestle. The nebulizer could not be used for sampling crystalline indomethacin so several mg of powder was placed in a beaker and directly sucked through tubing to the sampling chamber with perforated membrane maintaining air flow rate of 1 l/min. This approach could not be as well controlled as sampling by nebulizer and therefore approximately 3.6 times more amorphous than crystalline sample was collected on the 1×1 mm membranes. The measurements were conducted in the optical detection setup in the medium vacuum.

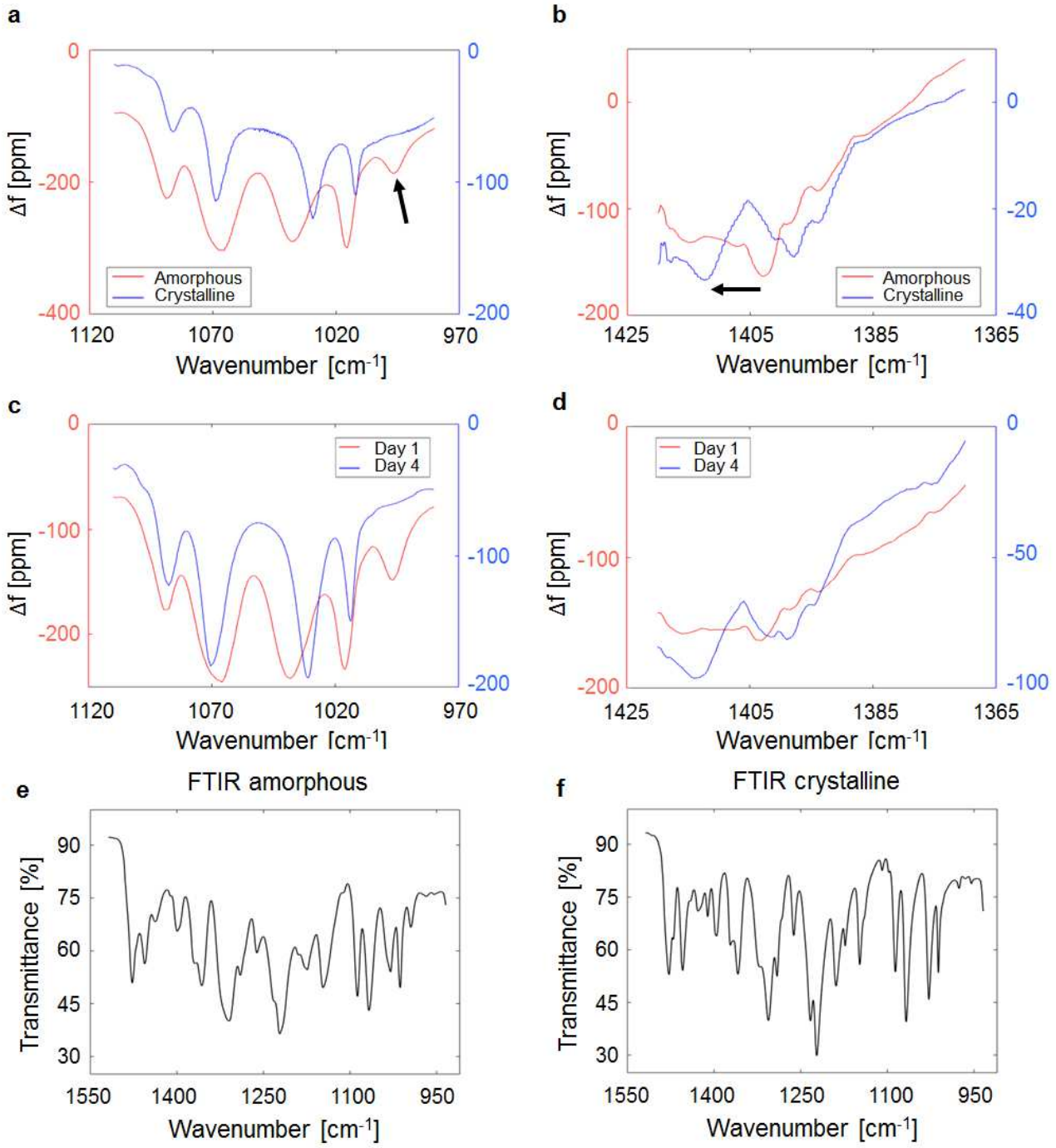

Figure 4.24 IR spectra of membrane with amorphous and crystalline indomethacin recorded in setup with optical detection scheme in medium vacuum. a) The disappearance of a peak at 996 cm^{-1} and b) peak shift from 1403 cm^{-1} to 1413 cm^{-1} could be observed. Plots c) and d) show similar spectra changes which were the effects of crystallization of the amorphous sample. Spectra obtained by NAM-IR were in good agreement with reference relative spectra e) and f).

The ability of performing relevant experiments without a need of high vacuum conditions makes the NAM-IR more important for future applications in industry or research. As IR spectroscopy is a vibrational technique the spectrum contains information on both the chemical and physical state. The overall spectrum of crystalline material would have sharper peaks than the spectrum of amorphous material mainly because it has much more ordered structure. Moreover, it is expected that IR spectra of a specific compound in amorphous and crystalline form would have shifted and disappeared peaks [190-193]. It can be explained i.e. by forming of hydrogen bonds between molecules during crystallization [194]. Primitively, the spectra of both drug forms were measured on the FTIR instrument to define possible changes between them. Then the wavenumber regions of 980-1110 cm^{-1} and 1370-1420 cm^{-1} have been selected to focus on the most distinct differences observed before. Indeed clear dissimilarities in spectra recorded by NAM-IR of amorphous and crystalline indomethacin could be recognized (see Figure 4.24a,b). The peaks of amorphous indomethacin at 1015, 1038, 1066 and 1089 cm^{-1} shifted for crystalline form to 1012, 1030, 1069 and 1086 cm^{-1}, respectively. There was a peak at 996 cm^{-1} present for the amorphous form but disappeared for the crystalline form. The second investigated wavenumber region showed the peak shift from 1403 cm^{-1} for amorphous to 1413 cm^{-1} for crystalline compound. The crystallization study provided very similar results (see Figure 4.24c,d). Amorphous indomethacin was nebulized on the membrane and NAM-IR experiment was done right afterwards. Then the chip with sample was left for 4 days at a temperature of 22°C and relative humidity of 48%, the storage conditions were measured using temperature and humidity probe (KTH from Supco, Allenwood, NJ, USA). Indomethacin captured on the sensor surface crystallized during this time which was confirmed by the new measurement. The peak at 996 cm^{-1} vanished and remaining peaks experienced analogical shifts as reported before. All of these results were in accord with literature [195] and reference FTIR data (see Figure 4.24e,f) and proved that NAM-IR is capable of finding the distinction between various form of chemical substances.

4.4. Conclusion

Micromechanical perforated SiN membrane resonators were successfully used as thermal sensors for photothermal IR spectroscopy contributing to the advancement of NAM-IR technique that has great potential for further improvement.

The fabrication of required structures was based on the conventional cleanroom techniques including photolitography, wet and dry etching and metal deposition. The achieved fabrication yield was about 90% but mainly due to the not uniform UV light intensity across the wafer perforation holes shape would differ for various chips. In addition, the smallest holes with lateral edge size of 1 µm were not always precisely defined because of the resolution limit of the mask aligner.

A crucial advantage of the NAM-IR is simple and efficient analyte sampling through impaction on the surface of the perforated membranes that acts as porous filters. It was accomplished by a simple setup using a jet nebulizer. The analyte was first dispersed in liquid and nebulized to create airborne nanoparticles that were later filtered by a resonator in a dedicated chamber. Such approach allowed reaching a theoretical sampling efficiency of 59±21%, a substantial progress in comparison to

sampling abilities of single filter-fiber string resonators with a total sampling efficiency on the order of 10% [115].

Measurements of roughly 100 pg sample of drug indomethacin were conducted using two different experimental setups. First one relied on optical readout with laser Doppler vibrometer and piezo ring actuation, whereas the second one was fully based on magnetomotive readout and actuation and required chips with electrodes. The influence of perforation and electrodes on the membranes mechanical and thermal properties was investigated. Analysis of obtained data showed that the performance of the magnetic transduction scheme was comparable to the traditionally used optical readout systems. Bearing in mind that the IR laser spot covered only about 12.5% of the membrane surface, the minimum mass required for study is only 109±15 fg. It is of the same order of magnitude as the detection limit reported for NAM-IR done with silicon nitride string resonators [17,125]. It should be noticed that all of the obtained IR spectra, both for amorphous and crystalline indomethacin were in good agreement with FTIR reference plots.

Chapter 5

Conclusion and Outlook

My research in the Nanoprobes group at DTU Nanotech was focused on nanomechanical resonators. It was a highly experimental work oriented towards advancement of a certain type of NEMS. The main goal of this Ph.D. project was to develop integrated devices for NAM-IR and it was successfully accomplished.

However, another work had been realized prior to that. It was dedicated to nanomechanical pyrolytic carbon resonators. Novel fabrication approach has been used which allowed for obtaining cantilevers and strings. The fabrication process was relatively simple and consisted of three basic steps: photolithography, dry etching and pyrolysis. Two combinations of the process with different step order were investigated and it turned out that each of them can provide different type of resonator. Measurements of the fundamental mode resonance frequency were then utilized for characterization of vibrating structures. Data obtained from cantilevers enabled calculation of Young's modulus which was 74±8 GPa for negative and 115±8 GPa for positive photoresist precursor. On the other hand, resonance frequency values of strings led to derivation of tensile stress of 33±7 MPa for positive photoresist only, as fabrication of strings through pyrolysis of negative photoresist was not feasible. Presented mechanical properties and known electrical conductivity of pyrolytic carbon suggest that after better understanding the nature of pyrolysis and optimization of fabrication process, pyrolytic carbon resonators can become a real alternative to common materials used now for resonators.

As it has already been mentioned, the core of my project was related to NAM-IR, the technique with extremely high sensitivity that needs only minute amount of sample and requires nearly no analyte preparation, reducing expenses and saving time. In fact, this kind of photothermal IR spectroscopy approach was demonstrated for the first time by Shoko Yamada, former Ph.D. student in the Nanoprobes group. On the basis of her results and comments, the possible improvements of the method were identified. It was the starting point for my engagement in this field.

The initial NAM-IR system relied on silicon rich SiN string resonators with a width below 1 µm. It offered detection limit of several tens of fg but alignment of the IR laser beam to the vibrating structure was difficult and inefficient. Moreover, the experimental setup was based on the optical radout with laser Doppler vibrometer, a precise but bulky and expensive instrument.

Replacing string with membrane resonators appeared as a natural solution to these issues. In order to maintain the advantage of analyte sampling through impaction on the resonator surface, the membranes had microscale perforation. In addition, membranes facilitated introduction of magnetomotive readout and actuation scheme. Several non-intersecting electrodes were deposited on single membrane which helped to avoid a complex differential signal extraction setup.

Indeed, perforated membranes showed even higher overall sampling efficiency than string resonators. The principal difference here was that string could be considered single filter-fiber, whereas perforated membrane acted as porous membrane filter. Sampling has been carried out with rather uncomplicated setup in which airborne sample nanoparticles were created by jet nebulizer. It was exactly the same setup as used before during sampling attempts with strings.

The actual NAM-IR experiments were preceded by theoretical analysis and characterization of membranes. The model of the heat transfer in the circular membrane and its influence on the fundamental mode resonance frequency was developed. Qualitative FEM simulations confirmed the veracity of the analytical predictions. Then experiments were conducted to gain knowledge about such features of resonators as tensile stress, frequency stability and thermal time constant. It was also vital to understand the impact of perforation and electrodes on the resonators behavior. Furthermore, a newly designed setup based on the magnetic transduction was employed and the importance of such factors like actuation voltage and chamber air pressure must have been investigated. It was eventually concluded that the performance of optical and magnetomotive detection setups was closely comparable.

The proof of concept experiments were done on the indomethacin which is commonly used as a model drug. It was easily nebulized from dispersion in methanol and sampled on the sensor. The NAM-IR study of roughly 100 pg of sample provided IR spectra of the compound. Several absorption peaks were recorded and they were in good agreement both between different experimental setups and FTIR reference. It was proved that indomethacin in amorphous and crystalline form can be distinguished using this technique as well. Through analysis of the obtained data the minimal sample mass required for analysis was determined to be 109±15 fg. The sensitivity of the same order of magnitude was achieved with string resonators.

Even though optimization of the chip fabrication process and setup design improvements should be done, the results of this research on new approach to NAM-IR suggest that it is a technique with vast possible applications. It could be attractive especially for pharmaceutical industry where product quality has highest priority. One can imagine an integrated NAM-IR device placed by the ventilation system in laboratory or production facility and constantly filtering air. In defined period of time the sampling chamber would be pumped down and used for performing measurements. For instance if any undesirable compound would be identified, the system could set a warning. Such on-line monitoring system should be of course easy to handle and free of technical failures. Unfortunately, membranes after sample deposition cannot be cleaned and reused which means they should be fabricated for a reasonable price.

Another relevant study that could be done using existing setup is to determine if given compound is in the hydrate or non-hydrate form [196,197]. Similarly as in the case of amorphous and crystalline forms, these two forms would have different solubility and stability and it needs to be strictly controlled on the each step of production process. Next, compound with a melting point at much higher temperature than indomethacin could be chosen to enable experiments with greater QCL power. It would be interesting to see if single molecule measurement would be possible with NAM-IR.

Modifications to setups described in this thesis could also be envisioned. Particularly, the possibility of controlling temperature of a sample inside the chamber would be appealing. It should be feasible to add to the system if a temperature control unit based on Peltier module would be developed [162]. It offers a wide range of temperatures and is capable of both cooling and heating. Standard Peltier element could be fitted without difficulty in the vacuum chamber and then controlled for example through LabVIEW program. The temperature-dependent measurements of IR spectra could provide information about mechanism of polymorphic transition of various chemical compounds and follow their rapid changes in the crystalline forms and could to some extent replace DSC technique [198,199]. Apart from that, such new feature would give access to drug degradation [200] and thermodynamics [201,202] studies that are crucial for new drug discovery. I believe that these concepts could be carried on in future by members of the Nanoprobes group.

Chapter 6

Bibliography

[1] R. P. Feynman. There's plenty of room at the bottom. *Engineering and Science* **23**, 22-36, 1960.

[2] A. Hullmann, and M. Meyer. Publications and patents in nanotechnology. An overview of previous studies and the state of the art. *Scientometrics* **58**, 507-527, 2003.

[3] J. Weiss, P. Takhistov, and D. J. McClements. Functional materials in food nanotechnology. *J. Food Sci.* **71**, 107-116, 2006.

[4] W. Zhu, P. J. M. Bartos, and A. Porro. Application of nanotechnology in construction. Summary of a state-of-the-art report. *Mater. Struct.* **37**, 649-658, 2004.

[5] A. P. S. Sawhney, B. Condon, K. V. Singh, S. S. Pang, and G. Li. Modern applications of nanotechnology in textiles. *Text. Res. J.* **78**, 731-739, 2008.

[6] M. Singh, S. Singh, S. Prasad, and I. S. Gambhir. Nanotechnology in medicine and antibacterial effect of silver nanoparticles. *Dig. J. Nanomater. Biostruct.* **3**, 115-122, 2008.

[7] J. M. Garcés, D. J. Moll, J. Bicerano, R. Fibiger, and D. G. McLeod. Polymeric nanocomposites for automotive applications. *Adv. Mater.* **12**, 1835-1839, 2000.

[8] A. Boisen, S. Dohn, S. S. Keller, S. Schmid, and M. Tenje. Cantilever-like micromechanical sensors. *Rep. Prog. Phys.* **74**, 036101, 2011.

[9] J. Chaste, A. Eichler, J. Moser, G. Ceballos, R. Rurali, and A. Bachtold. A nanomechanical mass sensor with yoctogram resolution. *Nat. Nanotechnol.* **7**, 301-304, 2012.

[10] J. Moser, J. Güttinger, A. Eichler, M. J. Esplandiu, D. E. Liu, M. I. Dykman, and A. Bachtold. Ultrasensitive force detection with a nanotube mechanical resonator. *Nat. Nanotechnol.* **8**, 493-496, 2013.

[11] T. Larsen, S. Schmid, L. Grönberg, A. O. Niskanen, J. Hassel, S. Dohn, and A. Boisen. Ultrasensitive string-based temperature sensors. *Appl. Phys. Lett.* **98**, 121901, 2011.

[12] T. Larsen, S. Schmid, L. G. Villanueva, and A. Boisen. Photothermal analysis of individual nanoparticulate samples using micromechanical resonators. *ACS Nano* **7**, 6188-6193, 2013.

[13] S. Bose, S. Schmid, T. Larsen, S. S. Keller, P. Sommer-Larsen, A. Boisen, and K. Almdal. Micromechanical string resonators: analytical tool for thermal characterization of polymers. *ACS Macro Lett.* **3**, 55-58, 2014.

[14] G. H. Brilmyer, A. Fujishima, K. S. V. Santhanam, and A. J. Bard. Photothermal spectroscopy. *Anal. Chem.* **49**, 2057-2062, 1977.

[15] J. R. Barnes, R. J. Stephenson, C. N. Woodburn, S. J. O'Shea, and M. E. Welland. A femtojule calorimeter using micromechanical sensors. *Rev. Sci. Instrum.* **65**, 3793, 1994.

[16] S. Kim, D. Lee, and T. Thundat. Photothermal cantilever deflection spectroscopy. *EPJ. Tech. Instrum.* **1**, 7, 2014.

[17] S. Yamada, S. Schmid, T. Larsen, O. Hansen, and A. Boisen. Photothermal infrared spectroscopy of airborne samples with mechanical string resonaotrs. *Anal. Chem.* **85**, 10531-10535, 2013.

[18] A. N. Cleland, and M. L. Roukes. Fabrication of high frequency nanometer scale mechanical resonators from bulk Si crystals. *Appl. Phys. Lett.* **69**, 2653, 1996.

[19] D.-K. Bučar, R. W. Lancaster, and J. Bernstein. Disappearing polymorphs revisited. *Angew. Chem. Int. Ed.* **54**, 6972-6993, 2015.

[20] A. A. Gowen, C. P. O'Donnell, P. J. Cullen, and S. E. J. Bell. Recent applications of chemical imaging to pharmaceutical process monitoring and quality control. *Eur. J. Pharm. Biopharm.* **69**, 10-22, 2008.

[21] S. G. Kelly. *Fundamentals of mechanical vibrations.* McGraw-Hill, Inc., 1993.

[22] S. Schmid, L. G. Villanueva, and M. L. Roukes. *Fundamentals of nanomechanical resonators*. Springer, 2016.

[23] A. N. Cleland. *Foundations of nanomechanics*. Springer, 2003.

[24] S. P. Timoshenko, and S Woinowsky-Krieger. *Theory of plates and shells*. McGraw-Hill, 1959.

[25] O. A. Bauchau, and J. I. Craig, *Structural analysis*. Springer, 2009.

[26] F. Ebrahimi. *Advances in vibration analysis research*. InTech, 2011.

[27] A. E. H. Love. *A treatise of the mathematical theory of elasticity.* Cambridge University Press, 1906.

[28] S. S. Verbridge, J. M. Parpia, R. B. Reichenbach, L. M. Bellan, and H. G. Craighead. High quality factor resonance at room temperature with nanostrings under high tensile stress. *J. Appl. Phys.* **99**, 124304, 2006.

[29] B. M. Zwickl, W. E. Shanks, A. M. Jayich, C. Yang, A. C. Bleszynski Jayich, J. D. Thompson, and J. G. E. Harris. High quality mechanical and optical properties of commercial silicon nitride membranes. *Appl. Phys. Lett.* **92**, 103125, 2008.

[30] A. Bejan. *Heat transfer*. Wiley, 1993.

[31] V. Kaajakari, T. Mattila, A. Oja, J. Kiihamäki, and H. Seppä. Square-extensional mode single-crystal silicon micromechanical resonator for low-phase-noise oscillator applications. *IEEE Electron Device Lett.* **25**, 173-175, 2004.

[32] K. Y. Fong, W. H. P. Pernice, M. Li, and H. X. Tang. High Q optomechanical resonators in silicon nitride nanophotonic circuits. *Appl. Phys. Lett.* **97**, 073112, 2010.

[33] Y. T. Yang, K. L. Ekinci, X. M. H. Huang, L. M. Schiavone, M. L. Roukes, C. A. Zorman, and M. Mehregany. Monocrystalline silicon carbide nanoelectromechanical systems. *Appl. Phys. Lett.* **78**, 162, 2001.

[34] A. N. Cleland, M. Pophristic, and I. Ferguson. Single-crystal aluminium nitride nanomechanical resonators. *Appl. Phys. Lett.* **79**, 2070, 2001.

[35] K. L. Ekinci. Electromechanical transducers at the nanoscale: actuation and sensing of motion in nanoelectromechanical systems (NEMS). *Small* **1**, 786-797, 2005.

[36] J. A. Lee, S. W. Lee, K.-C. Lee, S. I. Park, and S. S. Lee. Fabrication and characterization of freestanding 3D carbon microstructures using multi-exposures and resist pyrolysis. *J. Micromech. Microeng.* **18**, 035012, 2008.

[37] L. Amato, S. S. Keller, A. Heiskanen, M. Dimaki, J. Emnéus, A. Boisen, and M. Tenje. Fabrication of high-aspect ratio SU-8 micropillar arrays. *Microelectron. Eng.* **98**, 483-487, 2012.

[38] Y. Lim, J. Heo, M. Madou, and H. Shin. Monolithic carbon structures including suspended single nanowires and nanomeshes as a sensor platform. *Nanoscale Res. Lett.* **8**, 492-501, 2013.

[39] P. T. Williams, and S. Besler. The influence of temperature and heating rate on the slow pyrolysis of biomass. *Renew. Energ.* **7**, 233-250, 1996.

[40] O. J. A. Schueller, S. T. Brittain, C. Marzolin, and G. M. Whitesides. Fabrication and characterization of glassy carbon MEMS. *Chem. Mater.* **9**, 1399-1406, 1997.

[41] H. L. Seung, B. Min, S. S. Lee, S. I. Park, and K.-C. Lee. High frequency carbon nanomechanical resonators embedded with carbon nanotube stiffening layers. *Appl. Phys. Lett.* **97**, 183108, 2010.

[42] A. Singh, J. Jayaram, M. Madou, and S. Akbar. Pyrolysis of negative photoresist to fabricate carbon structures for microelectromechanical systems and electrochemical applications. *J. Electrochem. Soc.* **149**, 78-83, 2002.

[43] S. S. Keller, G. Blagoi, M. Lillemose, D. Haefliger, and A. Boisen. Processing of thin SU-8 films. *J. Micromech. Microeng.* **18**, 125020, 2008.

[44] N. Noeth, S. S. Keller, and A. Boisen. Fabrication of a cantilever-based microfluidic flow meter with $nLmin^{-1}$ resolution. *J. Micromech. Microeng.* **21**, 015007, 2011.

[45] L. Amato, A. Heiskanen, R. Hansen, L. Gammelgaard, T. Rindzevicius, M. Tenje, J. Emnéus, and S. S. Keller. Dense high-aspect ratio 3D carbon pillars on interdigitated microelectrode arrays. *Carbon* **94**, 792-803, 2015.

[46] G. Canton, T. Do, L. Kulinsky, and M. Madou. Improved conductivity of suspended carbon fibers through integration of C-MEMS and electro-mechanical spinning technologies. *Carbon* **71**, 338-342, 2014.

[47] S. Ranganathan, R. McCreery, S. M. Majji, and M. Madou. Photoresist-derived carbon for microelectromechanical systems and electrochemical applications. *J. Electrochem. Soc.* **147**, 277-282, 2000.

[48] http://www.polytec.com/us/solutions/vibration-measurement/basic-principles-of-vibrometry/ Accessed 10 November 2016.

[49] P. Castellini, M. Martarelli, and E. P. Tomasini. Laser Doppler vibrometry: development of advanced solutions to technology's needs. *Mech. Syst. Signal Pr.* **20**, 1265-1285, 2006.

[50] S. Schmid. Electrostatically actuated all-polymer microbeam resonators – characterization and application; Appendix E; Der Andere Verlag, Volume 6, Switzerland, 2009.

[51] K. Y. Yasumura, T. D. Stowe, E. Chow, T. Pfafman, T. W. Kenny, B. C. Stipe, and D. Rugar. Quality factors in micron- and submicron-thick cantilevers. *J. Microelectromech. Syst.* **9**, 117-125, 2000.

[52] S. A. Chandorkar, M. Agarwal, R. Melamud, R. N. Candler, K. E. Goodson, and T. W. Kenny. Limits of quality factor in bulk-mode micromechanical resonators. *Proc. IEEE MEMS Conf.*, Tucson, AZ, USA, 74-77, January 2008.

[53] C. Zhang, G. Xu, and Q. Jiang. Analysis of the air-damping effect on a micromachined beam resonator. *Math. & Mech. of Solids* **8**, 315-325, 2003.

[54] W. Ye, X. Wang, W. Hemmert, D. Freeman, and J. White. Air damping in laterally oscillating microresonators: a numerical and experimental study. *J. Microelectromech. Syst.* **12**, 557- 566, 2003.

[55] D. M. Photiadis, and J. A. Judge. Attachment losses of high Q oscillators. *Appl. Phys. Lett.* **85**, 482-484, 2004.

[56] Z. Hao, A. Erbil, and F. Ayazi. An analytical model for support loss in micromachined beam resonators with in-plane flexural vibrations. *Sensor Actuat. A-Phys.***109**, 156-164, 2003.

[57] J. H. Ko, J. Jeong, J. Choi, and M. Cho. Quality factor in clamping loss of nanocantilever resonators. *Appl. Phys. Lett.* **98**, 171909, 2011.

[58] A. A. Kiselev, and G. J. Iafrate. Phonon dynamics and phonon assisted losses in Euler-Bernoulli nanobeams. *Phys. Rev. B* **77**, 205436, 2008.

[59] K. Kunal, and N. R. Aluru. Akhiezer damping in nanostructures. *Phys. Rev. B* **84**, 245450, 2011.

[60] R. Lifshitz, and M. L. Roukes. Thermoelastic damping in micro- and nanomechanical systems. *Phys. Rev. B* **61**, 5600, 2000.

[61] S. Vengallatore. Analysis of thermoelastic damping in laminated composite micromechanical beam resonatos. *J. Micromech. Microeng.* **15**, 2398-2404, 2005.

[62] S. Prabhakar, and S. Vengallatore. Theory of thermoelastic damping in micromechanical resonators with two-dimensional heat conduction. *J. Microelectromech. Syst.* **17**, 494-502, 2008.

[63] D. A. Czaplewski, J. P. Sullivan, T. A. Friedmann, D. W. Carr, B. E. N. Keeler, and J. R. Wendt. Mechanical dissipation in tetrahedral amorphous carbon. *J. Appl. Phys.* **97**, 023517, 2005.

[64] http://www.engineeringtoolbox.com Accessed 14 November 2016.

[65] A. Olkhovets, S. Evoy, D. W. Carr, J. M. Parpia, and H. G. Craighead. Actuation and internal friction of torsional nanomechanical silicon resonators. *J. Vac. Sci. Technol. B* **18**, 3549-3551, 2000.

[66] S. Schmid, and C. Hierold. Damping mechanisms of single-clamped and prestressed double-clamped resonant polymer microbeams. *J. Appl. Phys.* **104**, 093516, 2008.

[67] S. Schmid, K. D. Jensen, K. H. Nielsen, and A. Boisen. Damping mechanisms in high-Q micro and nanomechanical string resonators. *Phys. Rev. B* **84**, 165307, 2011.

[68] N. C. Thomas. The early history of spectroscopy. *J. Chem. Educ.* **68**, 631-634, 1991.

[69] B. Stuart. *Infrared spectroscopy: fundamentals and applications.* Wiley, 2004.

[70] J. R. Durig. *Applications of FT-IR spectroscopy.* Elsevier, 1990.

[71] J. L. Koenig. *Spectroscopy of polymers.* Elsevier, 1999.

[72] H. W. Siesler, and K. Holland-Moritz. *The vibrational spectroscopy of polymers.* Cambridge University Press, 1989.

[73] S. R. Sandler, W. Karo, W. Bonesteel, and E. M. Pearce. *Polymer synthesis and characterization: a laboratory manual.* Academic Press, 1998.

[74] Z. Chen, Y. R. Shen, and G. A. Somorjai. Studies of polymer surfaces by sum frequency generation vibrational spectroscopy. *Annu. Rev. Phys. Chem.* **53**, 437-465, 2002.

[75] R. A. Merrill, and E. G. Bartick. Analysis of pressure sensitive adhesive tape: I. Evaluation of infrared ATR accessory advances. *J. Forensic Sci.* **45**, 93-98, 2000.

[76] C. A. Wilkie. TGA/FTIR: an extremely useful technique for studying polymer degradation. *Polym. Degrad. Stabil.* **66**, 301-306, 1999.

[77] P. I. Harris, and D. Chapman. The conformational analysis of peptides using Fourier transform IR spectroscopy. *Biopolymers* **37**, 251-263, 1995.

[78] L. K. Tamm, and S. A. Tatulian. Infrared spectroscopy of proteins and peptides in lipid bilayers. *Q. Rev. Biophys.* **30**, 365-429, 1997.

[79] J. Bandekar. Amide modes and protein conformation. *Biochim. Biophys, Acta* **1120**, 123-143, 1992.

[80] A. Barth. The infrared absorption of amino acid side chains. *Prog. Biophys. Mol. Biol.* **74**, 141-173, 2000.

[81] W. K. Surewicz, H. H. Mantsch, and D. Chapman. Determination of protein secondary structure by Fourier transform infrared spectroscopy: a critical assessment. *Biochemistry* **32**, 389-394, 1993.

[82] M. Banyay, M. Sarkar, and A. Gräslund. A library of IR bands of nucleic acids in solution. *Biophys. Chem.* **104**, 477-488, 2003.

[83] E. Taillandier, and J. Liquier. Infrared spectroscopy of DNA. *Methods Enzymol.* **211**, 307-355, 1992.

[84] D. C. Fernandez, R. Bhargava, and S. M. Hewitt. Infrared spectroscopic imaging for histopathologic recognition. *Nat. Biotechnol.* **23**, 469-474, 2005.

[85] C. Petibois, V. Rigalleau, A. Mellin, A. Perromat,G. Cazorla, H. Gin, and G. Déléris. Determination of glucose in dried serum samples by Fourier-Transform Infrared Spectroscopy. *Clin. Chem.* **45**, 1530-1535, 1999.

[86] M. Kačuráková, and R. H. Wilson. Developments in mid-infrared FT-IR spectroscopy of selected carbohydrates. *Carbohydr. Polym.* **44**, 291-303, 2001.

[87] D. E. Bugay. Characterization of the solid-state: spectroscopic techniques. *Adv. Drug. Deliv. Rev.* **48**, 43-65, 2001.

[88] E. Ben-Dor, and A. Banin. Near-infrared analysis as a rapid method to simultaneously evaluate several soil properties. *Soil Sci. Soc. Am. J.* **59**, 364-372, 1993.

[89] N. H. Nielsen, S. Gordon, J. P. Pajander, J. Østergaard, T. Rades, and A. Müllertz. Biorelevant characterisation of amorphous furosemide salt exhibits conversion to a furosemide hydrate during dissolution. *Int. J. Pharm.* **457**, 14-24, 2013.

[90] J. A. DiMasi, R. W. Hansen, and H. G. Grabowski. The price of innovation: new estimates of drug development costs. *J. Health Econ.* **22**, 151-185,2003.

[91] M. T. Ansari, S. Karim, N. M. Ranjha, N. H. Shah, and S. Muhammad. Physicochemical characterization of artemether solid dispersions with hydrophilic carriers by freeze dried and melt methods. *Arch. Pharmacal Res.* **33**, 901-910, 2010.

[92] I. N. Papadoyannis, and V. F. Samanidou. *Encyclopedia of Chromatography.* Taylor & Francis, 2004.

[93] S. Bialkowski. *Photothermal spectroscopy methods for chemical analysis.* Wiley, 1996.

[94] M. G. Sowa, and H. H. Mantsch. Photothermal infrared spectroscopy: applications to medicine. *J. Mol. Struct.* **300**, 239-244, 1993.

[95] A. Hammiche, H. M. Pollock, M. Reading, M. Claybourn, P. H. Turner, and K. Jewkes. Photothermal FT-IR spectroscopy: a step towards FT-IR microscopy at a resolution better than the diffraction limit. *Appl. Spectrosc.* **53**, 810-815, 1999.

[96] W. B. Jackson, N. M. Amer, A. C. Boccara, and D. Fournier. Photothermal deflection spectroscopy and detection. *Appl. Opt.* **20**, 1333-1344, 1981.

[97] N. V. Lavrik, M. J. Sepaniak, and P. G. Datskos. Cantilever transducers as a platform for chemical and biological sensors. *Rev. Sci. Instrum.* **75**, 2229, 2004.

[98] G. Y. Chen, T. Thundat, E. A. Watcher, and R. J. Warmack. Adsorption-induced surface stress and its effects on resonance frequency. *J. Appl. Phys.* **77**, 3618-3622, 1995.

[99] M. D. Hsieh, and E. T. Zellers. Limits of recognition for simple vapor mixtures determined with a microsensor array. *Anal. Chem.* **76**, 1885-1895, 2004.

[100] C. Jin, and E. T. Zellers. Limits of recognition for binary and ternary vapor mixtures determined with multitransducer arrays. *Anal. Chem.* **80**, 7283-7293, 2008.

[101] W. Zhao, L. A. Pinnaduwage, J. W. Leis, A. C. Gehl, S. L. Allman, A. Shepp, and K. K. Mahmud. Identification and quantification of components in ternary vapor mixtures using a microelectromechanical-system-based electronic nose. *J. Appl. Phys.* **103**, 104902, 2008.

[102] J. K. Gimzewski, Ch. Gerber, E. Meyerm and R. R. Schlittler. Observation of a chemical reaction using a micromechanical sensor. *Chem. Phys. Lett.* **217**, 589-594, 1994.

[103] T. Thundat, R. J. Warmack, G. Y. Chen, and D. P. Allison. Thermal and ambient-induced deflections of scanning force microscope cantilevers. *Appl. Phys. Lett.* **64**, 2894, 1994.

[104] M. Bagheri, I. Chae, D. Lee. S. Kim, and T. Thundat. Selective detection of physisorbed hydrocarbons using photothermal cantilever deflection spectroscopy. *Sens. Actuat. B-Chem.* **191**, 765-769, 2014.

[105] S. Yoon, J. Son, W. Lee, H. Lee, and CW. Lee. Prediction of bitumen content in oil sand based on FT-IR measurement. *J. Ind. Eng. Chem.* **15**, 370-374, 2009.

[106] A. R. Krause, C. Van Neste, L. Senesac, T. Thundat, and E. Finot. Trace explosive detection using photothermal deflection spectroscopy. *J. Appl. Phys.***103**, 094906, 2008.

[107] O. Zandieh, and S. Kim. Sensitive and selective detection of adsorbed explosive molecules using opto-calorimetric infrared spectroscopy and micro-differential thermal analysis. *Sens. Actuat. B-Chem.* **231**, 393-398, 2016.

[108] S. Kim, D. Lee, R. Thundat, M. Bagheri, and T. Thundat. Photothermal cantilever deflection spectroscopy. *ECS Trans.* **50**, 459-464, 2013.

[109] M. Yun, Ch. Yim, N. Jung, S. Kim, T. Thundat, and S. Jeon. Nanomechanical thermal analysis of photosensitive polymers. *Macromolecules* **44**, 9661-9665, 2011.

[110] M. F. Khan, S. Kim, D. Lee, S. Schmid, A. Boisen, and T. Thundat. Nanomechanical identification of liquid reagents in a microfluidic channel. *Lab Chip* **14**, 1302-1307, 2014.

[111] B. Bhushan. *Springer handbook of nanotechnology.* Springer, 2010.

[112] O. Hansen, and A. Boisen. Noise in piezoresistive atomic force microscopy. *Nanotechnology* **10**, 51-60, 1999.

[113] H. J. Butt, and M. Jaschke. Calculation of thermal noise in atomic force microscopy. *Nanotechnology* **6**, 1-7, 1995.

[114] N. Miriyala, M. F. Khan, and T. Thundat. Thermomechanical behavior of a biomaterial microchannel cantilever subjected to periodic IR radiation. *Sens. Actuat. B-Chem.* **235**, 273-279, 2016.

[115] A. J. Andersen, S. Yamada, E. K. Pramodkumar, T. Andresen, A. Boisen, and S. Schmid. Nanomechanical IR spectroscopy for fast analysis of liquid-dispersed engineered nanomaterials. *Sens. Actuat. B-Chem.* **233**, 667-673, 2016.

[116] R. Feng, and R. J. Farris. Influence of processing conditions on the thermal and mechanical properties of SU8 negative photoresist coatings. *J. Micromech. Microeng.***13**, 80-88, 2003.

[117] H. Lorenz, M. Despont, N. Fahrni, N. LaBianca, P. Renaud, and P. Vettiger. SU-8: a low-cost negative resist for MEMS. *J. Micromech. Microeng.* **7**, 121-124, 1997.

[118] M. T. Alam, M. P. Manoharan, M. A. Haque, C. Muratore, and A. Voevodin. Influence of strain on thermal conductivity of silicon nitride thin films. *J. Micromech. Microeng.* **22**, 045001, 2012.

[119] C. H. Mastrangelo, Y.-Ch. Tai, and R. S. Muller. Thermophysical properties of low-residual stress, Silicon-rich, LPCVD silicon nitride films. *Sens. Actuat. A-Phys.* **23**, 856-860, 1990.

[120] N. Stojanovic, J. Yun, E. B. K. Washington, J. M. Berg, M. W. Holtz, and H. Temkin. Thin-film thermal conductivity measurements using microelectrothermal test structures and finite-element-model-based data analysis. *J. Microelectromech. Syst.* **16**, 1269-1275, 2007.

[121] T. F. Retajczyk, and A. K. Sinha. Elastic stiffness and thermal expansion coefficients of various refractory silicides and silicon nitride films. *Thin Solid Films* **70**, 241-247, 1980.

[122] X. Zhang, and C. P. Grigoropoulos. Thermal conductivity and diffusivity of free-standing silicon nitride thin films. *Rev. Sci. Instrum.* **66**, 1115-1120, 1995.

[123] F. L. Riley. Silicon nitride and related materials. *J. Am. Ceram. Soc.* **83**, 245-265, 2000.

[124] M. Stadtmüeller. Mechanical stress of CVD-dielectrics. *J. Electrochem. Soc.* **139**, 3669-3674, 1992.

[125] S. Yamada. Analyzing engineered nanoparticles using photothermal infrared spectroscopy. Ph.D. thesis, Denmark, 2016.

[126] S. Franssila. *Introduction to microfabrication*. Wiley, 2010.

[127] J. A. Thornton, and D. W. Hoffman. Stress-related effects in thin films. *Thin Solid Films* **171**, 5-31, 1989.

[128] A. Stoffel, A. Kovács, W. Kronast, and B. Müller. LPCVD against PECVD for micromechanical applications. *J. Micromech. Microeng.* **6**, 1-13, 1996.

[129] C. A. Mack. Corner rounding and line-end shortening in optical lithography. *Microlithographic techniques in integrated circuit fabrication II, Proc.,* SPIE, **4226**, 83-92, 2000.

[130] S. Schmid, M. Kurek, J. Q. Adolphsen, and A. Boisen. Real-time single airborne nanoparticle detection with nanomechanical resonant filter-fiber. *Sci. Rep.* **3**, 1288, 2013.

[131] W. C. Hinds. *Aerosol technology.* Wiley, 1999.

[132] M. J. Manton. The impaction of aerosols on a nuclepore filter. *Atmos. Environ.* **12**, 1669-1675, 1978.

[133] K. R. Spurný, J. P. Lodge, E. R. Frank, and D. C. Sheesley. Aerosol filtration by means of nuclepore filters: structural and filtration properties. *Environ. Sci. Technol.* **3**, 453-464, 1969.

[134] I. Ogura, N. Hashimoto, M. Kotake, H. Sakurai, A. Kishimoto, and K. Honda. Aerosol particle collection efficiency of holey carbon film-coated TEM grids. *Aerosol Sci. Tech.* **48**, 758-767, 2014.

[135] S. Marre, and J. Palmeri. Theoretical study of aerosol filtration by nucleopore filters: the intermediate crossover regime of Brownian diffusion and direct interception. *J. Colloid Interface Sci.* **237**, 230-238, 2001.

[136] I. Ogura, M. Kotake, H. Sakurai, and K. Honda. Surface-collection efficiency of nuclepore filters for nanoparticles. *Aerosol Sci. Technol.* **50**, 846-856, 2016.

[137] M. J. Manton. Brownian diffusion of aerosols to the face of a nuclepore filter. *Atmos. Environ.* **13,** 525-531, 1979.

[138] Model 3076 Constant Output Atomizer. Instruction manual. P/N 1933076, Revision J, 2005.

[139] M. Fierz, C. Houle, P. Steigmeier, and H. Burtscher. Design, calibration, and field performance of a miniature diffusion size classifier. *Aerosol Sci. Tech.* **45**, 1-10, 2011.

[140] S. Bau, B. Zimmermann, R. Payet, and O. Witschger. A laboratory study of the performance of the handheld diffusion size classifier (DiSCmini) for various aerosols in the 15-400 nm range. *Environ. Sci. Process. Impacts* **17**, 261-269. 2015.

[141] T. Xiang, and B. D. Anderson. Molecular dynamics simulation of amorphous indomethacin. *Mol. Pharm.* **10**, 102-114, 2013.

[142] J. Faist, F. Capasso, D. L. Sivco, C. Sirtori, A. L. Hutchinson, and A. Y. Cho. Quantum cascade laser. *Science* **264**, 553-556, 1994.

[143] R. Maulini, M. Beck, J. Faist, and E. Gini. Broadband tuning of external cavity bound-to-continuum quantum-cascade lasers. *Appl. Phys. Lett.* **84**, 1659, 2004.

[144] LaserTune IR source and external IR detector. User Manual. Version 2.00, 2014.

[145] W. C. Michels, and N. L. Curtis. A pentode lock-in amplifier of high frequency selectivity. *Rev. Sci. Instrum.* **12**, 444-447, 1941.

[146] J. H. Scofield. Frequency-domain description of a lock-in amplifier. *Am. J. Phys.* **62**, 129-133, 1994.

[147] A. N. Cleland, and M. L. Roukes. External control of dissipation in a nanometer-scale radiofrequency mechanical resonator. *Sens. Actuat. A-Phys.* **72**, 256-261, 1999.

[148] E. Collin, M. Defoort, K. Lulla, T. Moutonet, J.-S. Heron, O. Bourgeois, Y. M. Bunkov, and H. Godfrin. In-situ comprehensive calibration of a tri-port nano-electro-mechanical device. *Rev. Sci. Instrum.* **83**, 045005, 2012.

[149] A. Venkatesan, K. J. Lulla, M. J. Patton, A. D. Armour, C. J. Mellor, and J. R. Owers-Bradley. Dissipation due to tunneling two-level systems in gold nanomechanical resonators. *Phys. Rev. B* **81**, 073410, 2010.

[150] M. Defoort, K. J. Lulla, C. Blanc, H. Ftouni, O. Bourgeois, and E. Collin. Stressed silicon nitride nanomechanical resonators at helium temperatures. *J. Low Temp. Phys.* **171**, 731-736, 2013.

[151] M. Defoort, K. J. Lulla, T. Crozes, O. Maillet, O. Bourgeois, and E. Collin. Slippage and boundary layer probed in an almost ideal gas by a nanomechanical resonators. *Phys. Rev. Lett.* **113**, 136101, 2014.

[152] W. J. Venstra, H. J. R. Westra, K. Babaei Gavan, and H. S. J. van der Zant. Magnetomotive drive and detection of clamped-clamped mechanical resonators in water. *Appl. Phys. Lett.* **95**, 263103, 2009.

[153] X. L. Feng, C. J, White, A. Hajimiri, and M. L. Roukes. A self-sustaining ultrahigh-frequency nanoelectromechanical oscillator. *Nat. Nanotechnol.* **3**, 342-346, 2008.

[154] K. Halbach. Design of permanent multipole magnets with oriented rare earth cobalt material. *Nucl. Instr. Meth.* **169**, 1-11, 1980.

[155] M. Pedersen, W. Olthuis, P. Bergeveld. The 8th International Conference on Solid-State Sensors and Actuators. 234.A7, 13-16, 1995.

[156] Q. P. Unterreithmeier, T. Faust, and J. Kotthaus. Damping of nanomechanical resonators. *Phys. Rev. Lett.* **105**, 027205, 2010.

[157] S. Chakram, Y. S. Patil, L. Chang, and M. Vengalattore. Dissipation in ultrahigh quality factor SiN membrane resonators. *Phys. Rev. Lett.* **112**, 127201, 2014.

[158] L. G. Villanueva, and S. Schmid. Evidence of surface loss as ubiquitous limiting damping mechanism in SiN micro- and nanomechanical resonators. *Phys. Rev. Lett.* **113**, 227201, 2014.

[159] L. S. Cutler, and C. L. Searle. Some aspects of the theory and measurement of frequency fluctuations in frequency standards. *Proc. IEEE* **54**, 136-154, 1966.

[160] D. W. Allan. Statistics of atomic frequency standards. *Proc. IEEE* **54**, 221-230, 1966.

[161] J. A. Barnes, A. R. Chi, L. S. Cutler, D. J. Healey, D. B. Leeson, T. E. McCunigal, J. A. Mullen, W. L. Smith, R. L. Sydnor, R. F. C. Vessot, and G. M. R. Winkler. Characterization of frequency stability. *IEEE Trans. Instrum. Meas.* **20**, 105-120, 1971.

[162] T. Larsen. Micro-mechanical temperature sensors. Ph.D. thesis, Denmark, 2012.

[163] N. Wada, and S. A. Solin. Ramand and IR absorption spectroscopic studies on α, β and amorphous Si_3N_4. *J. Non.-Cryst. Solids* **43**, 7-15, 1981.

[164] H. Cho, B. Jeong, M.-F. Yu, A. Vakakis, D. M. McFarland, and L. A. Bergman. Nonlinear hardening and softening resonances in micromechanical cantilever-nanotube systems originated from nanoscale geometric nonlinearities. *Int. J. Solids Struct.* **49**, 2059-2065, 2012.

[165] K. Ren, M. B. Pisani, P. Kao, and S. Tadigadapa. Micromachined quartz resonator-based high performance thermal sensors. IEEE SENSORS 2010 Conference, 2197-2210, 2010.

[166] P. Eriksson, J. Y. Andersson, and G. Stemme. Thermal characterization of surface-micromachined silicon nitride membranes for thermal infrared detectors. *J. Microelectromech. S.* **6**, 55-61, 1997.

[167] Z. Wang, X. Qiu, J. Oiler, J. Zhu, and H. Yu. Film bulk acoustic-wave resonator (FBAR) based infrared sensor. 5th IEEE International Conference on Nano/Micro Engineered and Molecular Systems. 824-827, 2010.

[168] A. K. Pandey, O. Gottlieb, O. Shtempluck, and E. Buks. Performance of an AuPd micromechanical resonator as a temperature sensor. *Appl. Phys. Lett.* **96**, 203105, 2010.

[169] T. Harris, B. Kim, Ch. Reinke, P. Hopkins, T. Olsson, I. El-Kady, E. Shaner, and J. Sullivan. Thermal Conductivity measurements of silicon thin films with periodically arrayed nanoscale perforations. IMECE Conference, 2011.

[170] J. Tang, H.-T. Wang, D. H. Lee, M. Fardy, Z. Huo, T. P. Russell, and P. Yang. Holey silicon as an efficient thermoelectric material. *Nano Lett.* **10**, 4279-4283, 2010.

[171] D. Song, and G. Chen. Thermal conductivity of periodic microporous silicon films. *Appl. Phys. Lett.* **84**, 687-689, 2004.

[172] A. S. Chauhan, S. Sridevi, K. B. Chalasani, A. K. Jain, S. K. Jain, N. K. Jain, and P. V. Diwan. Dendrimer-mediated transdermal delivery: enhanced bioavailability of indomethacin. *J. Control. Release* **90**, 335-343, 2003.

[173] S. B. La, T. Okano, and K. Kataoka. Preparation and characterization of the micelle-forming polymeric drug indomethacin-incorporated poly(ethylene oxide)-poly(β-benzyl L-aspartate block copolymer micelles. *J. Pharm. Sci.* **85**, 85-90, 1996.

[174] H. Liu, N. Finn, and M. Z. Yates. Encapsulation and sustained release of a model drug, indomethacin, using CO_2-based microencapsulation. *Langmuir* **21**, 379-385, 2005.

[175] L. H. Nielsen, S. S. Keller, K. C. Gordon, A. Boisen, T. Rades, and A. Müllertz. Spatial confinement can lead to increased stability of amorphous indomethacin. *Eur. J. Pharm. Biopharm.* **81**, 418-425, 2012.

[176] A. Forster, J. Hempenstall, and T. Rades. Characterization of glass solutions of poorly water-soluble drugs produced by melt extrusion with hydrophilic amorphous polymers. *J. Pharm. Pharmacol.* **53**, 303-315, 2001.

[177] M. F. Khan, N. Miriyala, J. Lee, M. Hassanpourfard, A. Kumar, and T. Thundat. Heat capacity measurements of sub-nanoliter volumes of liquids using biomaterial microchannel cantilevers. *Appl. Phys. Lett.* **108**, 211906, 2016.

[178] K. O. Bugaev, A. A. Zelenina, and V. A. Volodin. Vibrational spectroscopy of chemical species on silicon and silicon-rich nitride thin films. *Int. J. Spectrosc.* **2012**, 281851, 2012.

[179] G. Rudakov, and I. Reshetnikov. IR spectra of ICPCVD SiNx thin films for MEMS structures. *JPCS*, **643**, 012063, 2015.

[180] K. Löbmann, R. Laitinen, H. Grohganz, K. C. Gordon, C. Strachan, and T. Rades. Coamorphous drug systems: enhanced physical stability and dissolution rate of indomethacin and naproxen. *Mol. Pharm.* **8**, 1919-1928, 2011.

[181] L. S. Taylor, and G. Zografi. Spectroscopic characterization of interactions between PVP and indomethacin in amorphous molecular dispersions. *Pharmaceut. Res.* **14**, 1691-1698, 1997.

[182] N. Kaneniwa, M. Otsuka, and T. Hayashi. Physicochemical characterization of indomethacin polymorphs and the transformation kinetics in ethanol. *Chem. Pharm. Bull.* **33**, 3447-3455, 1985.

[183] A. Forster, J. Hempenstall, and T. Rades. Characterization of glass solutions of poorly water-soluble drugs produced by melt extrusion with hydrophilic amorphous polymers. *J. Pharm. Pharmacol.* **53**, 303-315, 2001.

[184] A. Salari, and R. E. Young. Application of attenuated total reflectance FTIR spectroscopy to the analysis of mixtures of pharmaceutical polymorphs. *Int. J. Pharm.* **163**, 157-166, 1998.

[185] L. H. Nielsen, S. Gordon, R. Holm, A. Selen, T. Rades, and A. Müllertz. Preparation of an amorphous sodium furosemide salt improves solubility and dissolution rate and leads to T_{max} after oral dosing to rats. *Eur. J. Pharm. Biopharm.* **85**, 942-951, 2013.

[186] J. F. Bauer. Pharmaceutical solids – the amorphous phase. *J. Validation. Technol.* **15**, 63-68, 2009.

[187] S. J. Byard, S. L. Jackson, A. Smail, M. Bauer, and D. C. Apperley. Studies on the crystallinity of a pharmaceutical development drug substance. *J. Pharm. Sci.* **6**, 1321-1335, 2005.

[188] P. Mura, M. T. Faucci, F. Maestrelli, S. Furlanetto, and S. Pinzauti. Characterization of physicochemical properties of naproxen systems with amorphous β-cyclodextrin-epichlorohydrin polymers. *J. Pharm. Biomed. Anal.* **29**, 1015-1024, 2002.

[189] M. K. Gupta, A. Vanwert, and R. H. Bogner. Formation of physically stable amorphous drugs by milling with neusilin. *J. Pharm. Sci.* **92**, 536-551, 2003.

[190] F. A. Andersen, and L. Brečević. Infrared spectra of amorphous and crystalline calcium carbonate. *Acta Chem. Scand.* **45**, 1018-1024, 1991.

[191] G. Buckton, E. Yonemochi, J. Hammond, and A. Moffat. The use of near infra-red spectroscopy to detect changes in the form of amorphous and crystalline lactose. *Int. J. Pharm.* **168**, 231-241, 1998.

[192] L. Zhou, R. I. Kaiser, and A. T. Tokunaga. Infrared spectroscopy of crystalline and amorphous diacetylene (C4H2) and implicatrions for Titan's atmospheric composition. *Planet. Space Sci.* **57**, 830-835, 2009.

[193] D. Ciolacu, F. Ciolacu, and V. I. Popa. Amorphous cellulose – structure and characterization. *Cell. Chem. Technol.* **45**, 13-21, 2011.

[194] S. G. Kazarian, and K. L. A. Chan. "Chemical photography" of drug release. *Macromolecules* **36**, 9866-9872, 2003.

[195] D. C. Apperley, A. H. Forster, R. Fournier, R. K. Harris, P. Hodgkinson, R. W. Lancaster, and T. Rades. Characterization of indomethacin and nifedipine using variable-temperature solid-state NMR. *Magn. Reson. Chem.* **43**, 881-892, 2005.

[196] F. Tian, H. Qum M. Louhi-Kultanen. Insight into crystallization mechanisms of polymorphic hydrate systems. *Chem. Eng. Technol.* **33**, 833-838, 2010.

[197] U. Paaver, A. Lust, S. Mirza, J. Rantanen, P. Veski, J. Heinämäki, and K. Kongermann. Insight into the solubility and dissolution of piroxicam anhydrate and monohydrate forms. *Int. J. Pharm.* **431**, 111-119, 2012.

[198] J. A. Zeitler, D. A. Newnham, P. F. Taday, C. J. Strachan, M. Pepper, K. C. Gordon, and T. Rades. Temperature dependent terahertz pulsed spectroscopy of carbamazepine. *Thermochim. Acta* **436**, 71-77, 2005.

[199] J. A. Zeitler, D. A. Newnham, P. F. Taday, T. L. Threlfall, R. W. Lancaster, R. W. Berg, C. J. Strachan, M. Pepper, K. C. Gordon, and T. Rades. Characterization of temperature-induced phase transitions in five polymorphic forms of sulfathiazole by terahertz pulsed spectroscopy and differential scanning calorimetry. *J. Pharm. Sci.* **95**, 2486-2498, 2006.

[200] D. W. Reynolds, K. L. Facchine, J. F. Mullaney, K. M. Alsante, T. D. Hatajik, and M. G. Motto. Available guidance and best practices for conducting forced degradation studies. *Pharmaceutical Technology* **26**, 48-54, 2002.

[201] P. C. Weber, and F. R. Salemme. Applications of calorimetric methods to drug discovery and the study of protein interactions. *Curr. Opin. Struc. Biol.* **13**, 115-121, 2003.

[202] S. K. Singh, and N. Caram-Lelham. Thermodynamics of κ-carrageenan-amphiphilic drug interaction as influenced by specific counterions and temperature: a microcalorimetric and viscometric study. *J. Colloid Interface Sci.* **203**, 430-446, 1998.

Acknowledgements

First and foremost, I would like to thank my supervisors Anja Boisen and Silvan Schmid. They were so kind to trust and accept me for a stay in the Nanoprobes group during summer 2012 which was a unique opportunity for me to gain hands-on experience in nanotechnology. It was also them who encouraged me later to apply for a Ph.D. position at DTU Nanotech. I really appreciate your guidance and admire your extensive knowledge in the field of nanoelectromechanical systems. Your support throughout my research was simply priceless.

Members of the Nanoprobes group come from different societal cultures, geographic regions and scientific backgrounds. This diversity definitely contributed to exceptional and inspiring atmosphere and wonderful working environment. I would like to thank all the great people that I met here for their willingness to share skills and expertise. Especially I am grateful to Ole Hansen, Stephan Sylvest Keller, Andrea Casci Ceccacci and Peter Larsen who did his best as a new leader of the "Resonator Guild".

I am thankful to DTU Danchip staff for their patience during countless training sessions and dedication to solving fabrication-related problems. I would like to thank Jan Frank Pedersen from DTU Mekanik for machining parts of experimental setups and En-Te Hwu together with his associates from Academia Sinica in Taiwan for their help with Blu-ray optical pickup head system.

I would like to express my gratitude to all my colleagues and friends who made my stay in Denmark an unforgettable experience. Discovering this one of a kind country and its culture was a pleasure.

Last but not least, I would like to thank my family for support and faith in me. I would like to extent special thanks to my wife Katarzyna who was always by my side no matter the circumstances.

Appendix A

Fabrication process flows

Fabrication of pyrolytic carbon nanomechanical resonators using AZ 5214e and SU-8 2005 photoresist, respectively. Dry etch and pyrolysis have been performed in different order in both cases.

Substrate: Silicon <100>, 4” 525 µm thick single side polished wafers.

Process	Step N°	Description	Equipment	Parameters/ Recipe	Target	Remarks
Wafer preparation	1	Dip in BHF	Wet bench	60 s		Remove native oxide
Photolitography	2	Spin coating of AZ	Maximus	30 s, 1000 rpm/s, 725 rpm	4.2 µm	
	3	Soft-baking	Maximus	60 s, 90°C		
	4	Exposure	KS Aligner	14 s, hard contact		Mask "String resonators"
	5	Development	Developer 1	70 s, 3 min rinse and 90 s spin rinse drying		
Dry etch	6	Release of the structures	ASE	1500 W coil power, 0 W platen power, 300 sccm SF6 gas flow, 0°C chuck temperature, 5 min etch time		Isotropic etch
Pyrolysis	7	Pyrolysis of photoresist	Resist Pyrolysis Furnace	24 L/min N2 gas flow, 30 min in 200°C and 60 min in 900°C, 2°C/min ramp		

Process	Step N°	Description	Equipment	Parameters/ Recipe	Target	Remarks
Wafer preparation	1	Dehydration bake	Hotplate 1	30 min, 250°C		
Photolitography	2	Spin coating of SU-8	RCD8	30 s, 5000 rpm/s, 2000 rpm	5.5 µm	
	3	Solvent evaporation		2h in ventilated area		
	4	Exposure	KS Aligner	28 s, hard contact		Mask "String resonators"
	5	Post exposure baking	Hotplate 2	60 min in 50°C, 2°C/min ramp		
	6	Development	Developer bench	2 min in PGMEA (FIRST), 2 min in PGMEA (FINAL), 2 min rinse in IPA and 60 s dry in air		
Dry etch	7	Release of the structures	ASE	1500 W coil power, 0 W platen power, 300 sccm SF6 gas flow, 0°C chuck temperature, 5 min etch time		Isotropic etch
Pyrolysis	8	Pyrolysis of photoresist	Resist Pyrolysis Furnace	24 L/min N2 gas flow, 30 min in 200°C and 60 min in 900°C, 2°C/min ramp		

Fabrication of perforated silicon rich silicon nitride membrane resonators.

Substrate: Silicon <100>, 4” 350 µm thick double side polished wafers.

Process	Step N°	Description	Equipment	Parameters/ Recipe	Target	Remarks
LPCVD SiN	1	Deposition of low stress SiN	Furnace LPCVD Nitride (6")	4inc Is, 16 min 30 s	100 nm	
Wafer preparation	2	Dip in BHF	Wet bench	60 s		Remove native oxide
Photolitography I	3	Pretreatment with HMDS	HMDS oven	Program 4		Promote adhesion of photoresist
	4	Spin coating of AZ	SSE spinner	DCH_100mm_AZ5214E_1,5µm	1.5 µm	Front side
	5	Soft baking	SSE spinner	60 s, 90°C		
	6	Exposure	KS Aligner	7 s, hard contact		Mask "SiNFront"
	7	Development	Developer 1	70 s, 3 min rinse and 90 s spin rinse drying		
Dry etch I	8	Dry etch of SiN	AOE	SIO2_RES, 0°C, 45 s		Obtain perforation
Phlasma asher	9	Photoresist removal	Plasma asher 1	400 ml/min 02 gas flow, 70 ml/min N2 gas flow, 1000 W power, 40 min		
Photolitography II	10	Pretreatment with HMDS	HMDS oven	Program 4		Promote adhesion of photoresist
	11	Spin coating of nLOF	Gamma UV	3411	1.5 µm	Front side
	12	Soft baking	Gamma UV	60 s, 90°C		
	13	Exposure	KS Aligner	10 s, hard contact		Mask "METAL"
	14	Post exposure baking	Hotplate 2	60 s in 110°C		
	15	Development	TMAH UV-LITHO	60 s in 351B		
Plasma asher	16	Superfluous photoresist removal	Plasma asher 1	400 ml/min 02 gas flow, 70 ml/min N2 gas flow, 1000 W power, 40 min		
Metal deposition	17	Deposition of electrodes	Wordentec	E-beam process	5 nm of Ti and 50 nm of Au	
Lift-off	18	Superfluous metal removal	Lift-off bench	3 h in acetone		Obtain electrodes
PECVD SiN	19	Protective layer of SiN	PECVD 3	mfsinls2, 15 min	700 nm	
Photolitography III	20	Pretreatment with HMDS	HMDS oven	Program 4		Promote adhesion of photoresist
	21	Spin coating of AZ	SSE spinner	DCH_100mm_AZ5214E_1,5µm	1.5 µm	Back side
	22	Soft baking	SSE spinner	60 s, 90°C		
	23	Exposure	KS Aligner	7 s, hard contact		Mask "Backside"
	24	Development	Developer 1	70 s, 3 min rinse and 90 s spin rinse drying		
Dry etch II	25	Dry etch of SiN	RIE2	BGE_NITR, 4 min		Opening for KOH etch
Wet etch	26	Wet etch of Si in KOH	Fumehood (KOH)	28% KOH concentration, 80°C, 6 h		Releasing of the membranes
BHF strip	27	PECVD SiN removal	Wet bench	5 min		

Appendix B

Simulink models

Two models were developed in Simulink software in order to show difference between “single electrode” and “double electrode” designs. Actuation voltage was the input and electromotive force was the output for both models.

“Single electrode”

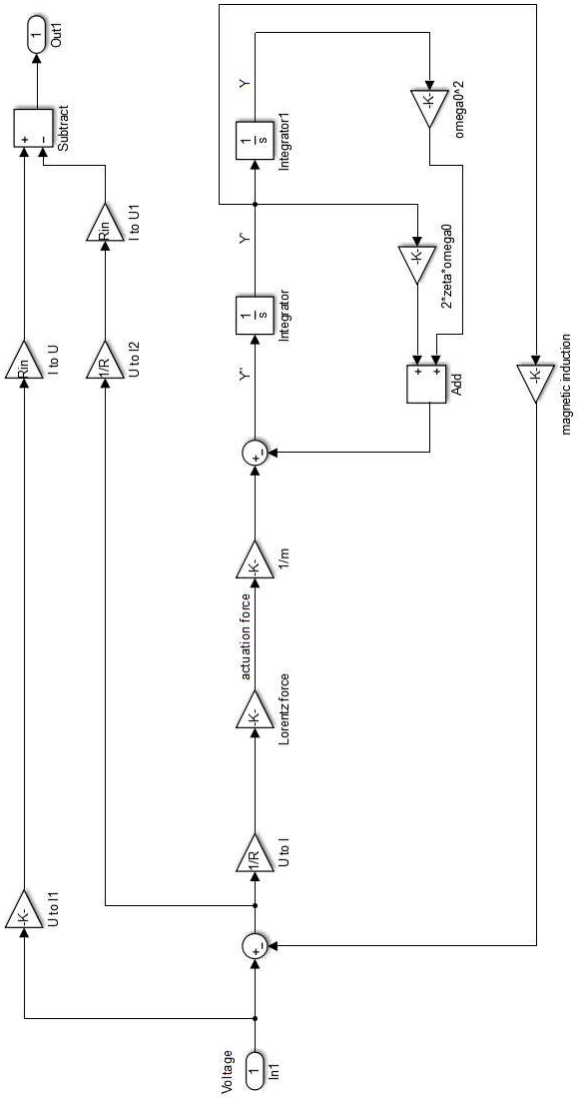

“Double electrode”

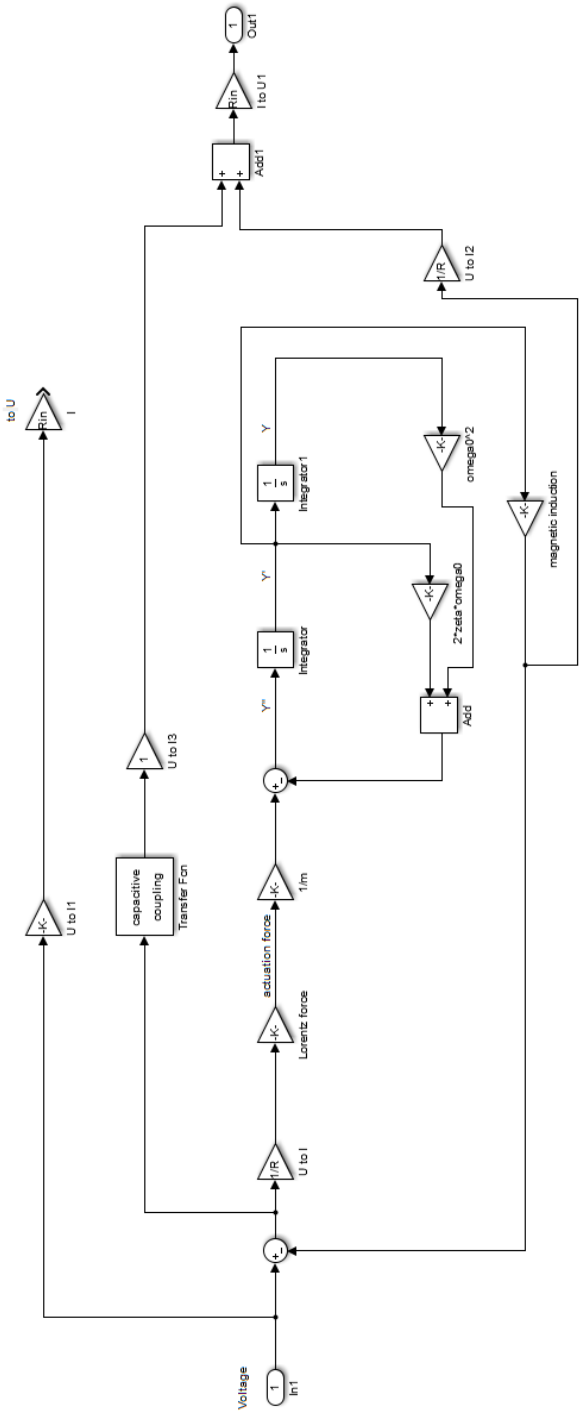

Appendix C

Experimental setup chamber design

The vacuum chamber for NAM-IR with magnetomotive readout and actuation consists of two aluminium parts that were designed in Autodesk Inventor 2016 software. All dimensions are in mm.

Part I

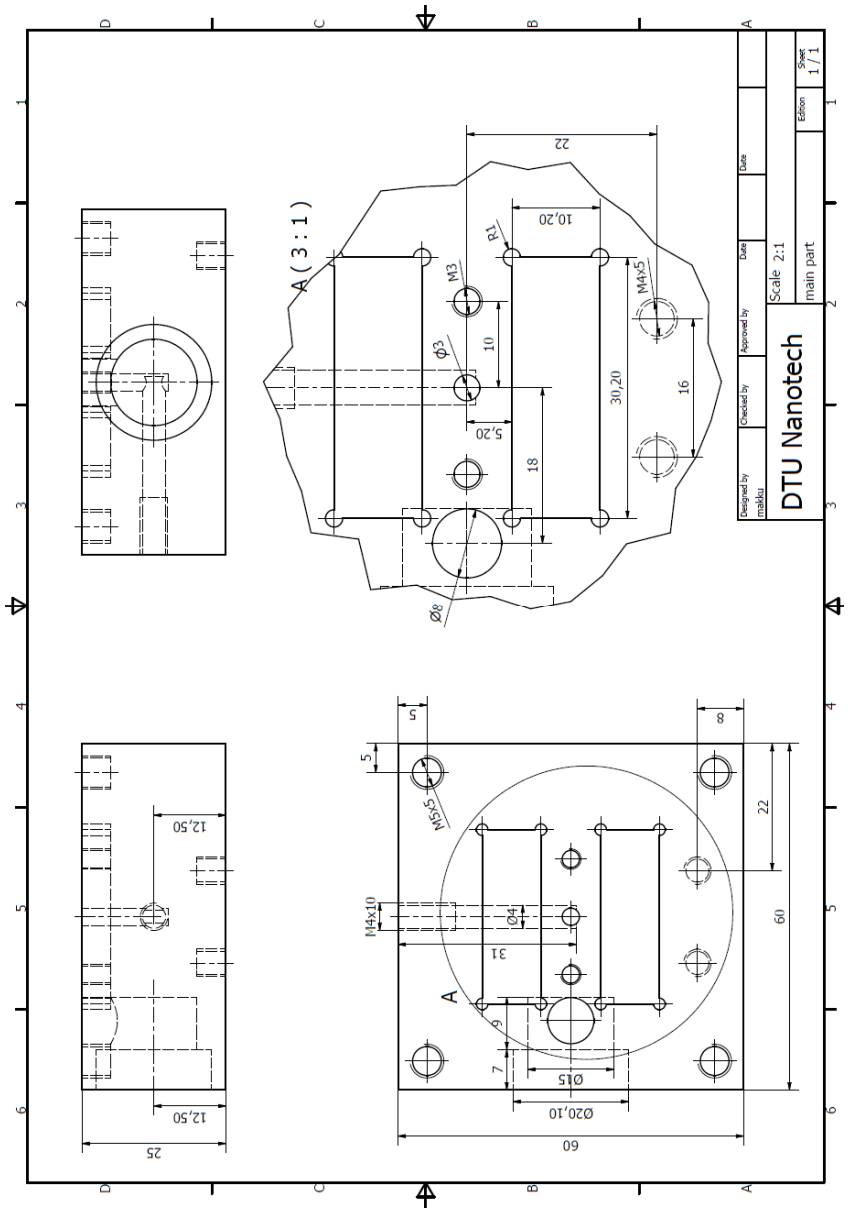

Part II

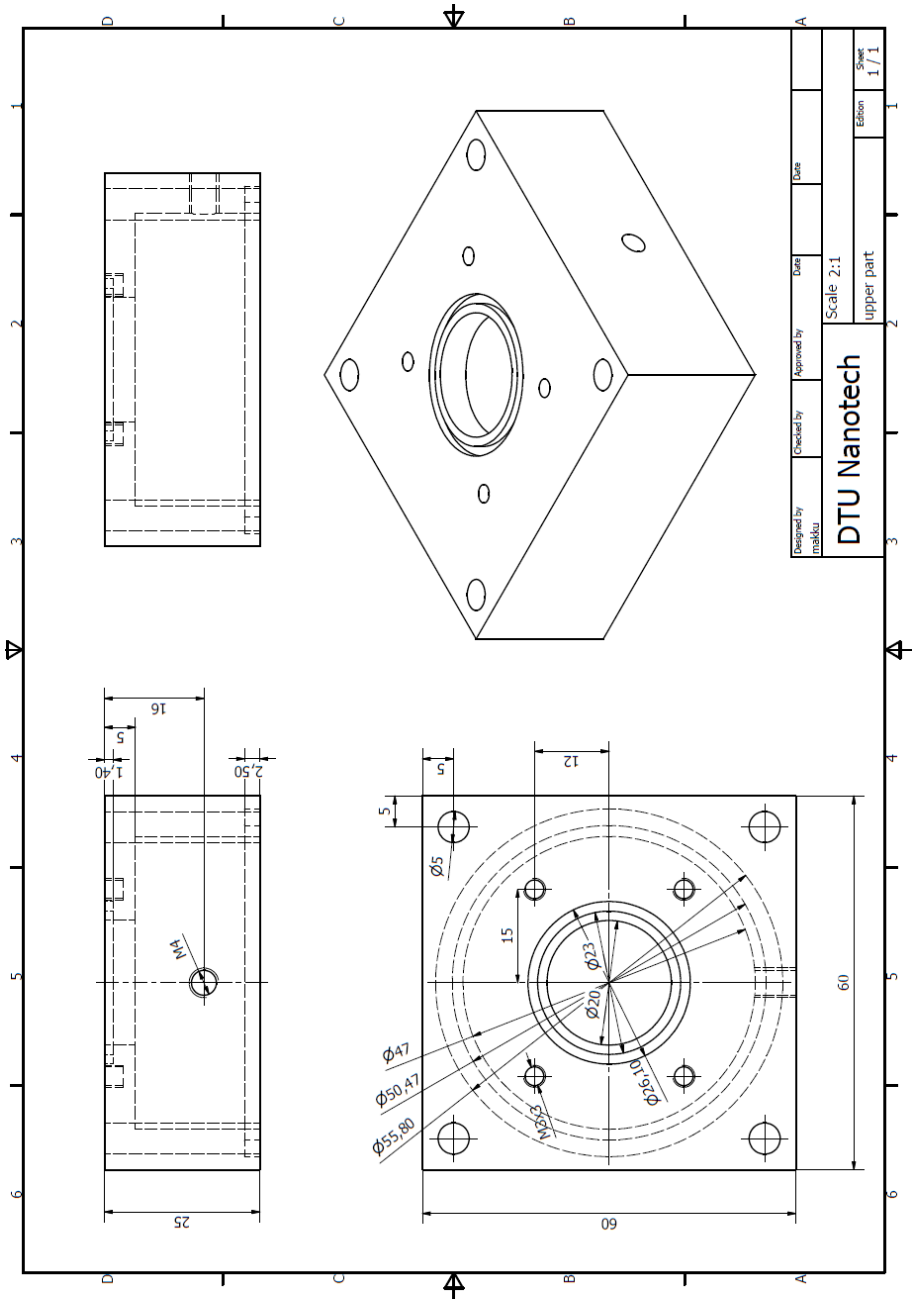
DTU Nanotech
Designed by makku
Checked by
Approved by
Date
Scale 2:1
upper part
Edition
Sheet 1 / 1
Ø5
Ø23
Ø20
Ø26,10
Ø47
Ø50,47
Ø55,80
M3
M4
15
60
12
5
16
1,40
2,50
25

Appendix D

Matlab script for calculation of Allan deviation

The script was developed by Luis Guillermo Villanueva.

```
function mp = AllanDev_RK(data)
%input argument data has time as a first column and frequency as a second
data=data(floor(end/100):end,:);
N=size(data,1);
% frequency data
f = data(:,2);
%time trace, assumed equidistant
dt = mean(diff(data(:,1)));%*1e-3;
t=[0:dt:(length(f)-1)*dt];
    f0=mean(f);
    df=f-f0;

%first cycle "i" is for time intervals i*dt is the interval
for i=3:floor(N/5)
    mp(i,1) = dt*i;

%this cycle "j" is to calculate average within i*dt long time interval
    for j = 1:floor(N/i)
        fp(j) = 0;
%this cycle "k" is for calculating the average frequency
        for k = 1:i
            fp(j) = fp(j) + f((j-1)*i+k)/i;
        end
    end
    fp = fp';
% fractional frequency
    yp = (fp - fp(1))./fp(1);
% difference frequency
    dp = diff(yp);
%allan deviation
    mp(i,2) = std(dp)/sqrt(2);
    mp(i,3) = sqrt(mean(dp.^2)/2);
%clean the arrays otherwise doesn't work
    clear fp yp dp;
end

    H=2*pi*tf([1],[1 0]);
    dphi=lsim(H,f,t);
    x=dphi/(2*pi*f0);
    tau=dt*[1:floor(size(mp,1))];
    sigmay_2=zeros(1,length(tau));
```

```
    for ii=1:1:length(tau)
        xtemp=x(1:round(tau(ii)/dt):length(x));
        ybar=diff(xtemp)/tau(ii);
        for j=1:length(ybar)-1
            sigmay_2(ii)=sigmay_2(ii)+(ybar(j+1)-ybar(j))^2;
        end
        sigmay_2(ii)=1/2*1/(length(ybar)-1)*sigmay_2(ii);
    end

    allandev=sqrt(sigmay_2);
    allandev(1:2)=0;
figure(200);
loglog(mp(:,1),mp(:,2),'b.-',mp(:,1),mp(:,3),'r.-,tau,allandev,'k.'); grid
on; hold on;
save Allan.dat mp -ASCII
```

Appendix E

List of publications

M. Kurek, F. K. Larsen, P. E. Larsen, S. Schmid, A. Boisen, and S. S. Keller. Nanomechanical pyrolytic carbon resonators: novel fabrication method and characterization of mechanical properties. *Sensors* **16**, 1097, 2016.

M. Kurek, M. Carnoy, P. E. Larsen, L. H. Nielsen, O. Hansen, T. Rades, S. Schmid, and A. Boisen. Nanomechanical infrared spectroscopy with vibrating filters for pharmaceutical analysis. Submitted to Angewandte Chemie International Edition, 2017.

M. Kurek, P. E. Larsen, S. Schmid, and A. Boisen. Simple electrodynamic transduction scheme for micromechanical resonators. Poster presentation at the 41st Micro and Nano Engineering Conference (MNE), The Hague, The Netherlands, 2015.

M. Kurek, F. K. Larsen, P. E. Larsen, S. Schmid, A. Boisen, and S. S. Keller. Micromechanical pyrolytic carbon string resonators. Oral presentation at the 13th International Workshop on Nanomechanical Sensing (NMC), Delft, The Netherlands, 2016.

M. Kurek, M. Carnoy, A. Boisen, and S. Schmid. Perforated SiN membrane resonators for nanomechanical IR spectroscopy. Poster presentation at the 42nd Micro and Nano Engineering Conference (MNE), Vienna, Austria, 2016.

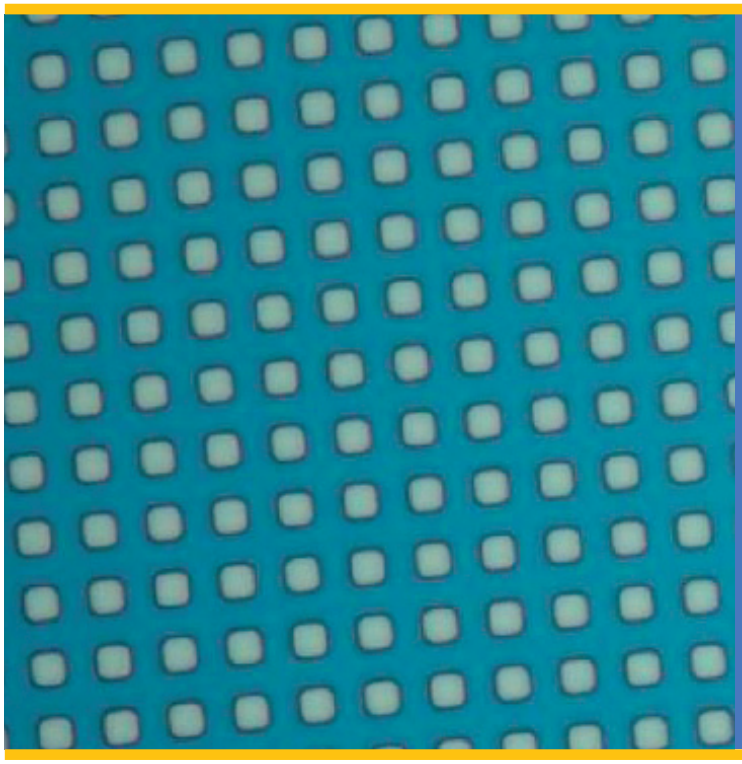

Published by:
DTU Nanotech
Department of Micro- and Nanotechnology
Technical University of Denmark
Ørsteds Plads, building 345C
DK-2800 Kgs. Lyngby